이학박사학위논문

열산화막에서의 전기화학을 기반으로 한 안트라센의 음극 전기유기반응과 수소 센서 응용을 위한 얇은 금속 박막 전기도금

Cathodic Electroorganic Reaction of Anthracene and Metal Thin Film Electrodeposition for Hydrogen Gas Sensor Based on Electrochemistry at Thermally Grown Silicon Oxide

2020 년 2 월

서울대학교 대학원

화학부 전기분석화학전공

신 재 호

열산화막에서의 전기화학을 기반으로 한 안트라센의 음극 전기유기반응과 수소 센서 응용을 위한 얇은 금속 박막 전기도금

지도교수 정 택 동

이 논문을 이학박사학위논문으로 제출함.

2020 년 2 월

서울대학교 대학원

화학부 전기화학전공

신 재 호

신재호의 박사학위논문을 인준함.

2020 년 2 월

위 원 장 손 병 혁 (인)

부 위 원 장 정 택 동 (인)

위 원 김 경 택 (인)

위 원 임 종 우 (인)

위 원 김 양 래 (인)

A Ph. D. Dissertation

Cathodic Electroorganic Reaction of Anthracene and Metal Thin Film Electrodeposition for Hydrogen Gas Sensor Based on Electrochemistry at Thermally Grown Silicon Oxide

By

Samuel Jaeho Shin

Supervisor: Professor Taek Dong Chung

Major: Electrochemistry

Department of Chemistry

Seoul National University

February 2020

Abstract

Electrochemistry on the insulator is counterintuitive although it may provide new insights on scientific findings and pioneering applications in many fields. Among the reports on faradaic reaction on insulators, the electrochemistry in electrolyte−oxide−semiconductor (EOS) system is worth to be noted that highly n−doped Si/thermal SiO_2 (n^+−Si/SiO_2) was brought into the solution as the electrode.

Thermal SiO_2 layer has a highly dielectric structure with minimal defects fabricated by oxidation of Si in the furnace and is generally used as the gate oxide in the semiconductor industry. With the underlying conductive substrate as highly n−doped Si (n^+−Si) to constitute an EOS system, it was reported that hydrogen atoms can be produced at n^+−Si/SiO_2. They are proposed to be responsible for faradaic current in voltammetry acting as “chemical electrode”, described such system as hydrogen atom mediated electrochemistry.

The research to seek what kind of chemistry is possible on insulators and what kind of application is possible were important but were overlooked. Especially, there must be a boundless field of chemistry brought into hydrogen atom from this system. Seek for the possible chemistry and application is the main theme of this dissertation.

In Chapter 1, a general background of the electrochemistry on the insulator, especially the hydrogen atom mediated electrochemistry on n^+-Si/SiO_2 electrode constituting the EOS system is provided. In addition, the perspectives of both the electrochemistry on the dielectric electrode and the hydrogen atoms in chemistry are discussed.

In Chapter 2, the investigation on the cathodic electroorganic reaction of the organic reactants on 200 nm thick defective n^+-Si/SiO_2 is discussed. It must be mentioned that the defective implies minimal pinholes and cracks but plenty of chemical defects such as dangling bonds or atom vacancies. This layer gives low faradaic current upon negative bias with no current upon positive bias in both acidic aqueous solution and acidic organic media. Its faradaic current depends only on proton concentration and the presence of redox couple contributes minor effect. Its electrochemical behavior is similar to the previous report.

The electrolysis of organic reactants was found to yield either *reduced* or *oxidized* products upon *cathodic* bias. Especially, anthracene and its derivatives are confirmed to be electrochemically *oxidized* as a consequence of *cathodic* electroorganic reaction on defective n^+-Si/SiO_2. Upon investigation, the electrochemically generated species, probably hydrogen atom, is suspected to involve in such a phenomenon. As described in Chapter 1, hydrogen atom possesses diverse reactivity towards reactants which correlates to

the observation. Various sets of experiments are provided to support the proposed reaction mechanism.

In Chapter 3, the direct electrodeposition of metal thin films on thermal SiO_2 is investigated and its application as a hydrogen gas sensor was demonstrated. By modifying the oxide surface with amine or 3–5 nm Au NPs, the electrodeposition faraday efficiency and the possible metals varied significantly. It was revealed from experimental results that uniform and thin metal films can be directly electrodeposited on n^+–Si/SiO_2–NH_2–AuNP despite the insulating layer, SiO_2. In addition, electroreduced Pd, Pt, Cu, and Ni firmly adhere to the oxide surface with the aid of pre–anchored Au NPs so that not only the amount of metal electroplated but also the faradaic efficiency was remarkably improved. These results indicate that the substrates for direct electrodeposition are not restricted to the conducting materials, but also include non–conducting surface by the aid of hydrogen atom mediated electrochemistry. Exploiting Pd directly electrodeposited on SiO_2, the H_2 gas sensor was demonstrated in a novel method to manufacture. Its performance was superior in response/recovery time in 0.1% H_2 with a low detection limit compared to the previous reports.

Keywords: Dielectric electrode, n^+–Si/SiO_2, Electrolyte–oxide–semiconductor (EOS) system, Hydrogen atom, Electroorganic reaction, Electrodeposition.

Student number: 2011-23227

Contents

List of Figures

membrane for electrolysis.

Figure 2-3 (a) Representative UV-VIS spectra after electrolysis of ANTH to AQ reaction in H-type divided cell by defective 200 nm n^+-Si/SiO_2 dielectric electrode. (b) UV-VIS spectra of standard ANTH and AQ in MeCN for comparison.

Figure 2-4 Schematic illustration and photos of the experimental setup for intermediate capture using TEMPO. (a) Three electrodes in an undivided cell. (b) CE separated by the double junction of Vycor tips. (c) Photo of the undivided cell and double junction Vycor tips in a solution-filled vial.

Figure 2-5 Representative voltammetric response of the defective 200 nm n^+-Si/SiO_2 electrode measured in N_2 atmosphere. Linear sweep voltammograms in (a) various concentration of aqueous acid solution, (b) $Fe(CN)_6^{3-/4-}$ redox couple in acidic aqueous solution, (c) various concentration of acid in MeCN, and (d) $Fc^{0/+}$ redox couple in acidic MeCN.

Figure 2-6 Electrochemical behavior of the defective 200 nm n^+-Si/SiO_2 electrode. (a) Cyclic voltammogram of large potential range in 1 mM $[Ru(II)(NH_3)_6]^{4-}$ + 1 mM $[Ru(III)(NH_3)_6]^{3-}$ + 0.5 M H_2SO_4 in H_2O. (b) Cyclic voltammogram of large potential range in 1 mM Fc + 1 mM Fc^+ + 1 M $HClO_4$ + 0.1 M TBAP in MeCN.

Figure 2-7 The typical *i*-*t* curve during electrolysis in 1 M $HClO_4$-MeCN solution at a constant voltage of − 1.67 V.

Figure 2-8 HR-TEM of the defective 200 nm n^+-Si/SiO_2 electrode (a) before and (b) after electrolysis.

Figure 2-9 FE-SEM of the defective 200 nm n^+-Si/SiO_2 electrode

(a) before and (b) after electrolysis.

Figure 2-10 Cyclic voltammograms of the defective 200 nm n^+-Si/SiO_2 electrode in large potential range with or without metal (Pd, Cr) deposition in 1 mM $Ru^{2+/3+}$ + 0.5 M H_2SO_4 aqueous solution. The metals were deposited on the electrodes that had been through 3 days of electrolysis. In case of Pd deposited dielectric electrode, slight oxidative current is observed at approximately + 4.5 V that is far more positive than the redox potential of $Ru^{2+/3+}$, approximately −0.2 V. Probably electron tunneling upon a high overpotential is responsible for it.

Figure 2-11 (a) Raman spectra of n^+-Si/SiO_2 in ambient before and after electrolysis. (b) Electrochemical Raman spectra of n^+-Si/SiO_2 in 0.5 M H_2SO_4 aqueous solution at − 1.67 V to see the influence of electrochemical bias.

Figure 2-12 (a) EELS of n^+-Si/SiO_2 before electrolysis in (a) horizontal and (b) vertical line profile.

Figure 2-13 (a) EELS of n^+-Si/SiO_2 after electrolysis in (a) horizontal and (b) vertical line profile.

Figure 2-14 XPS of n^+-Si/SiO_2 (a) before (black) and (b) after (red) electrolysis.

Figure 2-15 Cyclic voltammograms of the defective 200 nm n^+-Si/SiO_2 electrode comparison upon long period of electrolysis. The working solution was 5 mM ANTH + 1 mM BP + 1 M $HClO_4$ in MeCN.

Figure 2-16 Linear sweep voltammograms of **1a** on defective 200 nm n^+-Si/SiO_2 dielectric electrode in acidic MeCN and N_2 atmosphere. Cyclic voltammogram of **1a** on glassy carbon electrode is attached for

Figure 2-27 LC-MS of the proposed intermediate captured by TEMPO. The large version is attached on section 3.3.5.

Figure 2-28 Schematic illustration of two probable mechanisms of ANTH reaction at conductor electrode other than the defective 200 nm n^+-Si/SiO_2.

Figure 2-29 Electrolysis of ANTH in 1 M $HClO_4$-MeCN at carbon rod as working electrode in (a) air and (b) N_2 atmosphere for 12 h. The applied voltages were − 1.17 V and − 1.67 V respectively.

Figure 2-30 UV-VIS spectra of the electrolysis products of ANTH in 1 M $HClO_4$-MeCN with various conventional working electrodes (conductors) in N_2 atmosphere for 12 h. The applied voltages are −1.67 V and −2.17 V, which are lower and higher than the 1st reduction potential of ANTH ($E_{c1,\,1/2}^{o}$ = −2.02 V), respectively.

Figure 2-31 Electrolysis of ANTH in 1 M $HClO_4$-MeCN with a bare n^+-Si (native oxide etched completely) as working electrode in N_2 atmosphere for 64 h (nearly 3 days) with − 1.67 V bias. (a) *i*-*t* curve and (b) UV-VIS spectra. The change of the quantity of ANTH was checked by UV-VIS spectra.

Figure 2-32 Crossover check of ANTH in H-type divided cell with Nafion® membrane for 64 h.

Figure 2-33 Stability check of ANTH in 1 M $HClO_4$-MeCN solution.

Figure 2-34 The raw data of ^{1}H-NMR of the product mixture of anthraquinone (AQ, **2a**) after the electroorganic reaction of anthracene (ANTH, **1a**) for days on defective 200 nm n^+-Si/SiO_2.

Figure 2-35 The raw data of LC-MS of the product mixture of anthraquinone (AQ, **2a**) after the electroorganic reaction of

anthracene (ANTH, **1a**) for days on defective 200 nm n^+−Si/SiO_2. Biphenyl was included as the internal standard.

Figure 2−36 The raw data of ^{1}H−NMR of the product mixture of anthraquinone (AQ, **2a**) after the electroorganic reaction of anthracene (ANTH, **1a**) for 12 h on defective 200 nm n^+−Si/SiO_2.

Figure 2−37 The raw data of LC−MS of the product mixture of anthraquinone (AQ, **2a**) after the electroorganic reaction of anthracene (ANTH, **1a**) for days on defective 200 nm n^+−Si/SiO_2. Biphenyl was included as the internal standard.

Figure 2−38 The raw data of LC−MS of the product mixture of 2−methylanthraquinone (2−Me−AQ, **2b**) after the reaction of 2−methylanthracene (2−Me−ANTH, **1b**) for days on defective 200 nm n^+−Si/SiO_2. Biphenyl was included as the internal standard.

Figure 2−39 The raw data of LC−MS of the product mixture of 9−anthracenecarboxaldehyde (9−CHO−ANTH, **2c**) after the reaction of 9−methylanthracene (9−Me−ANTH, **1c**) for days on defective 200 nm n^+−Si/SiO_2. Biphenyl was included as the internal standard.

Figure 2−40 The raw data of LC−MS of the product mixture of anthraquinone (AQ, **2a**) after the reaction of 9−anthracenecarboxylic acid (9−COOH−ANTH, **1d**) for days on defective 200 nm n^+−Si/SiO_2. Biphenyl was included as the internal standard.

Figure 2−41 The magnified version of Figure 2−27, LC−MS attached. Intermediate capture of ANTH (**1a**) reaction on n^+−Si/SiO_2 with TEMPO.

Figure 2−42 The raw data of ^{1}H−NMR of **1a**.

Figure 2−43 The raw data of LC−MS of **1a**.

Representative image of directly electrodeposited thin film of metal NPs on n^+−Si/SiO_2 dielectric electrode. (c) Hydrogen gas sensing behavior of the fabricated sensor based on the electrodeposited thin film of Pd NPs on n^+−Si/SiO_2 dielectric electrode.

Figure 3−2 Schematic illustration of the metal electrodeposition directly by hydrogen atom mediated electrochemistry on chemically modified of n^+−Si/SiO_2 surfaces.

Figure 3−3 Schematic diagram of the fabrication of hydrogen gas sensor and measurement of its gas sensing property upon applied bias.

Figure 3−4 Electrodeposited Pd on various surface of modified n^+−Si/SiO_2 electrode. The experimental condition for electrodeposition was N_2−purged solution of 0.5 mM $PdCl_2$ and 0.1 M potassium phosphate (pH 3) applying −1.5 V for 30 min (a) on pristine SiO_2, (b) n^+−Si/SiO_2−NH_2, and (c) n^+−Si/SiO_2−NH_2−AuNP. Scale bars are 100 nm, 200 nm and 200 nm respectively from (a) to (c).

Figure 3−5 Pd film on n^+−Si/SiO_2−NH_2−AuNP. Pd was electrodeposited by applying −0.9 V (vs. Ag/AgCl) for 30 min on n^+−Si/SiO_2−AuNP. (a) FE−SEM image of the surface. (b) Magnified view of (a). (c) Cross−sectional view after FIB dissection. Scale bars are 200 nm, 100 nm and 100 nm respectively from (a) to (c).

Figure 3−6 FESEM images after various metal electrodeposition on n^+−Si/SiO_2. (a) FESEM image of electrodeposited Pt on n^+−Si/SiO_2−NH_2−AuNP. Scale bar, 200 nm. Pt was deposited at −1.7 V (vs. Ag/AgCl) for 30 min on n^+−Si/SiO_2−NH_2−AuNP in 1 mM H_2PtCl_6 and 0.1 M K_2SO_4 at pH 3.4 (b) FESEM image of electrodeposited Cu on n^+−Si/SiO_2−NH_2−AuNP. Cu deposits were prepared at −1.3 V for 30

min in the solution of 1 mM $CuSO_4$ in 0.1 M potassium phosphate at pH 3 on the n^+−Si/SiO_2−NH_2−AuNP. (c) FESEM image of electrodeposited Au on n^+−Si/SiO_2−NH_2−AuNP. Au deposits were prepared at −1.5 V for 30 min in the solution of 1 mM $KAuCl_4$ in 0.1 M potassium phosphate at pH 3 on the n^+−Si/SiO_2−NH_2−AuNP. (d) FESEM image of electrodeposited Ni on n^+−Si/SiO_2−NH_2−AuNP. Ni deposits were prepared at −1.5 V for 30 min in the solution of 1 mM $NiSO_4$ in pH 3.8 aqueous boric acid on the n^+−Si/SiO_2−NH_2−AuNP. Scale bar 200 nm.

Figure 3−7 Characterization of Pt electrodeposited on n^+−Si/SiO_2−NH_2−AuNP. (a) Au 4f core level XPS spectrum (Au 4f peak: 84.000, 87.679, 85.231 eV) (b) Pt 4d core level XPS spectrum (Pt 4d peak: 315.392, 332.259 eV) (c) Pt 4f core level XPS spectrum (Pt 4f peak: 75.740, 72.736 eV) of Au−Pt NPs on the n^+−Si/SiO_2 (d) EDS spectrum.

Figure 3−8 Characterization of electro−deposited Cu on n^+−Si/SiO_2−NH_2−AuNP. (a) Au 4f core level XPS spectrum (Au 4f peak: 83.83, 87.49 eV) (b) Cu 2p core level XPS spectrum (Cu 2p peak: 932.27, 933.54 eV) (c) EDS spectrum.

Figure 3−9 Characterization of electrodeposited Ni on n^+−Si/SiO_2−NH_2−AuNP. (a) Au 4f core level XPS spectrum (Au 4f peak: 83.26, 86.93, 83.86, 87.53 eV) (b) Ni 2p core level XPS spectrum (Ni 2p peak: 856.15 eV) (c) EDS spectrum.

Figure 3−10 Electrochemical behavior comparison at n^+−Si/SiO_2−NH_2 and n^+−Si/SiO_2−NH_2−AuNP. (a) Nyquist plots by impedance spectroscopy at −1.2 V (vs. Ag/AgCl) on n^+−Si/SiO_2−NH_2 (black squares) and n^+−Si/SiO_2−NH_2−AuNP (red circles) in 0.1 M

potassium phosphate buffer at pH 3. (b) The *i*–*V* curves obtained from N_2–purged solution of 0.5 mM $PdCl_2$ and 0.1 M potassium phosphate (pH 3) with scan rate of 10 mV/s.

Figure 3–11 Characterization of electrodeposited Pd on n^+–Si/SiO_2–NH_2–AuNP. (a) Pd 3d core level XPS spectrum (Pd 3d peak: 335.891, 341.966, 337.473 eV) (b) Au 4f core level XPS spectrum (Au 4f peak: 84.000, 87.685, 85.621 eV) (c) HAADF–STEM image. Scale bar 10 nm. (d) EDS spectrum at the point of "spectrum 1" in c.

Figure 3–12 Performance of the resistance–based H_2 gas sensor prepared via direct electrodeposition of Pd thin metal film on n^+–Si/SiO_2–NH_2–AuNP. The real–time resistance responses to various H_2 gas partial pressure which the flow was programmed for 1000 sccm gas flow at room temperature in the range of (a) 0.1 – 5% with 2 mV bias and (b) 100 – 2000 ppm with 10 mV bias. (c) Plot of sensitivity response as a function of H_2 partial pressure with 2 mV bias.

Figure 3–13 Performance of the hydrogen gas sensor of electrodeposited thin film of Pd NPs on n^+–Si/SiO_2–NH_2–AuNP. Plots of sensitivity as a function of H_2 partial pressure with (a) 5 mV and (b) 10 mV applied bias.

List of Tables

gas sensors.

1. Introduction

1.1 Background and Overview

1.1.1 Electrochemistry on insulator

Electrochemistry on the insulator is counterintuitive since the charge carrier concentration is extremely low in the insulator. However, there have been few reports of the faradaic reaction on insulator and are worth to be noted to breakdown the common sense and open the new vision on scientific findings.

The previous reports of these in the last decade can be classified into three categories. Firstly, the static electricity generated by contact electrification of the dielectric materials [1−6]. Reported by A. J. Bard group, electrostatic charges on Teflon was produced by rubbing with Lucite (PMMA) and the charged Teflon was used to demonstrate electrochemical reaction: pH increase, hydrogen formation, copper deposition, $Fe(CN)_6^{3-}$ reduction, and electrochemiluminescence of $Ru(bpy)_3^{2+}$ with $S_2O_8^{2-}$, etc [1]. In case of PMMA surface after contact electrification, the reducing strength was abnormally strong by the static charge density as up to 160 $\mu C/cm^2$ [1]which is 5 orders of magnitude higher than the in the air [3]. Such charge was described as cryptoelectrons meaning “hidden”

electrons [2]. Further research by a few groups modified the early version of the idea. B. A. Grzybowski group, the mosaic of surface charge in contact electrification was reported by imaging with Kelvin–probe force microscopy where it has been generally assumed that one charge uniformly positive and the other negatively [3]. In addition, the main counter–explanation arose in which the key role of the electrochemical reaction was driven by ions or free radicals rather than cryptoelectrons. They suggested that the charge was probably overestimated due to the absorption of the reactant [4]. To more expansion of the material choice, contact electrification was demonstrated between metal Au and PDMS insulator and the static electricity on Au was sufficiently strong enough to promote electrochemical reaction [6]. Importantly the main driving force of the reaction was again the ion and radicals rather than the pure electron.

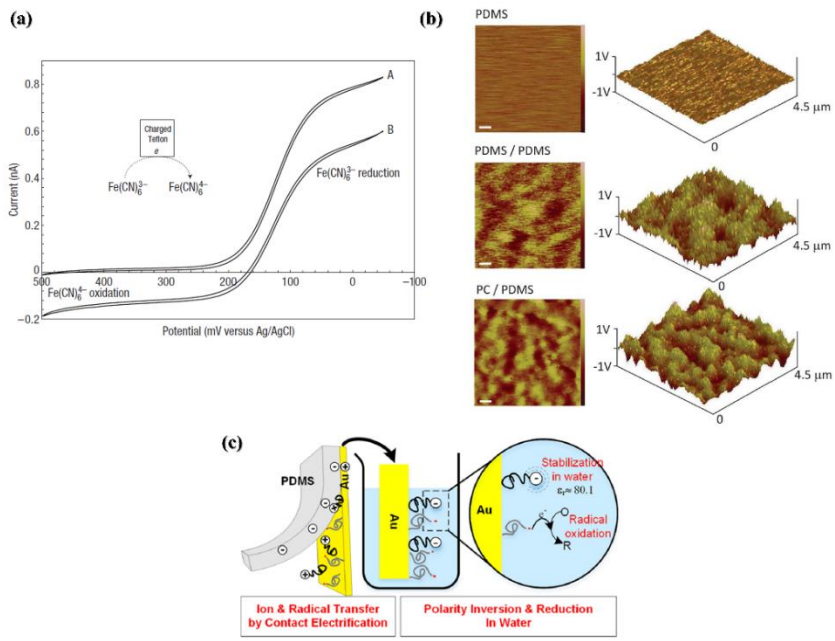

Fig. 1-1 (a) Electrochemical reaction of $Fe(CN)_6^{3-}$ by charged Teflon after contact electrification [1]. (b) The mosaic of charges after contact electrification by Kelvin-probe force microscopy [3]. (c) An electrochemical reaction is driven by ion and free radical by contact electrification [6].

Secondly, the electrochemistry through the glass was proposed [7]. It was demonstrated by the faradaic reaction after acid solution treatment of the nanometer-thick borosilicate glass-covered Pt nanoelectrode which was confirmed to have no pinholes. The hydrated glass film soaked by 6 M HCl for a few hours turns into a hydrogel-like state, affords the faradaic reaction of redox couples of outer-sphere electron transfer. This was suggested by the permselectivity of hydrated glass films: change of voltammograms

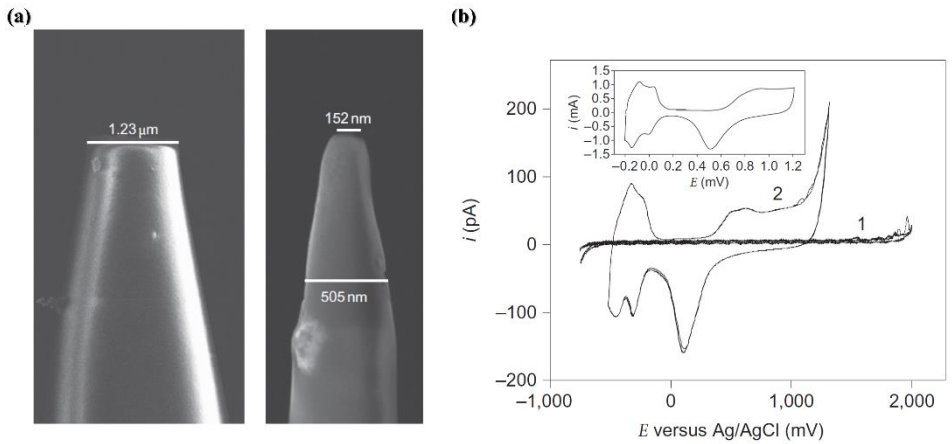

Fig. 1-2 The electrochemistry through borosilicate glass-covered Pt nanoelectrode. (a) SEM of the nanoelectrode. (b) Cyclic voltammetry of 0.5M H_2SO_4 solution before 1 and after 2 an electrode was soaked overnight after pre-treatment with 6 M HCl [7].

upon the charge of redox couples. Note that this is not like the electrode for pH meter, a passive potentiometric electrode involving no faradaic process.

Thirdly, electrochemistry at the thin film of thermal SiO_2. This is the main theme of this dissertation and is discussed in the next section.

1.1.2 Electrochemistry on thermal SiO_2: hydrogen atom mediated electrochemistry

Silicon dioxide (SiO_2) layer is a common insulating material and is generally used as the gate oxide in the semiconductor industry.

Therefore, their tunneling of charge carriers through the gate oxide was mainly studied in metal–oxide–semiconductor (MOS) system. It is well known that the scarce charges in the oxide originate from the chemical defects such as dangling bonds or atom vacancy in the SiO_2 and Si/SiO_2 interface. In addition, the presence of impurities such as Na, K, Li, [8] and mobile H (their charges either positive or neutral in general) [9] have been observed to sink at the Si/SiO_2 interface due to the relatively low chemical potential in the interface states and traps. If this system is brought into the electrolyte solution to form electrolyte–oxide–semiconductor (EOS) system, its effect is greater for sure.

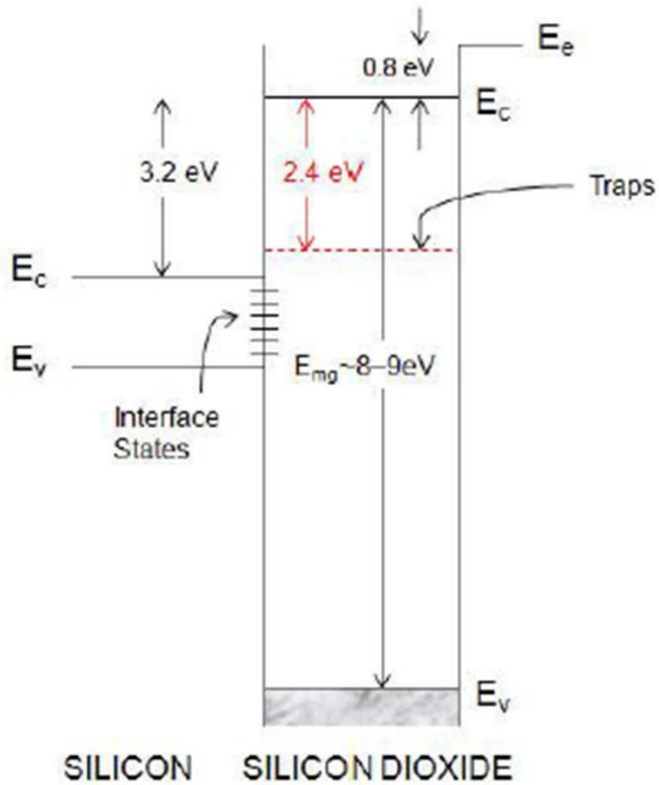

Fig. 1−3 Band model of the Si/SiO_2 interface with interfaces states and traps [10].

Thermal SiO_2 layer has a highly dielectric structure with minimal defects fabricated by oxidation of Si in the furnace. With the underlying conductive substrate as highly n−doped Si (n^+−Si), it constitutes an EOS system when used as the electrode in contact with the solution. It was reported that hydrogen atoms can be produced at the n^+−Si/thermal oxide interface (denote as n^+−Si/SiO_2), being responsible for faradaic current in voltammetry [11]. It is widely supposed that hydrogen atom is meta−stable in SiO_2 and other dielectrics according to the calculations and the studies related

to metal/oxide interface [12,13]. The possibility of diffusion of a hydrogen atom in the dielectric is also well-calculated and experimentally supported in many fields using metal-oxide-semiconductor (MOS) or metal-oxide-metal (MOM) [14,15]. In consideration of the electrical potential profile along the thermal SiO_2, protons selectively permeate along steep voltage gradient across the oxide layer and become reduced at the interface between the SiO_2 and n^+-Si. In addition, silanol defects in the thermal SiO_2 are subject to electrochemical reduction, causing asymmetric voltammetric behavior in acidic aqueous solution (reduction only). Such electrochemical reduction of silanol defect was observed by Raman spectroscopy [11]. In addition, the electrochemical behavior clearly deviated from Fowler-Nordheim (F-N) tunneling. In short, such thermal SiO_2 layer permits both the selective migration of protons and the diffusion of the hydrogen atoms, acting as "chemical electrode". As a consequence, it is possible to directly electroplate metals on the dielectric surface and gas reaction such as CO_2 reduction [11,16,17].

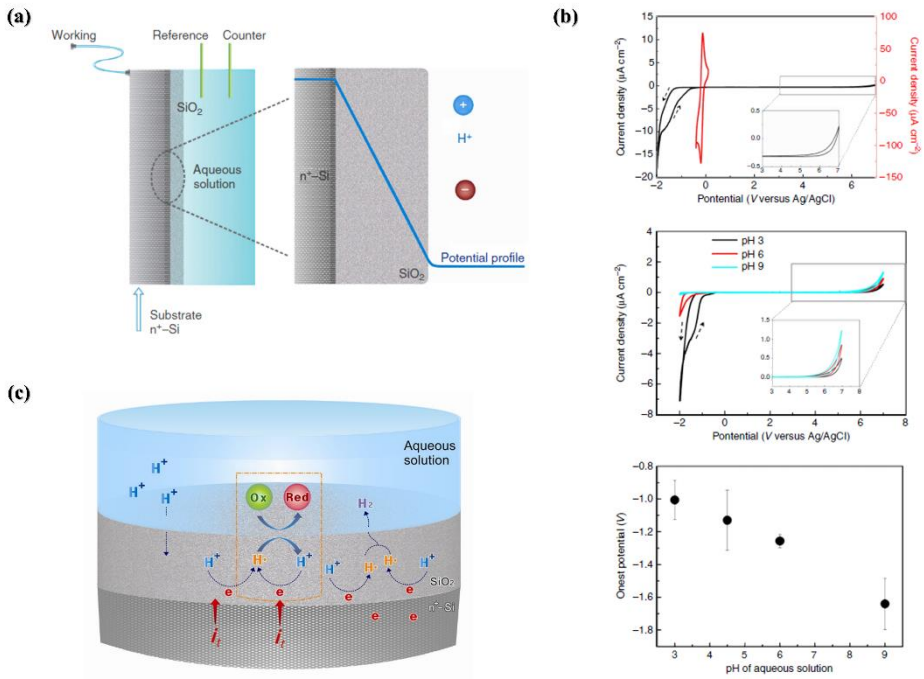

Fig. 1-4 (a) Schematic illustration of the experimental system and the electrical potential profile across n^+-Si/SiO_2/aqueous electrolyte. (b) Electrochemistry of the proposed EOS system. (top) The comparison of cyclic voltammograms on 6 nm n^+-Si/SiO_2 (black) and glassy carbon electrode (red), (middle) the comparison upon pH change, and (bottom) pH dependence of onset potentials. (c) Schematic view of the reactions in the proposed system: H-atom-mediated electrochemistry [11].

1.1.3 Perspectives of electrochemistry on dielectric electrode and hydrogen atoms

The common feature among the work of electrochemistry on the insulator is that the research mainly focused on finding the most plausible explanation for the faradaic reaction since it is not perceptive. In this respect, there is an empty space for the research on what kind of chemistry is possible on insulators and what kind of application is possible. Especially, there must be a boundless field of chemistry brought into hydrogen atom if it is really generated in such system. More importantly, hydrogen atom itself is known to inherently possess diverse reactivity towards chemicals: reduction, radical reaction, and even oxidation.

The direct use of hydrogen atom was reported by the gamma-ray radiolysis of water [18-22]. Such a way in aqueous solution produces hydrogen atoms and hydroxyl radicals which were utilized to provoke chemical reactions. Buxton *et al.* surveyed what kind of chemical reactions were possible by hydrogen atom [22]. They were reduction, oxidation, and radical reaction initiated by hydrogen atom abstraction (HAA). The hydrogen atom, a strong reducing agent (−2.106 V vs NHE) [18], may involve in reduction and radical reaction but oxidation is counterintuitive. According to the previous reports, oxidation by hydrogen atom can occur in strongly acidic media. There were two cases. First, the reaction between hydrogen atoms with Fe^{2+} forms the intermediate in the state of $Fe^{3+}-H^{-}$ followed by

abstraction of hydride by proton, resulting in Fe^{3+} and H_2 as the products. Similarly, the second case of the reaction of a hydrogen atom with 2 equivalent of I^- form the state of HI_2^{2-}, followed by the same manner to produce I_2^-. In summary, two reactions were the counter half-reaction of the following reduction: $H\cdot + H^+ + e^- = H_2$ (−2.30 V vs NHE). The radical reaction, on the other hand, is simply initiated by the abstraction of hydrogen atom, followed by radical cascade. Note that this kind of initiation is similar to the many HAA reactions and proton-coupled electron transfer (PCET) in organic chemistry [23-25]. The distinguishable characteristic is that the C-H activated reactant in such way generally undergoes oxidation or oxidative addition for various C-C coupling or functionalization.

Currently, hydrogen atom, composed of a single proton and a single electron, is the most basic element in chemistry and plays important roles in many fields of science. The adsorbed hydrogen atoms at the catalysts are understood to be the key intermediate species in the fields of development of clean fuels and chemical conversions such as water splitting [26-28], electrochemical CO_2 or CO reduction [29-33], catalytic and electrocatalytic hydrogenation (ECH) in biomass-derived chemical conversion [29,34-37], etc. In terms of the organic synthetic chemistry and biochemical processes such as photosynthesis, hydrogen atom plays an essential role in the version of HAA or hydrogen atom transfer (HAT) reactions, and HAT catalysts [38-42].

The roles the hydrogen atom in chemical reactions mentioned above, however, are all “supposed ideas” although they are widely considered to be acceptable. There is no direct evidence of them. The most common way to electrochemically generate hydrogen atom is the use of electrode adsorbed hydrogen atom intermediate in the process of electrochemical hydrogen evolution reaction (HER): Volmer ($H^+ + e^- \rightarrow H{\cdot}_{ads}$) reaction, especially in the field of ECH [34,35,37]. In case of HAT related studies, hydrogen atoms are proposed by careful analysis of the products and possible reaction pathways, also without direct evidence [38,41].

In short, the majority of researches on chemical reactions using hydrogen atom focused on either excessive generation by Volmer reaction or C−H activation by the net abstraction of the hydrogen atom using a catalyst. The direct formation of the hydrogen atom by gamma−ray radiolysis is too harsh and cannot be popularly equipped. In order to effectively utilize the hydrogen atom, the EOS system of thermal SiO_2 dielectric electrode may serve a good platform to be utilized.

1.2 References

[1] C. Y. Liu, A. J. Bard, *Nat. Mater.*, 2008, *7*, 505.

[2] C. Y. Liu, A. J.; Bard, *J. Am. Chem. Soc.*, 2009, *131*, 6397.

[3] H. T. Baytekin, A. Z. Patashinski, M. Branicki, B. Baytekin, S. Soh, B. A. Grzybowski, *Science*, 2011, *333*, 308.

[4] S. Piperno, H. Cohen, T. Bendikov, M. Lahav, I. Lubomirsky, *Phys. Chem. Chem. Phys.*, 2012, *14*, 5551.

[5] H. T. Baytekin, B. Baytekin, S. Huda, Z. Yavuz, B. A. Grzybowski, *J. Am. Chem. Soc.*, 2015, *137*, 1726.

[6] C. Yun, S. H. Lee, J. Ryu, K. Park, J. W. Jang, J. Kwak, S. Hwang, *J. Am. Chem. Soc.*, 2018, *140*, 14687.

[7] J. Velmurugan, D. P. Zhan, M. V. Mirkin, *Nat. Chem.*, 2010, *2*, 498.

[8] P. O. Hahn, M. Henzler, *J. Vac. Sci. Technol. A*, 1984, *2*, 574.

[9] S. R. Hofstein, *IEEE T. Electron. Dev.*, 1967, *14*, 749.

[10] R. Enderlein, N. J. Horing, *Fundamentals of Semiconductor Physics and Devices*, 1997, 567−572.

[11] J. Y. Lee, J. G. Lee, S. H. Lee, M. Seo, L. Piao, J. H. Bae, S. Y. Lim, Y. J. Park, T. D. Chung, *Nat. Commun.*, 2013, *4*, 2766.

[12] A. Yokozawa, Y. Miyamoto, *Phys. Rev. B*, 1997, *55*, 13783.

[13] I. A. Shkrob, B. M. Tadjikov, S. D. Chemerisov, A. D. Trifunac, *J. Chem. Phys.*, 1999, *111*, 5124.

[14] T. Whittaker, K. B. S. Kumar, C. Peterson, M. N. Pollock, L. C. Grabow, B. D. Chandler, *J. Am. Chem. Soc.*, 2018, *140*, 16469.

[15] A. J. Tan, M. Huang, C. O. Avci, F. Buttner, M.Mann, W. Hu, C. Mazzoli, S. Wilkins, H. L. Tuller, G. S. D. Beach, *Nat. Mater.*, 2019, *18*, 35.

[16] J. G. Lee, J. -Y. Lee, J. Yun, Y. Lee, S. Lee, S. J. Shin, J. H. Bae, T. D. Chung, *Electrochem. Commun.*, 2017, *76*, 75.

[17] J. Y. Lee, S. J. Shin, J. G. Lee, J. Yun, M. A. Oh, T. D. Chung, *J. Electrochem. Soc.*, 2017, *164*, D1.

[18] A. A. Bergh, *At&T Tech. J.*, 1965, *44*, 261.

[19] M. Anbar, D. Meyerstein, P. Neta, P., *Nature*, 1966, *209*, 1348.

[20] M. Anbar, E. J. Hart, *On the Reactivity of Hydrated Electrons Toward Inorganic Compounds. In Radiation Chemistry*, 1968, pp 79-94.

[21] H. A. Schwarz, *J. Chem. Edu.*, 1981, *58*, 101.

[22] G. V. Buxton, C. L. Greenstock, W. P. Helman, A. B. Ross, *J. Phys. Chem. Ref. Data*, 1988, *17*, 513.

[23] E. C. Gentry, R. R. Knowles, *Acc. Chem. Res.*, 2016, *49*, 1546.

[24] S. Ghosh, J. Castillo-Lora, A. V. Soudackov, J. M. Mayer, S. Hammes-Schiffer, *Nano Lett.*, 2017, *17*, 5762.

[25] W. D. Morris, J. M. Mayer, *J. Am. Chem. Soc.*, 2017, *139*, 10312.

[26] C. G. Morales-Guio, L. A. Stern, X. L. Hu, *Chem. Soc. Rev.*, 2014, *43*, 6555.

[27] Y. Zheng, Y. Jiao, Y. H. Zhu, L. H. Li, Y. Han, Y. Chen, A. J. Du, M. Jaroniec, S. Z. Qiao, *Nat. Commun.*, 2014, *5*, 3783.

[28] N. C. Cheng, S. Stambula, D. Wang, M. N. Banis, J. Liu, A. Riese, B. W. Xiao, R. Y. Li, T. K. Sham, L. M. Liu, G. A. Botton, X. L. Sun, *Nat. Commun.* 2016, *7*, 13638.

[29] Y. Fang, J C. Flake, *J. Am. Chem. Soc.*, 2017, *139*, 3399.

[30] W. Lin, K. M. Stocker, G. C. Schatz, *J. Am. Chem. Soc.*, 2017, *139*, 4663.

[31] C. G. Morales-Guio, E. R. Cave, S. A. Nitopi, J. T. Feaster, L. Wang, K. P. Kuhl, A. Jackson, N. C. Johnson, D. N. Abram, T. Hatsukade, C. Hahn, T. F. Jaramillo, *Nat. Catal.*, 2018, *1*, 764.

[32] X. Y. Liu, P. Schlexer, J. P. Xiao, Y. F. Ji, L. Wang, R. B. Sandberg, M. Tang, K. S. Brown, H. J. Peng, S. Ringe, C. Hahn, T. F. Jaramillo, J. K. Norskov, K. R. Chan, *Nat. Commun.*, 2019, *10*, 32.

[33] X. L. Zheng, Y. F. Ji, J. Tang, J. Y. Wang, B. F. Liu, H. G. Steinruck, K. Lim, Y. Z. Li, M. F. Toney, K. Chan, Y. Cui, *Nat. Catal.*, 2019, *2*, 55.

[34] P. Nilges, U. Schröder, *Energy Environ, Sci.*, 2013, *6*, 2925.

[35] S. Jung, E. J. Biddinger, *ACS Sust. Chem. Eng.*, 2016, *4*, 6500.

[36] N. Singh, Y. Song, O. Y. Gutiérrez, D. M. Camaioni, C. T. Campbell, J. A. Lercher, *ACS Catal.*, 2016, *6*, 7466.

[37] X. H. Chadderdon, D. J. Chadderdon, J. E. Matthiesen, Y. Qiu, J. M. Carraher, J. P. Tessonnier, W. Li, *J. Am. Chem. Soc.*, 2017, *139*, 14120.

[38] J. L. Jeffrey, J. A. Terrett, D. W. C. MacMillan, *Science*, 2015, *349*, 1532.

[39] C. C. Wang, H. C. Chang, Y. C. Lai, H. Y. Fang, C. C. Li, H. K. Hsu, Z. Y. Li, T. S. Lin, T. S.; Kuo, F. Neese, S. F. Ye, Y. W. Chiang, M. L. Tsai, W. F. Liaw, W. Z. Lee, *J. Am. Chem. Soc.*, 2016, *138*, 14186.

[40] A. Baschieri, L. Valgimigli, S. Gabbanini, G. A. DiLabio, E. Romero-Montalvo, R. Amorati, *J. Am. Chem. Soc.*, 2018, *140*, 10354.

[41] W. Nam, Y. M. Lee, S. Fukuzumi, *Acc. Chem. Res.*, 2018, *51*, 2014.

[42] T. Gunasekara, G. P. Abramo, A. Hansen, H. Neugebauer, M. Bursch, S. Grimme, J. R. Norton, *J. Am. Chem. Soc.*, 2019, *141*, 1882.

2. Cathodic Electroorganic Reaction on Silicon Oxide Dielectric Electrode

2.1 Introduction

Electrosynthesis is a conventional way of synthesis that activates the reactant by a faradaic reaction to provoke the electroorganic reaction. In most cases, it involves electrochemical stimulation of oxidative addition [1-5], C-H activation [3-6], and C-C coupling [1,5,7-10], etc. Fueled by the effort to substitutes for chemical additives (i.e. acid/base, oxidant/reductant, and catalysts) to supply/abstract of an electron, intense studies of electrosynthesis have been conducted especially in the last decade as an economic and sustainable strategy. [11]. While interests are centered at organic synthesis, the electrode material employed for the studies, however, receives little attention so that only a few options are available. The electrode materials have been mostly conductors and semiconductors for the purposes of electroanalysis, electrocatalysis, and so on. This is true as well for electroorganic reactions, for which the electrodes are more limited to conventional conductors such as carbon or boron-doped diamond [5].

In general, electroorganic reactions prefer chemically inert material for the electrode. Although catalytic electrode material could accelerate the electroorganic reaction and furnish various products of interest, its surface is hardly stable to sustain the yield of a given reaction. As electrochemical reaction inherently involves heterogeneous electron transfer, any specific adsorption may make the system out of control leading to passivation or unexpected results. That is why electrosynthesis studies normally utilize carbon or boron-doped diamond, which is not perfect but better than other options, fulfilling a large part of the conditions. It should be noted that the electrode in electrosynthesis to date has been expected to serve as nothing but an electron sink for electrochemical oxidation.

As to mention, there is a unique method in electrochemistry which deserves consideration, known as the faradaic reaction at the insulator thin film [12-20]. Electrochemistry on the insulator, in which very limited density of charge carriers exist, is unusual, and thus hardly found in the literature. These previous reports can be classified into three categories and are described in detail in Chapter 1. The first is the static electricity generated by contact electrification of the dielectric materials. Kelvin-probe microscopy showed a mosaic of positive and negative charges that could drive the electrochemical reduction of metal ions and metal-complex [12,13,15,17,20]. The second is the faradaic reaction through the glass, which was demonstrated on borosilicate glass covered with a

few nanometer thick on Pt nanoelectrode [14]. The investigation of its voltammetry by ruthenium redox couple in this system suggested the hydrogel-like state of glass in strong acid, similar to the behavior of glass pH sensor. Note that this is not like the electrode for pH meter, a passive potentiometric electrode involving no faradaic process.

The third is the electrochemistry at the thin film of thermal SiO_2 [16,18,19]. The details are discussed in Chapter 1. In short, hydrogen atoms can be generated at the n^+-Si/thermal oxide interface, bringing about apparent faradaic current in voltammetry. This stems from the reduction of protons that permeate by selective migration under steep voltage drop across the dielectric layer. In addition, electrochemical reduction of the silanol defects in the thermal SiO_2 leads to an asymmetric voltammetric behavior in acidic aqueous solution (reduction only). After all, such thermal SiO_2 layer permits both the selective migration of protons and the diffusion of the hydrogen atoms, acting as a "chemical electrode". As a consequence, it is possible to directly electroplate metals on the dielectric surface [16,19]. From this, it can be inferred that this may trigger the electrochemical reaction between the generated hydrogen and the organic reactant in the electrolyte.

Electroorganic reactions could benefit from the electrochemistry on thermal SiO_2. The surface of thermal SiO_2 where the electroorganic reaction occurs possibly prevents chemical fouling

compared to most of the electrocatalysts. A good example of chemical fouling is platinum poisoning [21−25]. Nonetheless, it is expected to promote electroorganic reactions that require harsh conditions. The reactive hydrogen atom (−2.30 V vs NHE) [26] are expected to be generated at a strong negative potential. In the case of conventional conductive electrodes, a catastrophic increase in background current should occur in order to generate a hydrogen atom. Moreover, insulator thin film allows avoiding vigorous electrolysis while it electrochemically reduces protons across its film which electric potential gradient is widely distributed. In addition, the electroorganic reaction may be precisely tuned through fine control of current, which is proportional to the reaction rate.

In this work, a defective 200 nm−thickness n^+−Si/SiO_2 was fabricated as a dielectric electrode. It must be mentioned that the notation of defective 200 nm−thickness n^+−Si/SiO_2 implies it has ignorable physical defects of pinholes and cracks but plenty of chemical defects such as dangling bonds or atom vacancies. Its electrochemical behavior was examined to compare previously reported 6 nm−thick n^+−Si/SiO_2. The most significant work was the investigation of cathodic electroorganic reactions of the anthracene and its derivatives which is one of the basic molecule constitutes of polycyclic aromatic hydrocarbons (PAH). The electrolysis was performed in an H−type divided cell and the products were analyzed. Ironically, the “oxidized” products were generated upon “cathodic”

potential, indicating that the dielectric electrode of n^+−Si/SiO_2 does not simply transfer electron but reactive chemical species. Many derivatives of anthracene in the solution commonly showed loss of hydrogen atom bound to the aromatic ring and subsequent addition of oxygen species. Furthermore, the underlying working principle was investigated and must be related to the hydrogen species in the dielectric electrode acting as a “chemical electrode”.

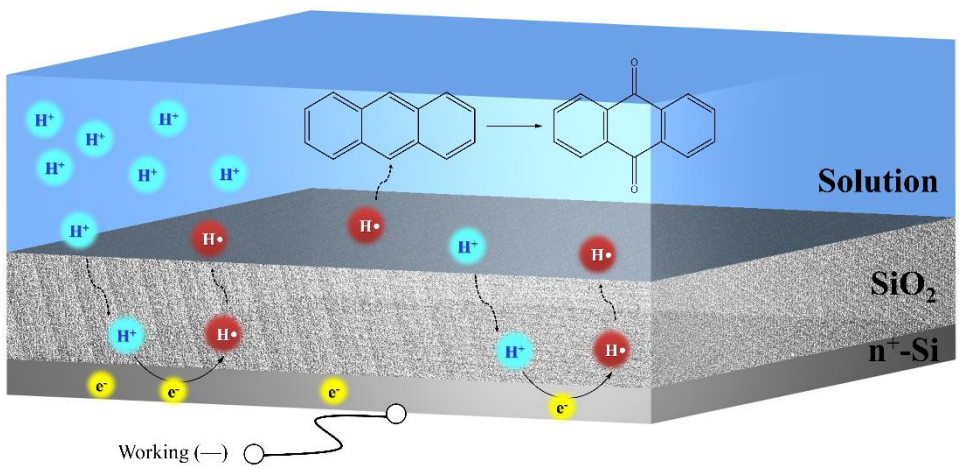

Fig. 2−1 Schematic illustration of the cathodic electroorganic reaction on defective thermal oxide on n^+−Si. The electrolysis is performed in the H−type divided cell. Ironically, the “oxidized” products were generated upon “cathodic” potential.

2.2 Experimental Methods

2.2.1 Reagents and materials

Anthracene (ANTH, **1a**, ≥99.0% GC), anthraquinone (AQ, **2a**, 97%), biphenyl (BP, 99.5%), 2-methylanthracene (2-Me-ANTH, **1b**, 97%), 9-methylanthracene (9-Me-ANTH, **1c**, 98%), 9-anthracenecarboxylic acid (9-COOH-ANTH, **1d**, 99%), phenanthrene (Phen, **3a**, ≥98.0%), pyrene (Py, **4a**, 98%), perchloric acid ($HClO_4$, 70%), trifluoroacetic acid (TFA, 99%), sodium perchlorate ($NaClO_4$, ≥98%), tetrabutylammonium perchlorate (TBAP, ≥99.0%), sodium chloride (NaCl, ≥99.0%), sodium sulfate (Na_2SO_4, ≥99.0%), chloroform-d ($CDCl_3$, ≥99.8 atom % D, 0.5 wt % Ag foil as stabilizer, 0.03 vol % TMS), and water-^{18}O ($H_2{}^{18}O$, 97 atom %) were purchased from Sigma Aldrich. Nitrobenzene ($PhNO_2$, 98.0%) was purchased from TCI chemicals. Sodium hydroxide (NaOH, 98.0%), acetonitrile (MeCN, 99.5%), sulfuric acid (H_2SO_4, 98%), benzene (99.5%), dichloromethane (MC, 99.5%), were purchased from Dae Jung. All chemicals were used without further purification.

2.2.2 Preparation of defective thermal SiO_2

N-type, arsenic-doped, <100> oriented Si (n^+-Si) wafers with

resistivity as low as 0.005 Ω cm, were obtained from STC (Japan). Highly n-doped Si with thermally oxidized SiO_2 (n^+-Si/SiO_2) was produced via oxidation n^+-Si wafers under the oxygen environment at 850 ° C. n^+-Si was cleaned by standard SPM and SC-1,2 cleaning consecutively. Then, the target 200 nm-thick thermal SiO_2 was prepared at 850 ° C in a furnace by blowing O_2. The native oxide was no removed prior to the thermal oxidation. Note that not all the defective thermal SiO_2 show faradaic current upon negative bias. The electrodes were tested by voltammetry prior to electrolysis to discard the total insulator (roughly one out of four were discarded). This is deemed to be ascribed to the inhomogeneous defect density of the SiO_2 layer.

2.2.3 Electrochemical setup and electrolysis

The wafer samples were degreased by sonication in acetone and isopropanol, and rinsed with methanol or deionized water (DI water). For back contact, the backside of the wafer sample was scratched with a diamond knife to remove the air-formed SiO_2 followed by smearing with a eutectic of Ga-In (≥99.99% trace metal basis from Sigma Aldrich). Electrochemical characterization was performed by a conventional three-electrode cell connected to electrochemical analyzers (CHI 660 and 750, CH Instrument). Pt wire (diameter of 0.5 mm) was employed as the counter electrode. The reference electrodes were Ag/Ag^+ (10 mM $AgNO_3$ + 0.1 M TBAP in MeCN,

BAS Inc.) and Ag/AgCl (3 M NaCl, BAS Inc.). The former was employed for the MeCN-rich solution and the letter for a water-rich solution. All potentials refer to the saturated calomel reference electrode (SCE). In short, Ag/Ag^+ was +0.327 V versus SCE in not distilled acetonitrile.

Electrolysis was performed in a home-made H-type divided cell (Fig. 2-2) with working and counter electrode (WE and CE) chambers separated by Nafion® 117 proton exchange membrane (0.007-inch thickness, Sigma Aldrich). It was carried out in 10 mL each in chambers for days. WE chamber was stirred 300 rpm and purged with N_2 gas (99.999%) throughout the reaction. Typical electrolysis solution in WE chamber composed of 5 mM of starting compound with 1 M acid dissolved MeCN. The CE chamber was filled with an acid-electrolyte solution. The O-rings were all SuperViton® and the rings for Nafion® separator were Teflon-taped to shorten the inner diameter of ~1 mm to minimize crossover.

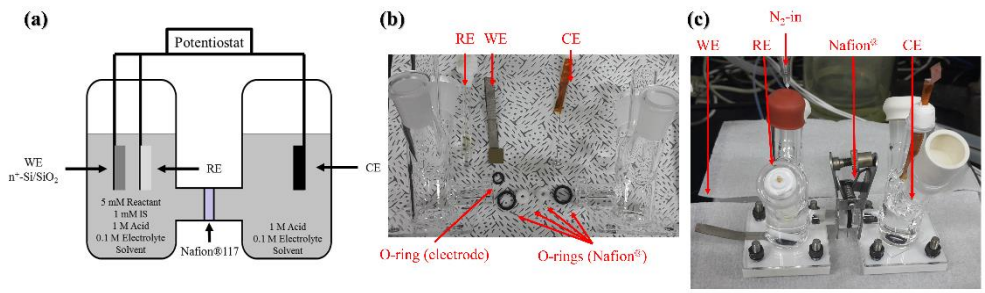

Fig. 2-2 (a) Diagram and photo of (b) before and (c) after assembly of a home-made H-type divided cell with Nafion® membrane for electrolysis.

2.2.4 Product analysis

UV-VIS measurements using a UV-VIS spectrometer (UV-VIS; Cary 60 G6860A, Agilent Technologies) were performed to check spectrum change prior to collection. Liquid aliquots from electrolysis were collected for work-up to remove excessive acids prior to chemical analyses. An equivalent volume of benzene was mixed with collected liquid aliquots and 2 equivalent volumes of saturated aqueous NaCl solution to separate the aqueous electrolyte layer and the organic solvent layer. The organic layer was extracted from the mixture and subsequently dried using anhydrous sodium sulfate. The products were analyzed using a high-performance liquid chromatography-mass spectrometer (LC-MS/MS; LCMS-8050, Shimadzu). For quantification, biphenyl was chosen as an internal standard and put into the WE chamber prior to electrolysis. We obtained quantitative results based on standard calibration. ^{1}H-NMR was obtained by 300 MHz (AVANCE DPX-300, Bruker).

The detailed method for quantitative analyses by UV-VIS is as follows. As shown in Fig. 2-3, The absorption of ANTH at λ_{357nm} and AQ at λ_{272nm} did not overlap, thereby appropriate to be calculated using Beer's law:

$$A = \varepsilon dC \qquad \text{(eq. 2-1)}$$

where A: absorbance, ε : molar extinction coefficient, d: cell length, and C: concentration. In addition, λ_{251nm} could be used for quantification of crossed amounts from WE to CE. The linear

calibration curve was obtained from standard ANTH and AQ solution in MeCN. The slope and the intercept are summarized in Table 2-1. The cell length for UV-VIS measurement was 1 cm, so the absorbance and the concentration relation is written as the following.

$$A = \varepsilon C + b \qquad \text{(eq. 2-2)}$$

where A: absorbance, ε : molar extinction coefficient, corresponding to the slope ($M^{-1}\cdot cm^{-1}$), C: concentration (M), and b: intercept.

The percentage consumption of ANTH could be calculated as follows.

$$\text{Consumption } (\%) = 100 \cdot \frac{C_i - C_f}{C_i} = 100 \cdot \frac{A_i - A_f}{A_i - b} \qquad \text{(eq. 2-3)}$$

where the subscript i is initial and f is final. This calculation is valid at λ_{357nm}.

The percentage generation of AQ could be calculated as shown below.

$$\text{Generation } (\%) = 100 \cdot \frac{C_f - C_i}{C_{i,ANTH}} = 100 \cdot \varepsilon_{AQ,272nm} \frac{A_f - A_i}{C_{i,ANTH}} \qquad \text{(eq. 2-4)}$$

where $C_{i,ANTH}$ is the initial concentration of ANTH in the working chamber. This calculation is valid at λ_{272nm}.

Note that the volume of the solution in H-type divided cell changes due to the evaporation by continuous N_2 purging. The volume should be checked through the meniscus then adjusted by adding or evaporating the solvent. In addition, similar calculations were also done for the derivative compounds of ANTH (methods not shown).

The detailed method for quantitative analyses by LC-MS is as follows. In order to perform chromatography, the electrolyte and

strong acids must be removed by work-up. The internal standard was dissolved together in the working solution. Biphenyl (BP) was appropriate in that it undergoes neither chemical reaction nor crossover during the experiment. In LC-MS/MS, the signal was detected by selected ion monitoring (SIM) mode for specific m/z. A relative area in LC chromatogram allows quantifications. BP was detected by UV (254 nm, 350 nm) since it was not ionized by atmospheric-pressure chemical ionization (APCI), inappropriate for SIM mode. The calibration curve of each chemical gave quantitative information about the chemical components.

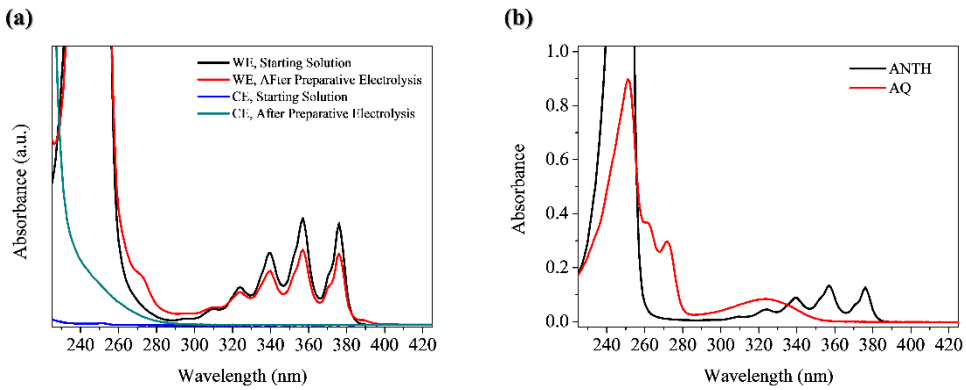

Fig. 2-3 (a) Representative UV-VIS spectra after electrolysis of ANTH to AQ reaction in H-type divided cell by defective 200 nm n^+-Si/SiO_2 dielectric electrode. (b) UV-VIS spectra of standard ANTH and AQ in MeCN for comparison.

	ANTH (λ_{357nm})	ANTH (λ_{251nm})	AQ (λ_{323nm})	AQ (λ_{272nm})	AQ (λ_{251nm})
Slope ($M^{-1}\cdot cm^{-1}$)	7.470E+03	1.522E+03	4.770E+03	1.500E+03	4.519E+04
Intercept	-1.424E-02	3.900E+03	-7.738E-04	-3.020E-03	-5.250E-03

Table 2-1 The slopes and intercepts for ANTH and AQ in MeCN from UV-VIS calibration curves (linear).

2.2.5 TEM sample preparation and measurements

TEM samples of n^+-Si/SiO_2 were prepared with focused ion beam (FIB; SMI3050SE, SII Nanotechnology) gun of FE-SEM after sequential deposition of carbon and Au for sample protection. The sampling area for TEM was selected whose cross-sections to be perpendicular to the wafer. HR images were taken by HR-TEM (JEM-2100F, JEOL) operated at 200 kV. Electron energy loss

spectrum (EELS) was obtained by Cs-STEM (JEM-ARM200F, Cold FEG, JEOL).

2.2.6 Experimental setup for intermediate capture using TEMPO

2,2,6,6-Tetramethylpiperidin-1-yl)oxyl (TEMPO was used to capture the proposed neutral charge radical intermediate. TEMPO, however, is unstable in a strongly acidic solution (<pH 3) and undergoes disproportionation. Nafion membrane was enough to make the solution acidic, so H-type divided cell could not be employed. The electrolysis was performed for undivided cell but CE properly separated using double junction of Vycor tips. The schematic illustration is described in Fig. 2-4.

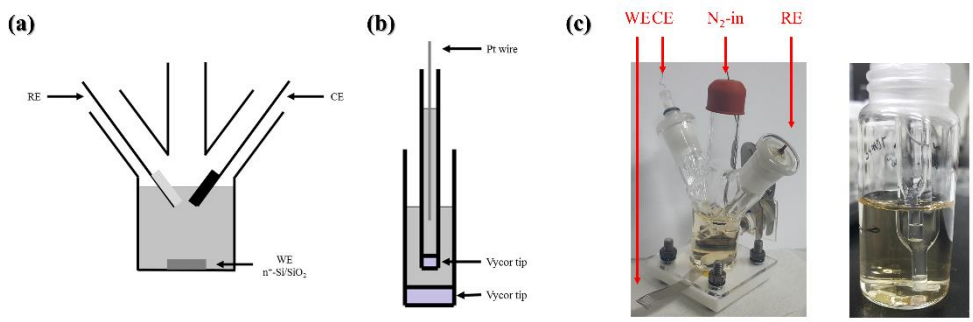

Fig. 2-4 Schematic illustration and photos of the experimental setup for intermediate capture using TEMPO. (a) Three electrodes in an undivided cell. (b) CE separated by the double junction of Vycor tips. (c) Photo of the undivided cell and double junction Vycor tips in a solution-filled vial.

2.2.7 Preparation of CVD SiO_2 (TEOS CVD and PECVD)

N-type, arsenic-doped, <100> oriented Si (n^+-Si) wafers of low resistivity (0.005 Ω cm) were obtained from STC (Japan). The wafers were all cleaned by standard SPM and SC-1,2 cleaning consecutively then stripping native oxide by diluted HF. The target 200 nm-thickness of oxides were prepared by chemical vapor deposition (CVD) to compare the defective thermal oxide. Tetraethylorthosilicate (TEOS) CVD oxide was prepared inside the CVD chamber (P-5000 II, AMK) with both 150 sccm of TEOS/He and O_2 under 9 Torr pressure with 350 W RF power. Plasma-enhanced CVD (PECVD) oxide was prepared at the CVD chamber (PlasmaPro System 100, Oxford Instrument) with 5% SiH_4/N_2 at 350 C.

2.3 Results and Discussion

2.3.1 Characterization of the electrochemical behavior of the defective 200 nm n^+−Si/SiO_2 dielectric electrode

Fig. 2−5 shows the representative electrochemical behavior of the defective 200 nm n^+−Si/SiO_2 electrode used in this work. As shown in Fig. 2−5a, cathodic current begins to flow at −1 V under acidic aqueous medium. Both the current density and the onset potential respond to proton concentration. However, the anodic current is negligible and is unchanged wherever potential scan begins (Fig. 2−6). Therefore, the defective 200 nm n^+−Si/SiO_2 electrode selectively flows cathodic current. Fig. 2−5b shows the voltammetry of dielectric electrode in the presence of redox couple which undergoes outer−sphere electron transfer in aqueous media. Without acid, an ignorable amount of cathodic current flows indicating that electron tunneling is negligible across the SiO_2 layer. This is analogous to the previously reported 6−nm−thick n^+−Si/SiO_2 EOS system [16]. Similar electrochemical behavior is also observed in organic aprotic solvents such as acetonitrile (MeCN) containing perchloric acid ($HClO_4$), tetrabutylammonium perchlorate (TBAP) electrolyte (Fig. 2−5c and 2−5d). Compared to the voltammetric response in aqueous solution, the current density decreases significantly while the onset

potential appears to be similar. A lower degree of dissociation of the acids in an aprotic solvent is responsible for lower current density [27]. The proton-driven cathodic current is affected by redox couple but the influence is insignificant [16].

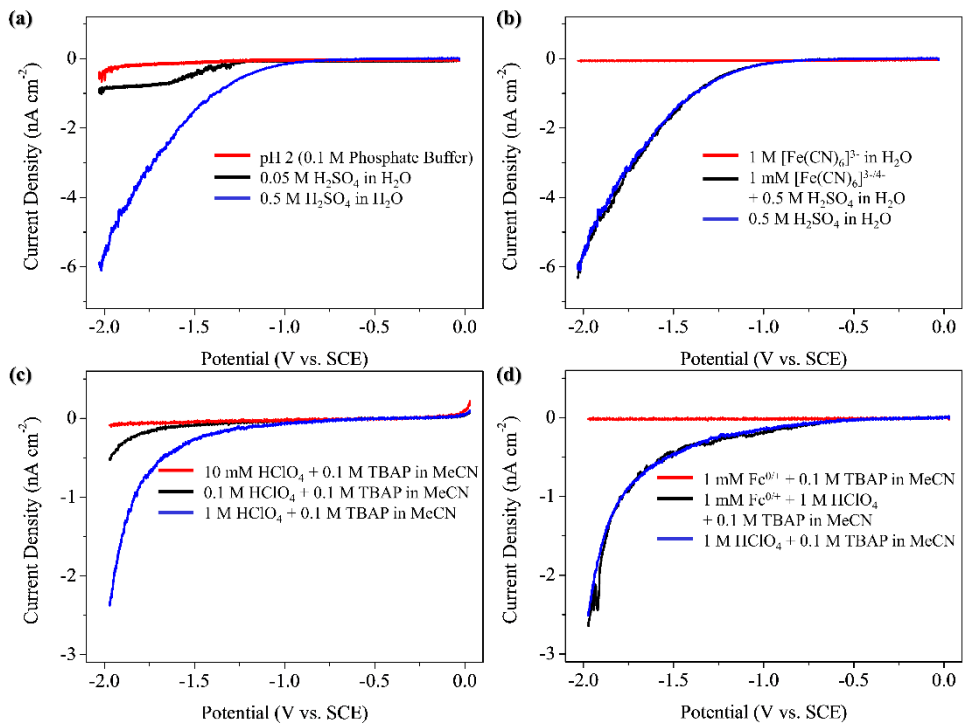

Fig. 2-5 Representative voltammetric response of the defective 200 nm n^+-Si/SiO_2 electrode measured in N_2 atmosphere. Linear sweep voltammograms in (a) various concentration of aqueous acid solution, (b) $Fe(CN)_6^{3-/4-}$ redox couple in acidic aqueous solution, (c) various concentration of acid in MeCN, and (d) $Fe^{0/+}$ redox couple in acidic MeCN.

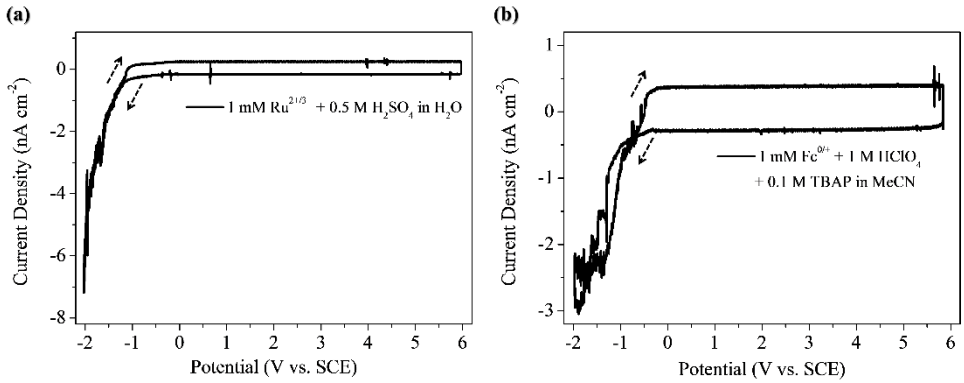

Fig. 2-6 Electrochemical behavior of the defective 200 nm n^+-Si/SiO_2 electrode. (a) Cyclic voltammogram of large potential range in 1 mM $[Ru(II)(NH_3)_6]^{4-}$ + 1 mM $[Ru(III)(NH_3)_6]^{3-}$ + 0.5 M H_2SO_4 in H_2O. (b) Cyclic voltammogram of large potential range in 1 mM Fc + 1 mM Fc^+ + 1 M $HClO_4$ + 0.1 M TBAP in MeCN.

While performing the electrolysis by defective 200 nm n^+-Si/SiO_2, faradaic current progressively increases as proceeds over 40 h, where the current density approaches near to the order of ~100 $\mu A \cdot cm^{-2}$ (Fig. 2-7). The accumulated charge passed corresponds to the order of 10 C, which produces a sufficient amount of change in both the reactant and the product for a particular electroorganic reaction. Such an increase of current density suggests that the SiO_2 film might be damaged to have physical or chemical defects as a consequence of prolonged cathodic bias. We examined the dielectric layers in the middle of electrolysis by HR-TEM (Fig. 2-8) and FE-SEM (Fig. 2-9). Collecting a number of images at random spots, we found no observable physical defects such as pinholes or cracks. To confirm this, Pd and Cr metals were electrodeposited on the

electrodes that had been through a long period of electrolysis and cyclic voltammetry was performed (Fig. 2-10). Any severe physical damage such as pinhole and crevice would lead to a short circuit between the electroplated metal film and underlying Si, at least enhanced electron tunneling. Metal films on the SiO_2 layer do not modify the voltammogram appreciably, supporting that negligible physical defects during a long period of cathodic bias. With regard to chemical defects, we investigated the SiO_2 film before and after electrolysis in various ways of surface analysis, i.e. Raman spectroscopy, electron energy loss spectroscopy (EELS), and X-ray photoelectron spectroscopy (XPS). All of these gave no significant difference (Fig. 2-11, Fig. 2-12, Fig. 2-13, and Fig. 2-14). The chemical defects caused by prolonged cathodic bias could be inconsiderable to be detected by such surface analysis techniques or reversibly healed as the SiO_2 films go through post-analysis after electrolysis. Most of the physical damages are not restored as reversibly as chemical defects.

Upon negative bias, protons are expected to migrate across the thermal SiO_2 at a slow rate, lowering the resistance of the dielectric layer [16,18]. This is a reversible process as protons are expelled when potential bias is reversed. Meanwhile, it is highly probable that chemical defects are gradually accumulated. Such defects include dangling bonds and atomic vacancy inside the SiO_2 layer, which is supposedly a quasi-reversible change in film properties. The onset

potential becomes more positive and the cathodic current more augmented for the linear sweep voltammogram of the electrode before and after 12 h of electrolysis (Fig. 2-15). The voltammetric behavior, not completely, is recovered after under the condition free of potential bias. Although surface analysis techniques provided no evidence of appreciable chemical or physical defects, voltammetry implies that the cathodic damage caused by long electrolysis exists and appears to be semi-permanent.

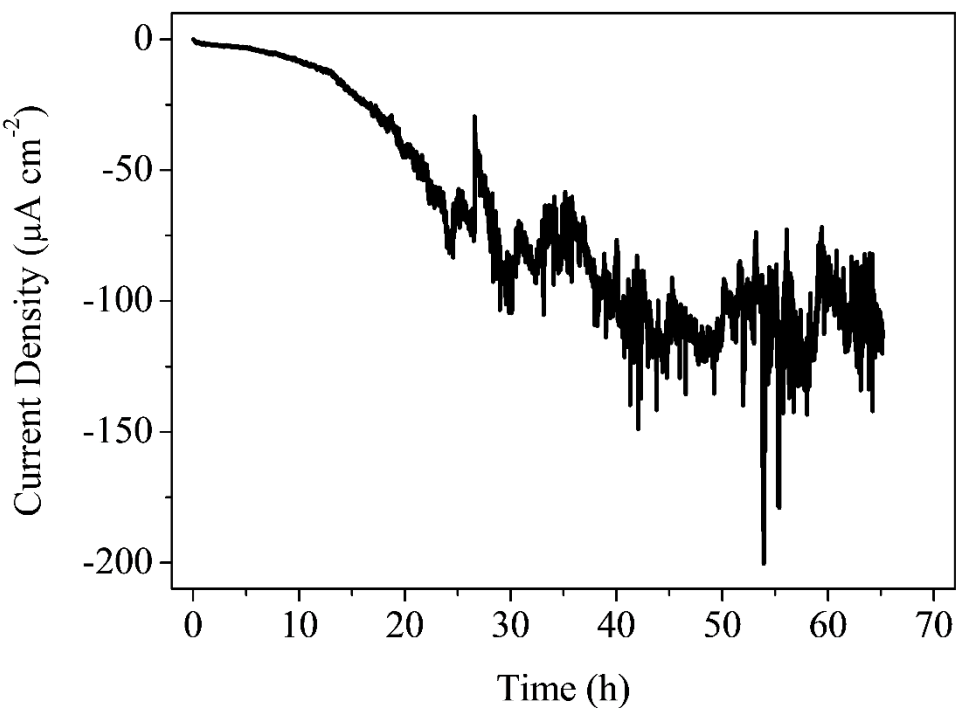

Fig. 2-7 The typical $i-t$ curve during electrolysis in 1 M $HClO_4$-MeCN solution at a constant voltage of − 1.67 V.

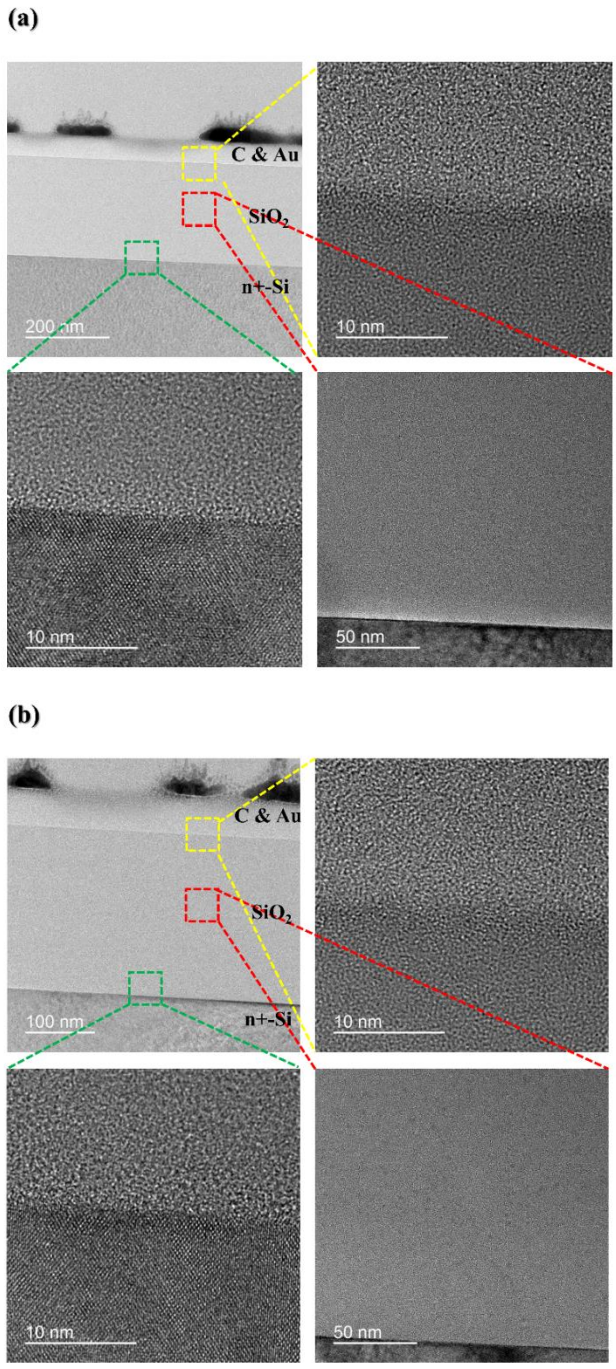

Fig. 2-8 HR-TEM of the defective 200 nm n^+-Si/SiO_2 electrode (a) before and (b) after electrolysis.

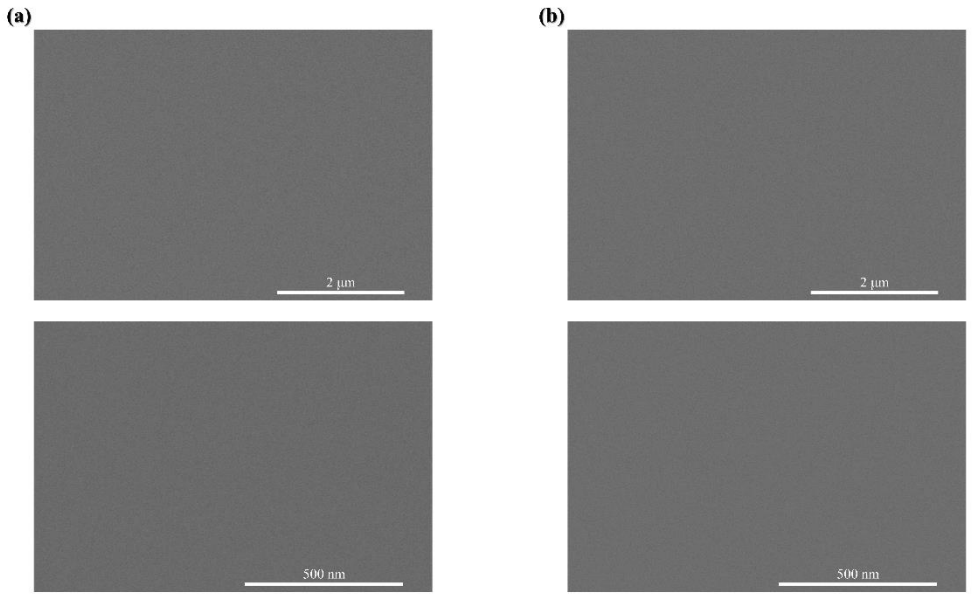

Fig. 2-9 FE-SEM of the defective 200 nm n^+-Si/SiO_2 electrode (a) before and (b) after electrolysis.

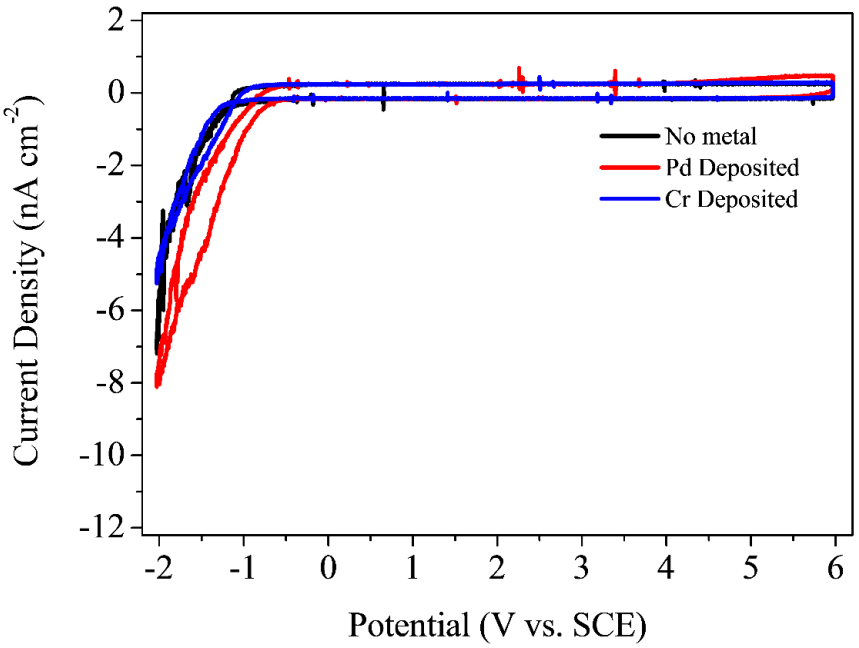

Fig. 2-10 Cyclic voltammograms of the defective 200 nm n^+-Si/SiO_2 electrode in large potential range with or without metal (Pd, Cr) deposition in 1 mM $Ru^{2+/3+}$ + 0.5 M H_2SO_4 aqueous solution. The metals were deposited on the electrodes that had been through 3 days of electrolysis. In case of Pd deposited dielectric electrode, slight oxidative current is observed at approximately + 4.5 V that is far more positive than the redox potential of $Ru^{2+/3+}$, approximately −0.2 V. Probably electron tunneling upon a high overpotential is responsible for it.

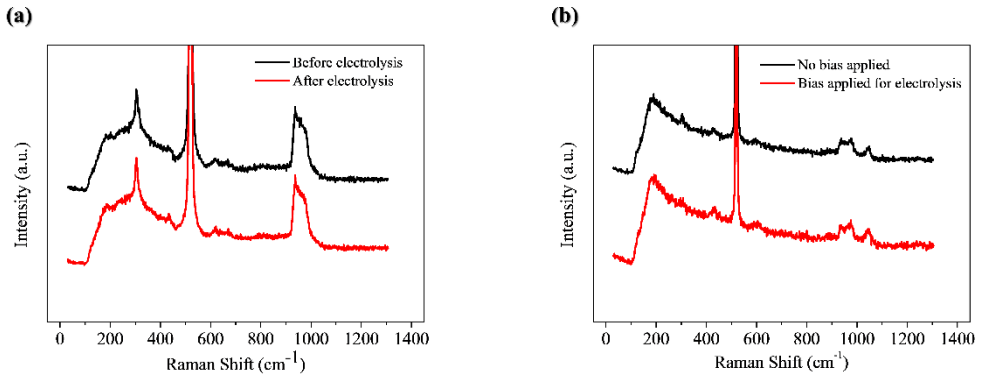

Fig. 2-11 (a) Raman spectra of n^+-Si/SiO_2 in ambient before and after electrolysis. (b) Electrochemical Raman spectra of n^+-Si/SiO_2 in 0.5 M H_2SO_4 aqueous solution at − 1.67 V to see the influence of electrochemical bias.

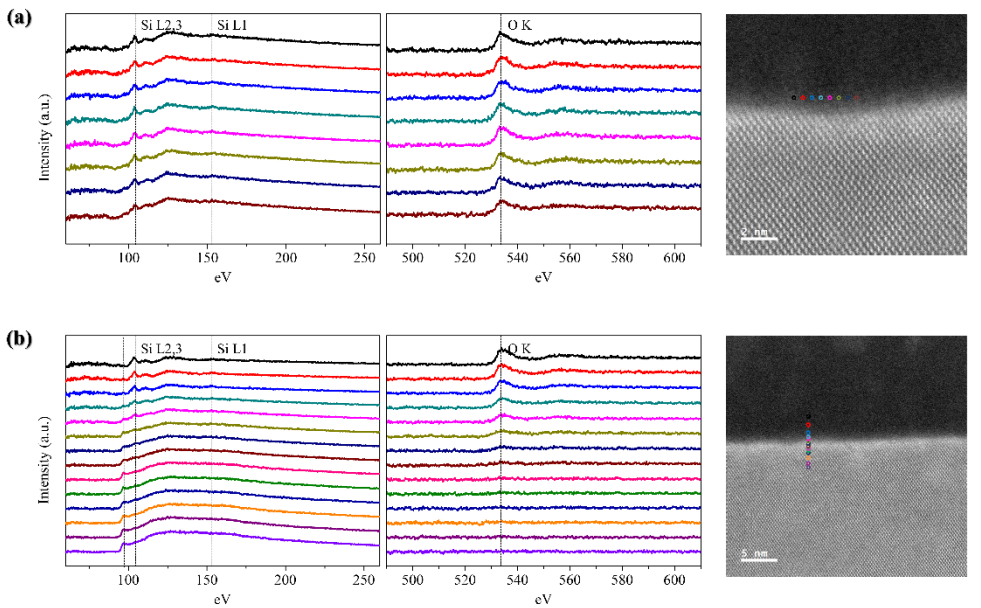

Fig. 2-12 (a) EELS of n^+-Si/SiO_2 before electrolysis in (a) horizontal and (b) vertical line profile.

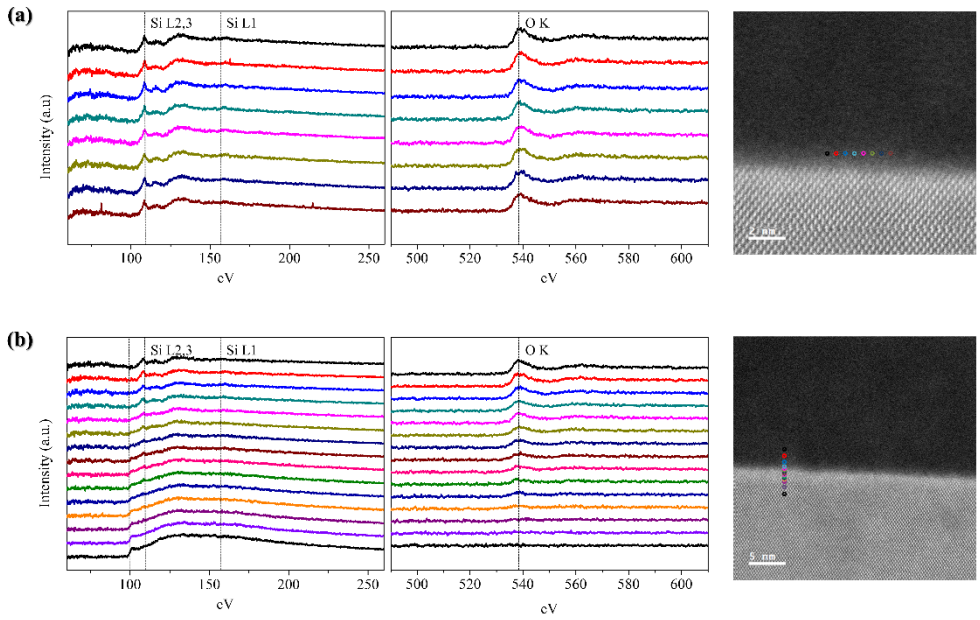

Fig. 2-13 (a) EELS of $n^{+}-Si/SiO_2$ after electrolysis in (a) horizontal and (b) vertical line profile.

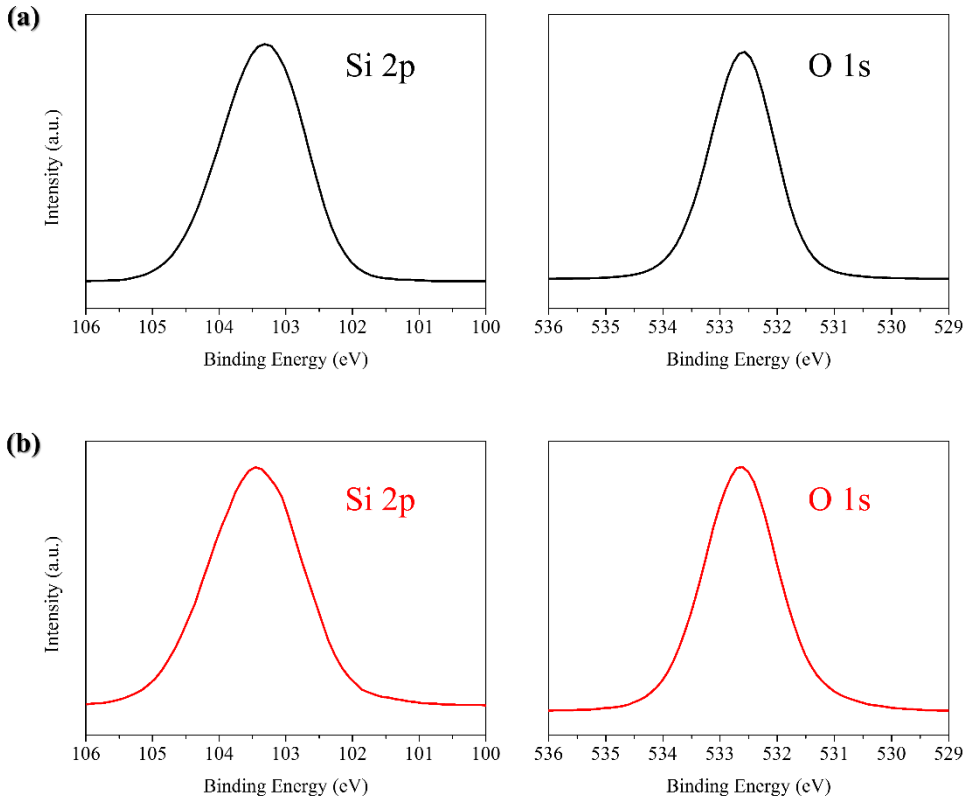

Fig. 2-14 XPS of n^+-Si/SiO_2 (a) before (black) and (b) after (red) electrolysis.

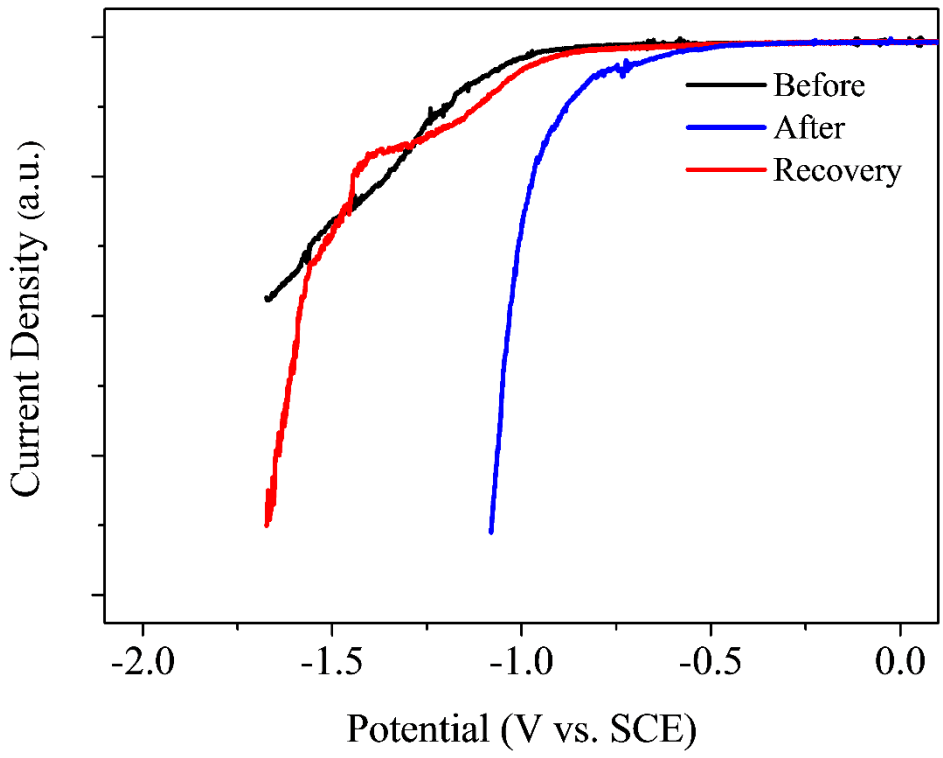

Fig. 2-15 Cyclic voltammograms of the defective 200 nm n^+-Si/SiO_2 electrode comparison upon long period of electrolysis. The working solution was 5 mM ANTH + 1 mM BP + 1 M $HClO_4$ in MeCN.

2.3.2 Cathodic electroorganic reaction of ANTH and its derivatives on defective 200 nm n^+−Si/SiO_2 dielectric electrode

Anthracene (ANTH, **1a**) is chosen as the reactant to investigate the cathodic electroorganic reaction on the defective thermal SiO_2. It is one of the smallest building block molecules to constitute PAHs and their chemical conversion and degradation are important in terms of their health risk in daily lives [28−32] Fig. 2−16 shows the presence of **1a** insignificantly modifies the voltammetric response of the defective thermal SiO_2. Comparing the onset potential in acidic organic solution, the dielectric electrode is far more positive than the reduction potential of **1a** measured by the cyclic voltammetry on the glassy carbon electrode (Fig. 2−16, $E_{c1,1/2}{}^{\circ}$ = −2.02 V. The full voltammogram is in Fig. 2−17). This implies the possibility of chemical reaction **1a** with the electrochemically generated species at the electrode can't be neglected. Moreover, this electrochemically generated species is thought to be a hydrogen atom.

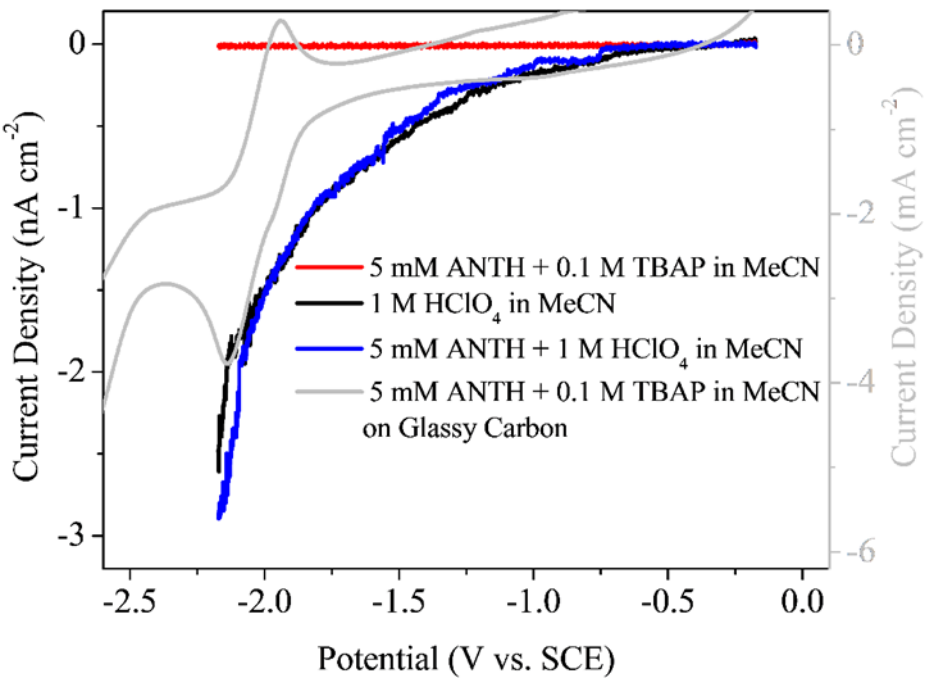

Fig. 2-16 Linear sweep voltammograms of **1a** on defective 200 nm n^+-Si/SiO_2 dielectric electrode in acidic MeCN and N_2 atmosphere. Cyclic voltammogram of **1a** on glassy carbon electrode is attached for comparison.

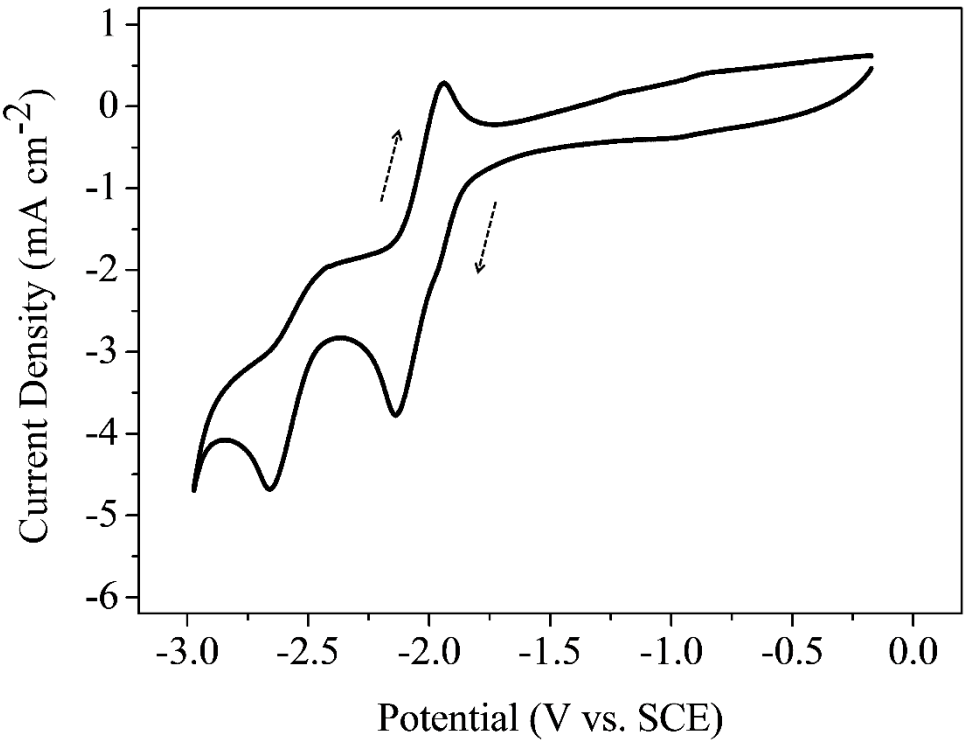

Fig. 2-17 Cyclic voltammogram of N_2-purged 5 mM ANTH (**1a**) + 0.1 M TBAP in MeCN on glassy carbon electrode.

The electrolysis of **1a** in acidic organic media and N_2 atmosphere performed in H-type divided cell with -1.67 V applied, which is less negative to its reduction potential, exploits interesting evidence about the actual phenomenon happening at the defective thermal SiO_2. It was found that the anthraquinone (AQ, **2a**) is produced as a result of cathodic electrolysis, confirmed by LC-MS and ^{1}H-NMR showed that (Fig. 2-18 and Fig. 2-19, respectively). In other words, **2a**, the "oxidized" form was produced upon cathodic" potential. Several control experiments approved that this is truly the

electrochemical reaction (details in section 2.3.4. Control experiments). This is a unique phenomenon hardly observed in conventional electrosynthesis.

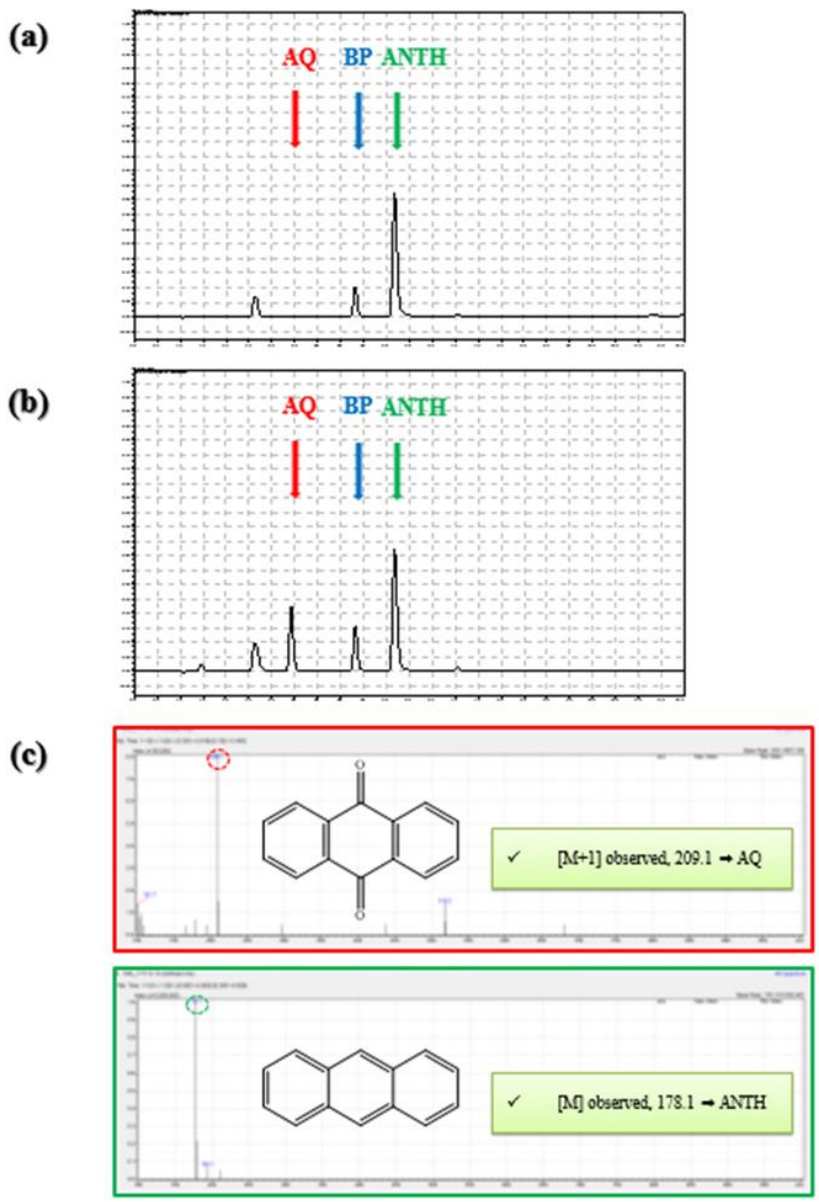

Fig. 2-18 Representative LC of (a) before and (b) after the reaction of ANTH on defective 200 nm n^+-Si/SiO_2 electrode. (c) MS of AQ (red) and ANTH (green).

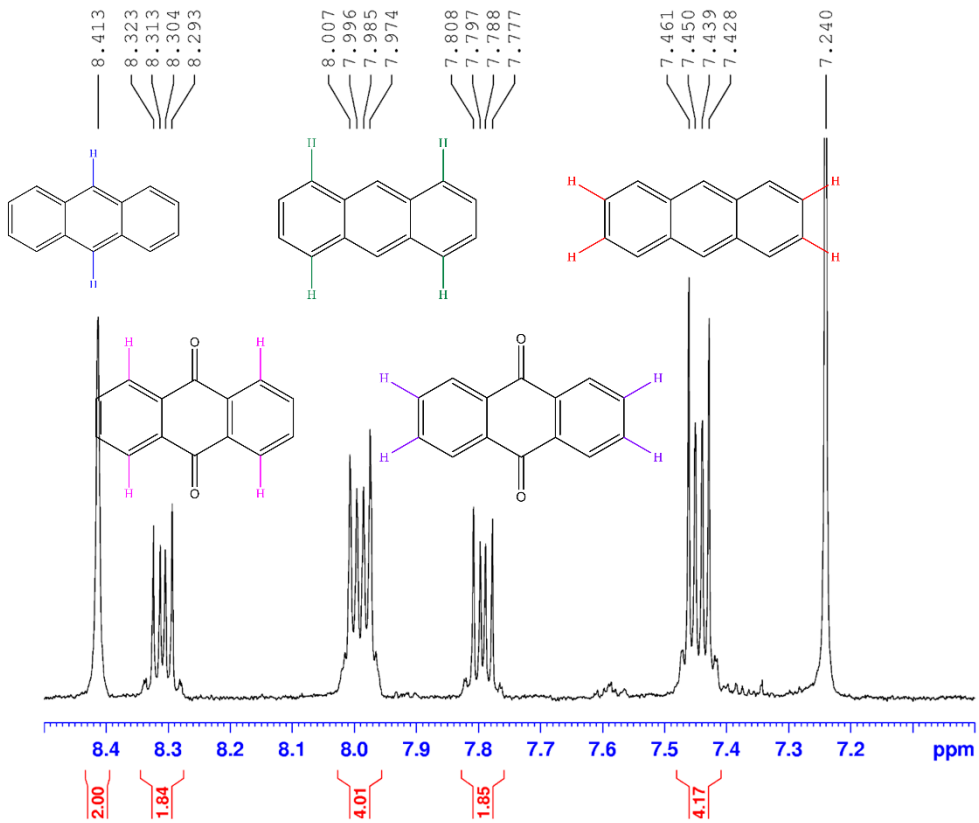

Fig. 2-19 ^{1}H-NMR of the product mixture obtained after the reaction of ANTH on defective 200 nm n^{+}-Si/SiO_2 electrode.

Table 2-2 summarizes the cathodic electroorganic reactions of **1a** on defective 200 nm n^+-Si/SiO_2 electrode by varying the concentration of acid and the reactant. Entry 1-3 exhibit the results for the concentration effect of proton in the starting solution. The results indicate that the extent of reaction was strongly dependent on the proton concentration as both the amounts of consumed (**1a**) and generated (**2a**) are clearly related to the proton concentration. This supports the idea of the hydrogen-related species produced from the electrode reacts with a reactant in the solution. Selectivity responds inversely to the concentration of proton, implying that the dilute concentration of proton promotes a more specific production of **2a**. Entry 1, 4, 5 suggest the effect of the **1a** concentration in the starting solution at the identical concentration of proton. The generated amount and selectivity are higher for a lower concentration of reactant **1a**. It is clear that a high concentration of reactant and proton does not contribute to the specific production of **2a**. As the penetration of **1a** through SiO_2 film is not possible, electrochemically generated species and **1a** should encounter at the interface between the dielectric film and the solution. The resulting heterogeneous process does not seem to be selective very much, probably being attributed to highly unstable hydrogen species electrochemically generated from the proton. Overall, these results imply such electrode is acting as a “chemical electrode”.

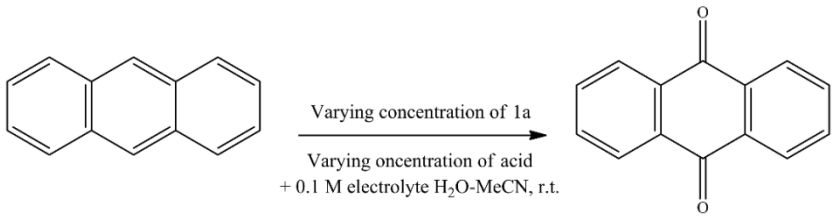

1a **2a**

Entry	*C* of 1a (mM)	*C* of Acid (M)	− (μmol)	− (%)	+ (μmol)	+ (%)	+/− (%)
1	5	1.00	18.55(±2.25)[a]	36.4(±4.4)[a]	4.56(±1.51)[a]	8.9(±3.0)[a]	25
2	5	0.10	5.12(±2.61)[a]	9.7(±5.0)[a]	2.41(±0.59)[a]	4.5(±1.1)[a]	47
3	5	0.01	1.60(±0.80)[a]	3.2(±1.6)[a]	0.89(±0.55)[a]	1.8(±1.1)[a]	56
4	2	1.00	3.15(±0.91)[a]	14.5(±4.2)[a]	2.56(±0.49)[a]	11.8(±2.3)[a]	81
5	0.7	1.00	2.08(±0.16)[a]	28.8(±4.3)[a]	2.13(±0.30)[a]	29.5(±10.6)[a]	103

* − (%): the consumed amount of reactant / the amount of starting material in percentage.
* + (%): the generated amount of product / the amount of starting material in percentage.
* +/− (%): the generated amount of product / the consumed amount of reactant in percentage.
* Abbreviation: *C* = concentration, − = consumed, + = generated, +/− = selectivity.
[a] Quantification done by LC−MS.

Table 2−2 The summary of **1a** electroorganic reaction on defective 200 nm n^+−Si/SiO_2 electrode by varying the concentrations of **1a** and acid. All the reactions are carried out at room temperature in N_2 atmosphere.

The idea of such “chemical electrode” can also be supported by the electrolysis performed by other oxides. The 200 nm thick n^+−Si/SiO_2 electrode can be alternatively fabricated tetraethylorthosilicate (TEOS) chemical vapor deposition (CVD) and chemical vapor deposition (PECVD) (Table 2−3). By and large, the oxides as made exhibit electrochemical behavior similar to the defective 200 nm n^+−Si/SiO_2 in this study in that current increasingly flows upon a constant negative bias. The limiting current of PECVD is in mA·cm^{-2} scale that is too high to be considered as an insulator (data not shown. See the accumulated charge in Table 2−3). PECVD gives oxide films that have more physical defects such as pinhole or cracks through which direct electron transfer occurs between n^+−Si and the electrolyte solution. Although TEOS CVD oxide allows low current, far less **1a** is consumed because of much less intrinsic chemical defects than the defective 200 nm n^+−Si/SiO_2 electrode. Therefore, the defective 200 nm n^+−Si/SiO_2 electrode was the most appropriate candidate for studying electroorganic reaction shown here among many oxide films we tested. Furthermore, the hydrogen species must be closely related to the intrinsic chemical defects of the oxide. This hydrogen species is thought to be the key to the action of “chemical electrode”.

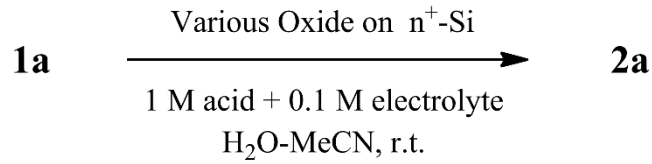

Entry	Oxide	Accumulated Charge (C)	− (%)	+ (%)	+/− (%)
1	Defective Thermal	46.43	36.35[a]	8.94[a]	29.46
2	TEOS CVD	52.33	9.24[a]	4.45[a]	48.22
3	PECVD	1121	5.51[a]	5.08[a]	92.19

* − (%): the consumed amount of reactant / the amount of starting material in percentage.
* + (%): the generated amount of product / the amount of starting material in percentage.
* +/− (%): the generated amount of product / the consumed amount of reactant in percentage.
[a] Quantification was done by LC−MS.

Table 2−3 The electroorganic reactions of ANTH to AQ on different oxides on n^+−Si electrode. The solution components are 1a (5 mM), 1 mM biphenyl (BP, internal standard), and 1 M $HClO_4$ in MeCN at room temperature in N_2 atmosphere.

Table 2-4, Fig. 2-20, and Fig. 2-21 represent the electroorganic reactions of several organic compounds on defective 200 nm n^+-Si/SiO_2 electrode. The chemical structures of the abbreviated compounds in Table 2-4 are organized in Fig. 2-20 for clear comprehension. It was found that the chemical derivatives of **1a** (**1b**, **1c**, and **1d**) were also "oxidized" as a result of "cathodic" electrolysis. The selective oxidation occurred at the preferred site of acene. The detailed explanation of the reason behind this is discussed in section 2.3.3. together with the proposed reaction mechanism. Other chemical structures among PAHs such as phenanthrene (Phen, **3a**) and pyrene (Py, **4a**) were also investigated. **3a** was found to be inert while **4a** was significantly consumed. No identifiable products were observed in the case of **4a**, probably by either decomposition or loss of product by work-up. The interesting feature of the reaction of PAHs is that the consumed amount upon electrolysis was strongly dependent on their electrochemical reduction potential (E, all measured from cyclic voltammetry on glassy carbon electrode, see section 2.3.5. Chemical and electrochemical analyses), as shown in Fig. 2-21. The consumed amount and reduction potential linearly correlate with each other except **1d**. This implies that the whole reaction is governed by the electrochemical process. On the other hand, normal reduction of organic reactant also occurs at a dielectric electrode upon cathodic bias as presented by the from nitrobenzene to aniline. Besides, many metals can be directly electrodeposited on

the dielectric electrode as reported in the previous reports [16,19].

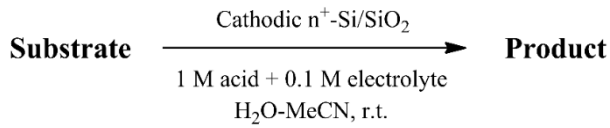

Entry	Substrate	Acid–Electrolyte	Applied Voltage (V)	E° (V)	– (%)	Product	+ (%)	+/– (%)
1	**1a**	$HClO_4$	−1.67	−2.02	36.4 (±4.4)[a]	**2a**	8.9 (±3.0)[a]	25
2	**1b**	$HClO_4$	−1.67	−2.20	6.7 (±0.8)[b]	**2b**	1.9 (±1.2)[b]	28
3	**1c**	$HClO_4$	−1.67	−2.17	11.9 (±1.0)[b]	**2c**	4.0 (±1.6)[b]	34
4	**1d**	$HClO_4$	−1.67	−1.96	11.1 (±2.1)[b]	**2a**	1.5 (±1.4)[b]	14
5	**3a**	TFA–$NaClO_4$	−2.17	−2.51	0.2[b]	–	–	–
6	**4a**	TFA–$NaClO_4$	−1.67	−2.14	11.2 (±2.5)[b]	–	–	–
7	$PhNO_2$	H_2SO_4	−1.53	–	30.8[b]	$PhNH_2$	–	–

* – (%): the consumed amount of reactant / the amount of starting material in percentage.
* + (%): the generated amount of product / the amount of starting material in percentage.
* +/– (%): the generated amount of product / the consumed amount of reactant in percentage.
* Abbreviation: C = concentration, – = consumed, + = generated, +/– = selectivity.
[a] Quantification done by LC–MS.
[b] Quantification done by UV–VIS.

Table 2–4 Various organic compounds which undergo electroorganic reactions on defective 200 nm n^+–Si/SiO_2 electrode. The starting solution was composed of 5 mM reactant, 1 mM biphenyl (BP, internal standard), and 1 M acid–0.1 M electrolyte in (v/v) H_2O–MeCN. All the reactions were carried out at room temperature in N_2 atmosphere. Only the identified products are stated.

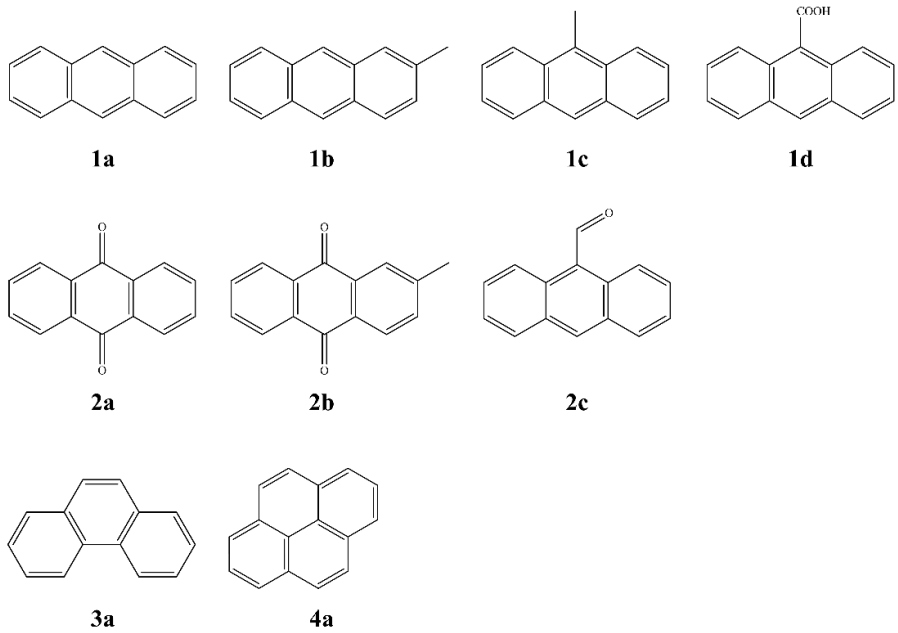

Fig. 2-20 Chemical structures abbreviated in Table 2-4.

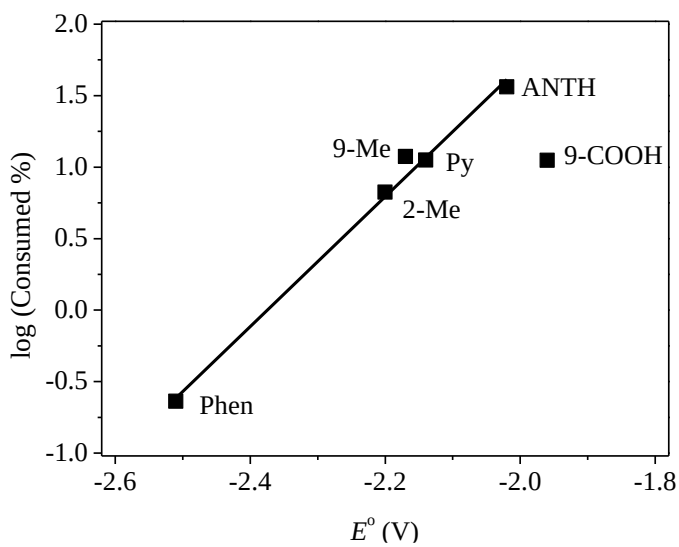

Fig. 2-21 The plot of log (Consumed %) against E° (V) of ANTH and its derivatives based on Table 2-4.

2.3.3 Proposal of the reaction mechanism of cathodic electroorganic on defective 200 nm n^+−Si/SiO_2 dielectric electrode

According to the observations of the cathodic electroorganic reaction in the EOS system of defective 200 nm n^+−Si/SiO_2 lead us to the reaction mechanism of the electroorganic reactions, which is illustrated in Fig. 2−22. The electrochemically generated species under cathodic potential is thought to be hydrogen atom as a few reports suggested and provided indirect evidence by Raman spectroscopy [16,33−34]. The reactions related to hydrogen at the thermal SiO_2 can be written as follows,

$$H^+ + e^- \rightleftharpoons H\cdot \qquad E_{H\cdot}^{o'} = -2.30\ V \qquad \text{(eq. 2−5)}$$

$$H\cdot + H\cdot \rightleftharpoons H_2 \qquad K = \frac{[H_2]}{[H\cdot]^2} \qquad \text{(eq. 2−6)}$$

$$2H^+ + 2e^- \rightleftharpoons H_2 \qquad E_{H_2}^{o'} = 0.000\ V \qquad \text{(eq. 2−7)}$$

$$\Delta G = -2FE = -2FE_{H_2}^{o'} + RTln\frac{[H^+]^2}{[H_2]} = -2FE_{H\cdot}^{o'} - RTlnK + RTln\frac{[H^+]^2}{[H_2]} \qquad \text{(eq. 2−8)}$$

A reaction of two hydrogen atoms to molecular hydrogen is a thermodynamically favored reaction, ΔG = −443.8 kJ/mol [26], which can be re−written in the form of the equilibrium constant, K,

and standard reduction potentials, $E^{o'}_{H\cdot}$ and $E^{o'}_{H_2}$. The homolytic bond dissociation energy (BDE) of C–H in 9–, 10–site of **1a** is 428 kJ/mol (the value includes the consideration of zero–point energy) [35], which is comparable to it. Thus, the intermolecular reaction between organic molecules and reactive hydrogen species may occur via hydrogen atom abstraction (HAA), which would be slow due to insufficient thermodynamic energy gain. This may attribute to the main reason for the high site selectivity to 9–site and 10–site C–H of **1a**. This resembles the proton–coupled electron transfer (PCET) in organic synthesis or oxidative HAA [36–38]. In addition, subsequent addition of H_2O to the neutral radical intermediate could thermodynamically promote HAA. Finally, the electroorganic reaction ends up to **2a** via auto–oxidation. The auto–oxidation of 9,10–anthracenediol to **2a** is very common in the anthraquinone process [39]. Nevertheless, both ^{1}H–NMR and the m/z peak from its LC–MS were the same, indicating auto–oxidation (Fig. 2–23 and 2–24).

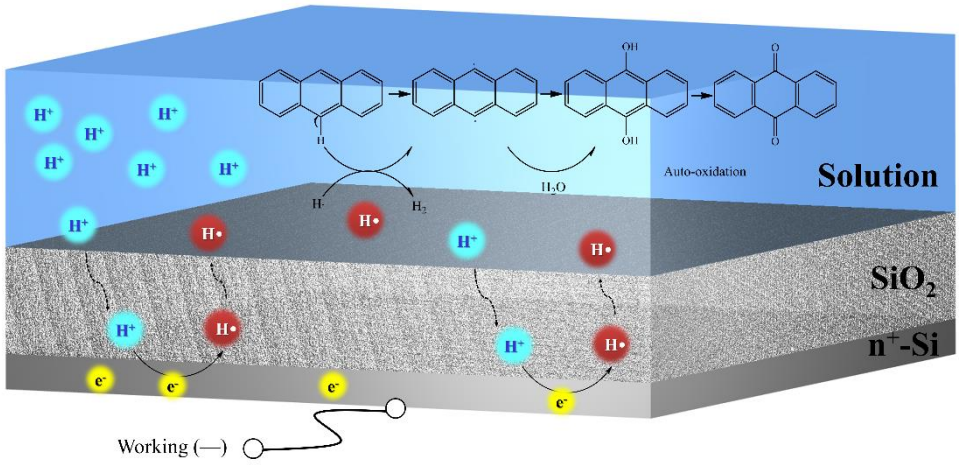

Fig. 2-22 Schematic view of the proposed mechanism of the ANTH (**1a**) cathodic electroorganic reaction on defective 200 nm n^+-Si/SiO_2 electrode.

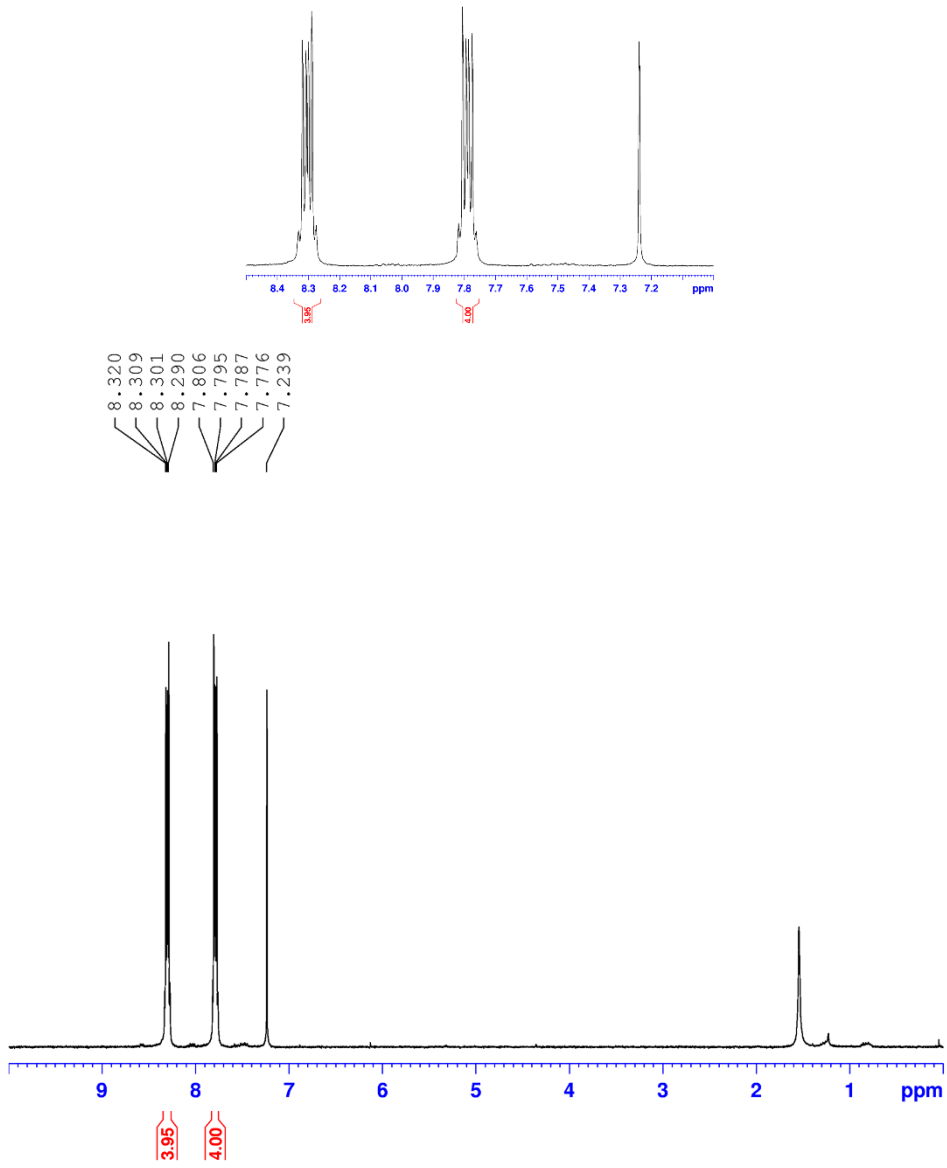

Fig. 2-23 ^{1}H-NMR of 9,10-anthracenediol in $CDCl_3$. Note that the spectrum is identical to AQ (**2a**). For comparison, see section 3.3.5.

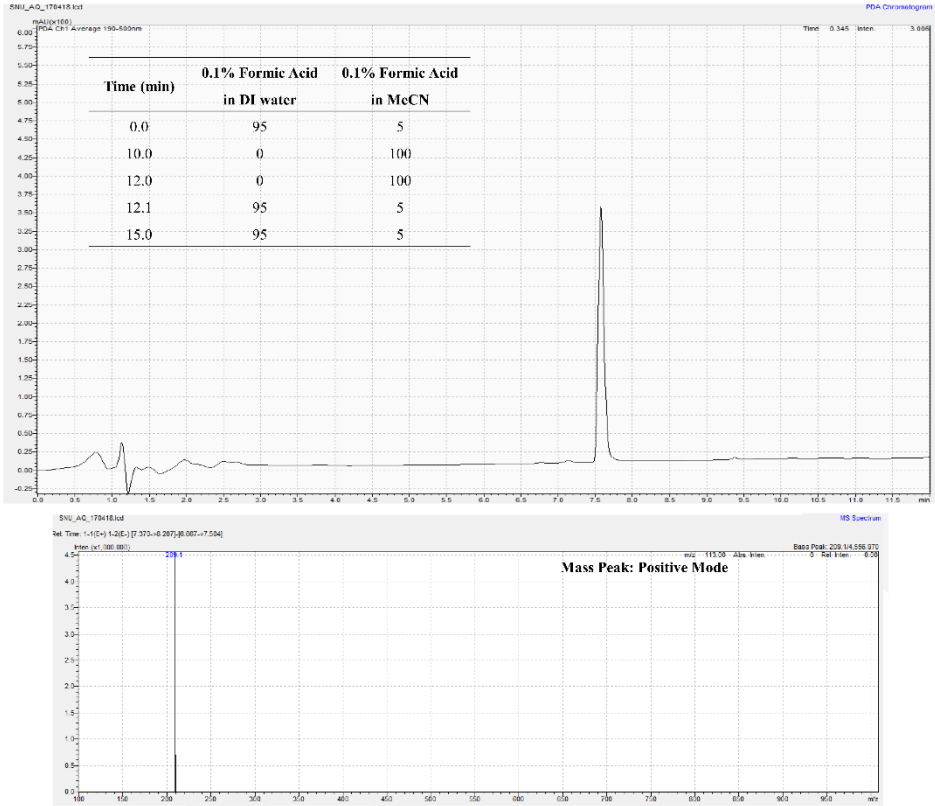

Fig. 2-24 LC-MS of 9,10-anthracenediol. The eluent condition is described in the inset. Note that both LC and m/z is identical to AQ (**2a**). For comparison, see section 3.3.5.

This proposed mechanism fits the result in Table 2-4 and Fig. 2-21. All the anthracene derivatives are oxidized upon a cathodic reaction on defective n^+-Si/SiO_2 electrode. As negative bias applied, the HAA by electrochemically generated hydrogen species may take place at the most reactive site of the reactant. In the case of **1a**, it is transformed to **2a** via preferential reactivity toward the C-H bond in the central ring of acene rather than less reactive peripheral acene [32]. For **1b**, similar to **1a**, the more reactive sites are 9- and 10-

sites. **1c**, on the other hand, the 9-substituted methyl (benzylic acene) is more reactive than the 10- site and peripheral acene, thereby HAA occurs selectively at 9-substituted methyl. The reaction of **1d** is interesting in that carboxylic group at 9- site is eliminated to yield **2a**. According to the voltammogram of **1d** (Fig. 2-25), the reactive site of **1d** is thought to be 9-COOH, where HAA takes place followed by decarboxylation. The intermediate by decarboxylation may be similar to **1a**, again undergoes the reaction to **2a**. For other PAHs of **3a** and **4a**, the consumption upon reaction is confirmed but no products are identified, suggested to be degraded upon exposure to electrochemically generated hydrogen species or product loss by work-up. Contrary to the earlier examples, nitrobenzene undergoes reduction "normally" in the same system, unlike anthracene derivatives as shown in Table 2-4. The C-H bond in nitrobenzene is a phenyl-H which is an unfavorable site to undergo HAA. Thus, hydrogenation occurs at the nitro group to yield aniline, the normal reduction product upon cathodic electroorganic reaction.

As mentioned earlier, the interesting feature of the reaction of PAHs is that the amount of the reactant consumed is linearly dependent to the measured reduction potential (E°) rather than BDE except for **1d** (Fig. 2-21) since the proposed reaction of **1d** is distinguished to the other derivatives. The reason for this is still unclear but some ideas can be given. First, the manifest dependence on E° indicates that the electrochemical electron transfer process is

involved in the entire reaction as a crucial step, which can determine the apparent reaction rate.

Secondly, bond dissociation free energy (BDFE, ΔG_{BDFE}) may be related. According to the reaction mechanism, BDFE may be an important parameter to be considered. Note that this term differs from the BDE which is the enthalpy of PAHs. As the free energies are state functions, the thermochemical cycle can be written as follows to describe the BDFE for the reactant of ϕ−H, the C−H bond of 9 site in case of ANTH,

$\phi - \mathrm{H} + e^- \rightleftharpoons \phi - \mathrm{H}^{-\cdot}$	E^o	(eq. 2−9)
$\phi - \mathrm{H}^{-\cdot} \rightleftharpoons \phi\cdot + \mathrm{H}^-$	$\Delta G_{\phi - H^{-\cdot}/\phi\cdot}$	(eq. 2−10)
$\mathrm{H}\cdot + e^- \rightleftharpoons \mathrm{H}^-$	$E^o_{\mathrm{H}\cdot/\mathrm{H}^-}$	(eq. 2−11)
$\phi - \mathrm{H} \rightleftharpoons \phi\cdot + \mathrm{H}\cdot$	ΔG_{BDFE}	(eq. 2−12)

$$\Delta G_{BDFE} = -FE^o + \Delta G_{\phi - H^{-\cdot}/\phi\cdot} + FE^o_{\mathrm{H}\cdot/\mathrm{H}^-} \quad \text{(eq. 2−13)}$$

where E^o is the standard reduction potential of ϕ−H and $E^o_{\mathrm{H}\cdot/\mathrm{H}^-}$ is the standard reduction potential of H·. A few values of $E^o_{\mathrm{H}\cdot/\mathrm{H}^-}$ were reported in the literature as a function of solvents [40].

The BDFE including the terms such as solvation energy and entropy can be considered as arbitrary constant C,

$$\Delta G_{BDFE} = -FE^o + \Delta G_{\phi - H^{-\cdot}/\phi\cdot} + C \quad \text{(eq. 2−14)}$$

As shown in Fig. 2−21, the amounts of the PAHs electrolyzed in this study linearly correlate with E^o as long as the reaction are in the same class. Therefore, E^o is the dominant factor to determine ΔG_{BDFE} although we have no information about the values of

$\Delta G_{\phi-H^{-\cdot}/\phi^{\cdot\cdot}}$.

After all, the consumed amount in the fixed period of electrolysis was reproducible so it must be linearly proportional to the average reaction rate constant. This tells that the logarithmic consumed amount should be related to ΔG_{BDFE}.

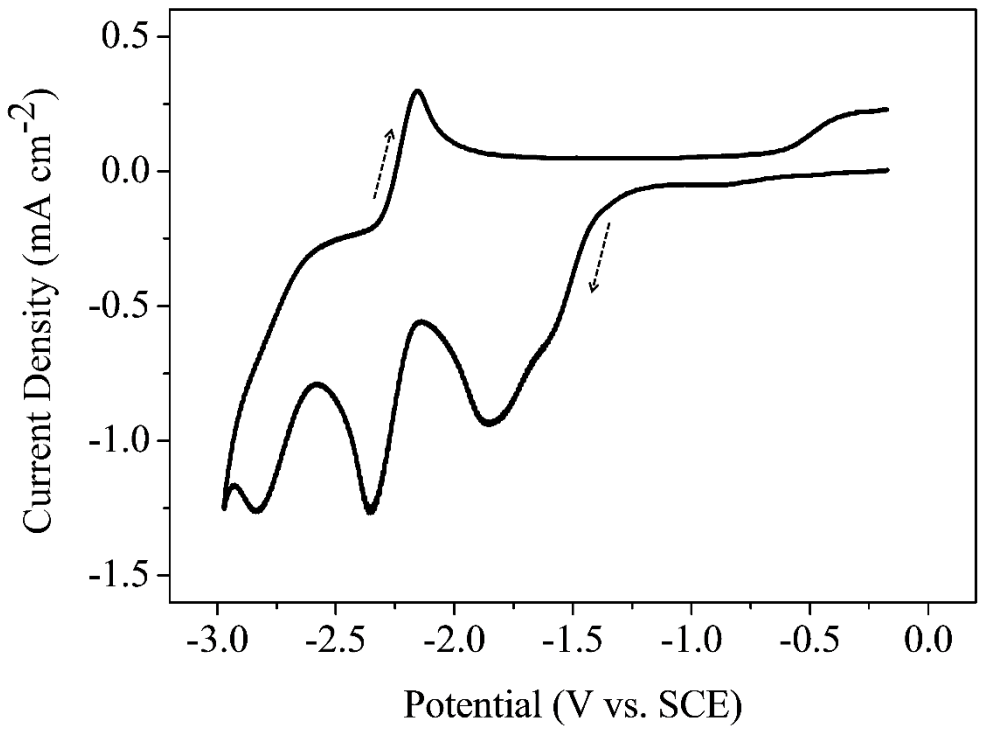

Fig. 2-25 Cyclic voltammogram of N_2-purged 5 mM 9-COOH-ANTH (**1d**) + 0.1 M TBAP in MeCN on glassy carbon electrode. The broad irreversible reduction must be related to the 9-COOH site since this is only observed among other anthracene derivatives.

The results of cathodic electroorganic reaction on the dielectric electrode suggest two important outcomes. First, this system may serve as a hydrogen atom donating platform directly from the solid phase to the solution without hydrogen atom transfer (HAT) catalysts. Second, the oxidation reaction by a hydrogen atom in such system. This is the first time to be reported in a mild condition since it was reported in a few cases of a hydrogen atom generated by harsh gamma-ray radiolysis [41,42].

More experimental evidences are needed to support such reaction mechanism. 2,2,6,6-Tetramethylpiperidin-1-yl)oxyl (TEMPO), a renowned radical capture agent [43,44], was used to capture the proposed charge neutral radical intermediate (Fig. 2-26). The captured intermediate was identified by LC-MS, observed [M+H] as m/z = 489.5 where M = ANTH - 2 H + 2 TEMPO (Fig. 2-27). It was too small amount to characterize with NMR because the reaction was carried out in 1 mM acid of organic media. It is well-known that TEMPO is unstable in a strongly acidic solution (<pH 3) and disproportionates, so the acidity of the reaction media was lowered in the reaction system. Consequently, as shown in Table 2-2, the reaction of **1a** on dielectric electrode was inefficient as being less acidic, lowering the chance to capture the target intermediate.

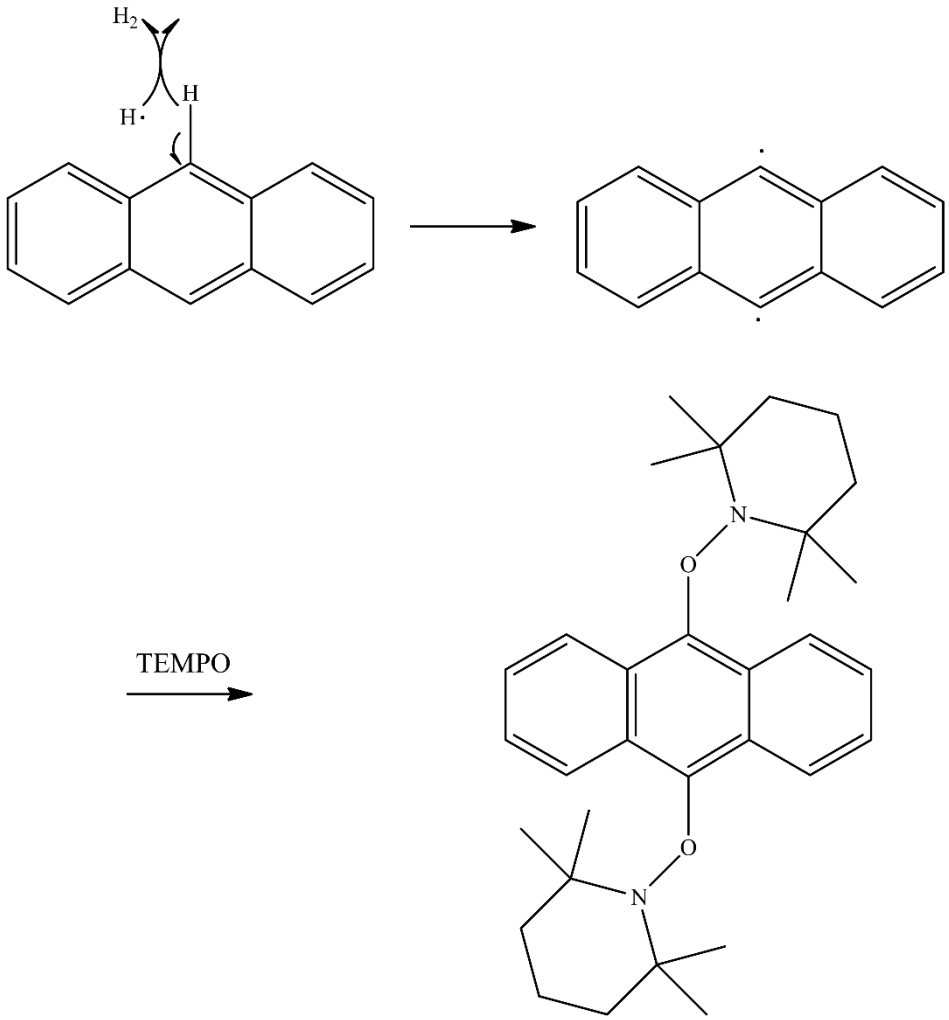

Fig. 2-26 Schematic illustration of the intermediate capture strategy using TEMPO for the proposed mechanism.

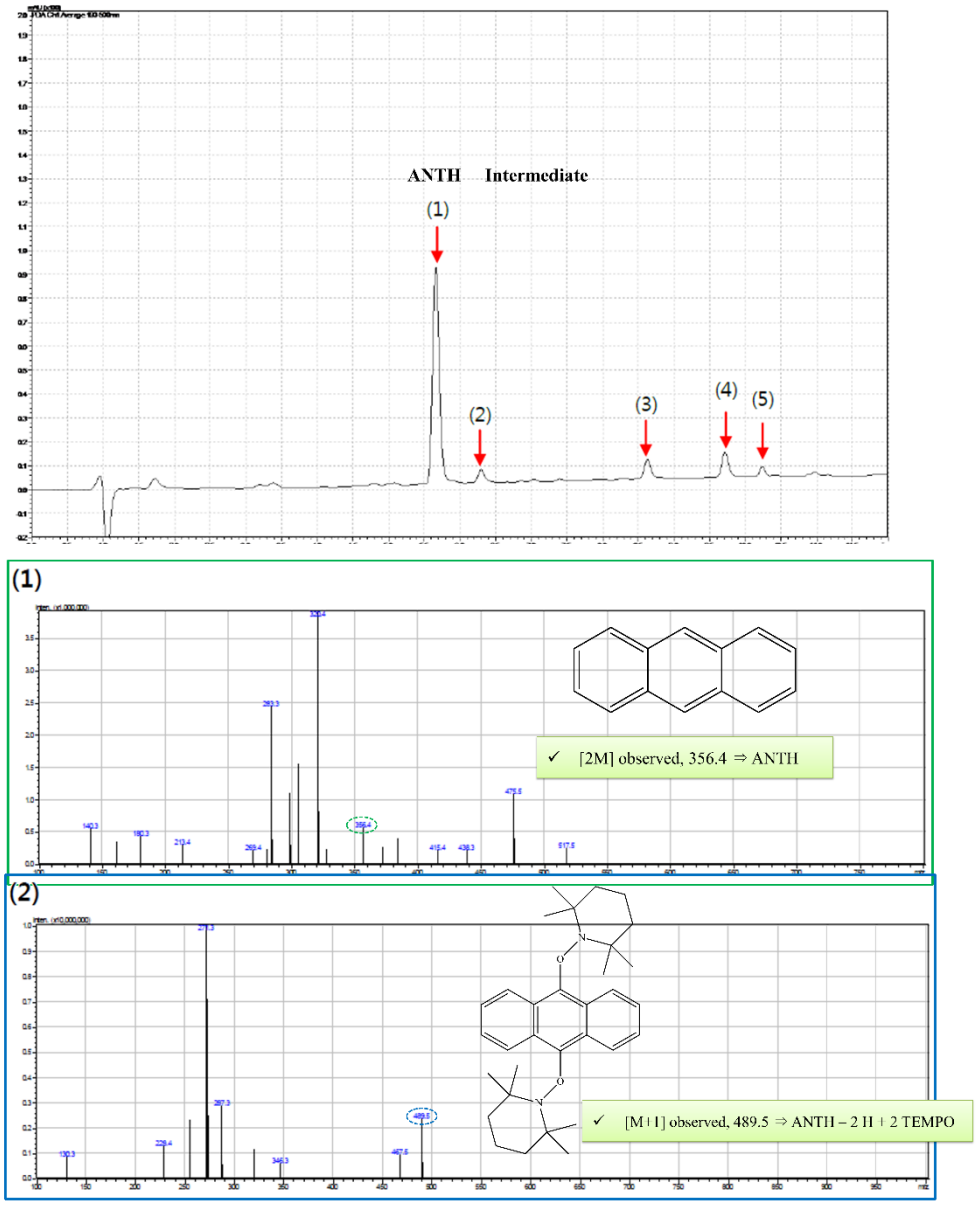

Fig. 2-27 LC-MS of the proposed intermediate captured by TEMPO. The large version is attached on section 3.3.5.

The role of H_2O in such cathodic electroorganic reaction in the EOS system is investigated (Table 2-5). Since the added acids contain moisture by itself, it was pointless to dry the solution. When H_2O is added to be 4% (v/v), the reaction remarkably occurred but the high content of H_2O, e.g. 10% of H_2O content or no H_2O inhibits the reaction. There is an optimal H_2O content for such reaction. Thus, it is clear that the electroorganic reaction of **1a** at the defective n^+-Si/SiO_2 electrode definitely involves H_2O in an appropriate amount. When $H_2{}^{18}O$ is added instead of H_2O, the reaction is significantly inhibited. Furthermore, LC-MS analysis of the reaction mixture exhibited the ratio in percent of the observed m/z peaks, the [M+H], for the product **2a** was ($C_{14}H_9{}^{16}O_2$, 209) : ($C_{14}H_9{}^{16}O^{18}O$, 211) : ($C_{14}H_9{}^{18}O_2$, 213) = 62.9 : 26.2 : 6.6. The produced **2a** contains low amount of ^{18}O, implying that most portion of the oxygen comes from H_2O rather than the additive $H_2{}^{18}O$. Thus, it can be inferred that the suggested neutral radical intermediate preferentially reacts with H_2O than $H_2{}^{18}O$. According to such observation, homolytic bond dissociation energies (BDE) of the additives must be responsible for it. The difference in reaction of ^{18}O and ^{16}O can be extremely large in the oxygen evolution at metal-complex [45]. It is well-known that the bond strength is generally stronger for heavy atoms, thereby ^{18}O-H is stronger than ^{16}O-H. Although the exact BDE is not known, the difference is not large enough to fully explain the specific reaction of H_2O. There must be many other factors of kinetic barrier to

dissociate O–H bonds, such as molecular orientation, thermodynamic stability, and free energy change of both the intermediate and the additives. Consequently, the radical intermediate should respond distinctively according to the suggested mechanism. In addition, the solubility of **1a** is sensitive to the fraction of the additives in acetonitrile. Although more additive as oxygen sources would help the overall reaction, too much of it cause solubility problem, i.e. **1a** starts to precipitate in 10% water.

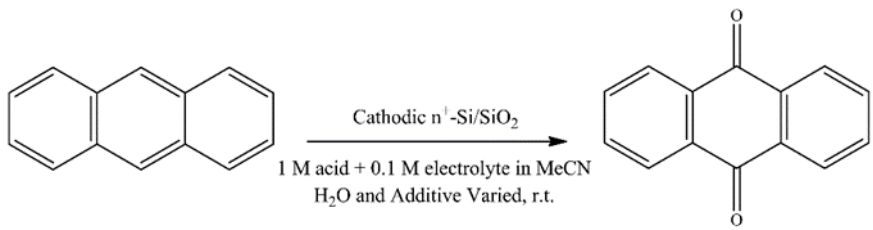

1a **2a**

Entry	Acid–electrolyte	Additive	Additive in MeCN (v/v 4%)	– (%)	+ (%)
1	TFA–$NaClO_4$	–	0	1.7[a]	2.0[a]
2	TFA–$NaClO_4$	H_2O	4	29.2[a]	14.7[a]
3	$HClO_4$	H_2O	4	36.4[a]	8.9[a]
4	$HClO_4$	H_2O	10	2.6[a]	2.5[a]
5	TFA–$NaClO_4$	$H_2{}^{18}O$	4	1.0[a]	0.4[a]

* – (%): the consumed amount of reactant / the amount of starting material in percentage.
* + (%): the generated amount of product / the amount of starting material in percentage.
[a] Quantification was done by LC–MS.

Table 2–5 The investigation of additive effect on cathodic electroorganic reaction of **1a** on defective 200 nm n^+–Si/SiO_2 electrode by changing the additive and its content. All the reactions were carried out in 1 M acid–electrolyte solution at room temperature in N_2 atmosphere.

2.3.4 Control experiments to confirm the cathodic electroorganic reaction of ANTH and its derivatives on defective 200 nm n^+-Si/SiO_2 dielectric electrode

Two probable mechanisms of ANTH reaction at conductor electrode other than the defective 200 nm n^+-Si/SiO_2 is illustrated in (Fig. 2-28). Superoxide could attack ANTH to produce AQ in the presence of oxygen. Since the electrolysis is conducted at defective 200 nm n^+-Si/SiO_2 dielectric electrode continuously supplying N_2 to purge out oxygen from the solution, we could rule out the superoxide mechanism. Even in the absence of oxygen, we can imagine radical anion as a result of electrochemical reduction of ANTH. If no AQ is produced by electrolysis at the conductor electrode in N_2 atmosphere, the second mechanism should not be responsible for AQ production at defective 200 nm n^+-Si/SiO_2 dielectric electrode.

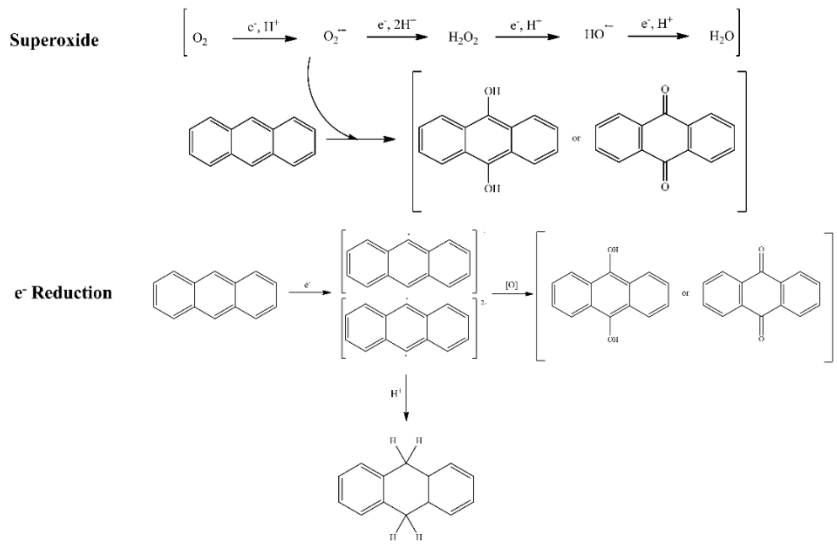

Fig. 2-28 Schematic illustration of two probable mechanisms of ANTH reaction at conductor electrode other than the defective 200 nm n^+−Si/SiO_2.

Electrolysis of ANTH in 1 M HClO4−MeCN at carbon rod as a working electrode in the different atmosphere (Fig. 2−29. When the cathodic bias of −1.17 V was applied to the solution of ANTH in 1 M HClO4−MeCN in the air for electrolysis of 12 h, ANTH was significantly consumed and AQ was generated (Fig. 2−29a). The potential bias applied is much less than that of ANTH, $E_{c1,\ 1/2}{}^{o}$ = −2.02 V, but negative enough to generate superoxide [46,47] which could provoke an unwanted radical reaction which is similar to ozonation [48]. Changing to N_2 atmosphere to purge dissolved oxygen in the solution, we could exclude oxygen effect, probably caused by superoxide, as shown in Fig. 2−29b.

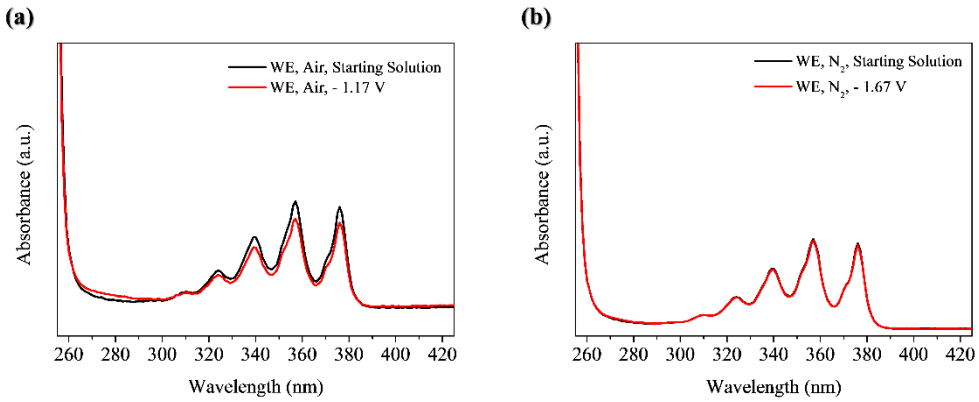

Fig. 2-29 Electrolysis of ANTH in 1 M $HClO_4$-MeCN at carbon rod as working electrode in (a) air and (b) N_2 atmosphere for 12 h. The applied voltages were − 1.17 V and − 1.67 V respectively.

Fig. 2-30 shows the UV-VIS spectra of the electrolysis products of ANTH in 1 M $HClO_4$-MeCN with various conventional working electrodes (conductors) in N_2 atmosphere for 12 h. The applied voltages are -1.67 V and -2.17 V, which are lower and higher than the 1st reduction potential of ANTH ($E_{c1,\ 1/2}^{o}$ = -2.02 V), respectively. In all cases, ANTH was not consumed, indicating that electrochemical conversion of ANTH to AQ uniquely occurs at defective 200 nm n^+-Si/SiO_2 dielectric electrode without dissolved oxygen. Note that the ANTH was not electrochemically consumed at -2.17 V applied, probably due to vigorous hydrogen evolution in highly acidic solution.

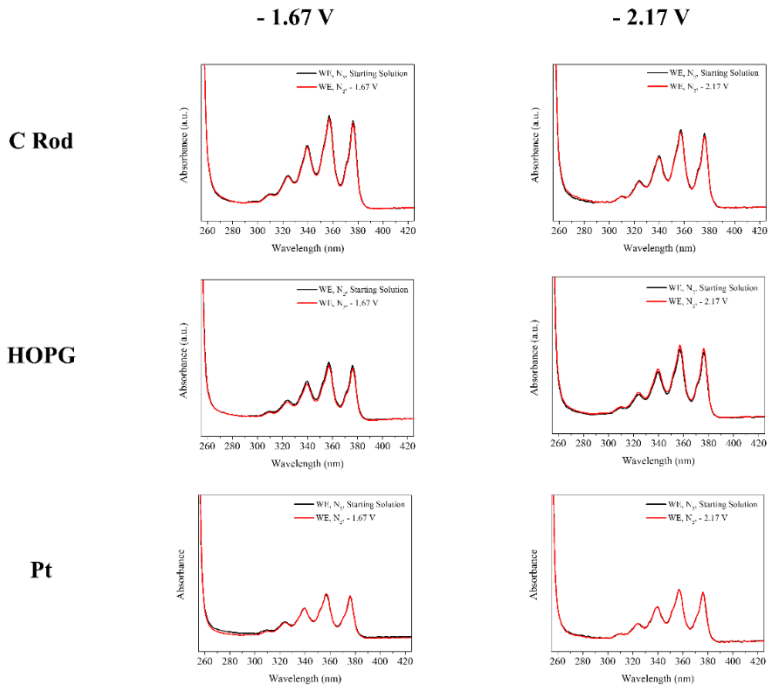

Fig. 2-30 UV-VIS spectra of the electrolysis products of ANTH in 1 M $HClO_4$-MeCN with various conventional working electrodes (conductors) in N_2 atmosphere for 12 h. The applied voltages are -1.67 V and -2.17 V, which are lower and higher than the 1st reduction potential of ANTH ($E_{c1,\ 1/2}^{o}$ = -2.02 V), respectively.

The longer period of 64 h electrolysis was performed and shown in Fig. 2-31. Electrolysis was performed of ANTH in 1 M $HClO_4$-MeCN with a bare n^+-Si (native oxide etched completely by dipping in HF for 1 h prior to electrolysis) as working electrode in N_2 atmosphere for 64 h (nearly 3 days). The change in the quantity of ANTH was checked by UV-VIS spectra. ANTH does not react in such electrochemical condition.

Since it is well-known that organics penetrates Nafion®, the extent of crossover must be examined. According to the UV-VIS spectra (Fig. 2-32), the crossed amount of ANTH from WE to CE was estimated to be 0.6%. This is a negligible amount for the calculation of ANTH consumption. Note that the crossover was minimized in our

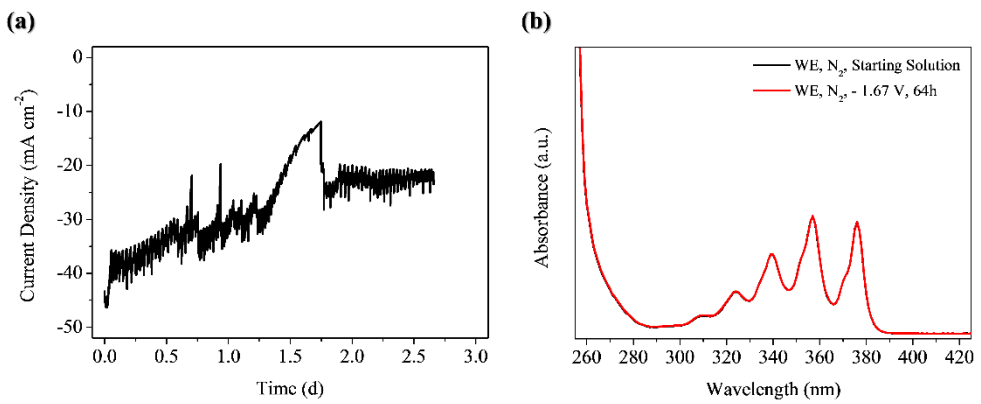

Fig. 2-31 Electrolysis of ANTH in 1 M $HClO_4$-MeCN with a bare n^+-Si (native oxide etched completely) as working electrode in N_2 atmosphere for 64 h (nearly 3 days) with - 1.67 V bias. (a) *i*-*t* curve and (b) UV-VIS spectra. The change of the quantity of ANTH was checked by UV-VIS spectra.

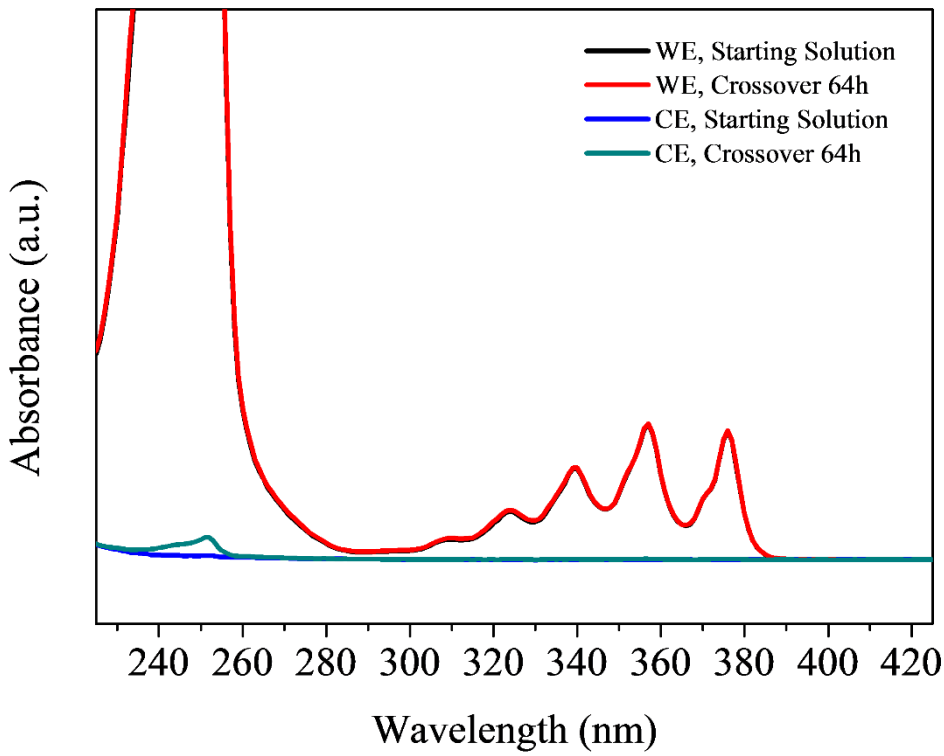

Fig. 2-32 Crossover check of ANTH in H-type divided cell with Nafion® membrane for 64 h.

system by shortening the inner diameter of the O-rings for Nafion®, described in section 1.1. If the O-rings were larger, the cross-section of Nafion® should be large enough thereby cannot neglect the crossover (data not shown).

In addition, it is well-known that ANTH and its derivatives undergo photooxidation to AQ [49]. We must check the extent of photooxidation (Fig. 2-33). First of all, ANTH is stable in dark (brown vial). UV-VIS measurements tell that ANTH oxidation is negligible at least 5 days in stray-light. Because the electrolysis in the H-type divided cell is inconvenient for the dark experiment, the

electrolysis period was limited to 3−5 days in this study. Note that periodic on/off of the UV−VIS spectrometer can cause the baseline variation, consequently contributing to the noise of absorbance at 357 nm (Fig. 2−33a). The photooxidation readily occurs when the lamps are irradiated to the solution (data not shown). In addition, photooxidation of the ANTH derivatives (Table 2−4) should be AQ irrespective of their functional group at 9, 10− substituent [49]. Therefore, the cathodic electroorganic reaction is not the result of photooxidation.

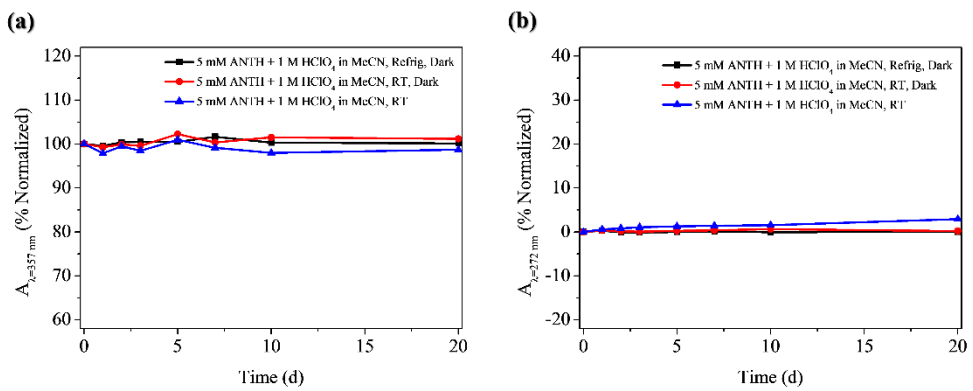

Fig. 2−33 Stability check of ANTH in 1 M $HClO_4$−MeCN solution.

2.3.5 Chemical and electrochemical analyses

The structural and electrochemical characterization by ^{1}H−NMR, LC−MS, and cyclic voltammetry are organized in this section. The lists contain the product mixture, standard compounds for reactant, internal standard, and products.

The reaction mixtures are organized below.

The raw data of ^{1}H−NMR (Fig. 2−34) and LC−MS (Fig. 2−35) of the product mixture of anthraquinone (AQ, **2a**) after the electroorganic reaction of anthracene (ANTH, **1a**) for days on defective 200 nm n^{+}−Si/SiO_2. In case of Fig. 2−34, large peaks of **2a** observed together with **1a**. Chemical shifts under 6 ppm seem to be impurities.

The raw data of ^{1}H−NMR (Fig. 2−36) and LC−MS (Fig. 2−37) of the product mixture of anthraquinone (AQ, **2a**) after the reaction of anthracene (ANTH, **1a**) for 12 h on defective 200 nm n^{+}−Si/SiO_2. In case of Fig. 2−36, slight peaks of **2a** observed. Chemical shifts under 6 ppm seem to be impurities.

The raw data of LC−MS (Fig. 2−38) of the product mixture of 2−methylanthraquinone (2−Me−AQ, **2b**) after the reaction of 2−methylanthracene (2−Me−ANTH, **1b**) for days on defective 200 nm n^{+}−Si/SiO_2.

The raw data of LC−MS (Fig. 2−39) of the product mixture of 9−anthracenecarboxaldehyde (9−CHO−ANTH, **2c**) after the reaction of 9−methylanthracene (9−Me−ANTH, **1c**) for days on defective 200 nm n^{+}−Si/SiO_2.

The raw data of LC-MS (Fig. 2-40) of the product mixture of anthraquinone (AQ, **2a**) after the reaction of 9-anthracenecarboxylic acid (9-COOH-ANTH, **1d**) for days on defective 200 nm n^+-Si/SiO_2..

The magnified version of Fig. 2-27, LC-MS attached as Fig. 2-41). Intermediate capture of ANTH (**1a**) reaction on n^+-Si/SiO_2 with TEMPO.

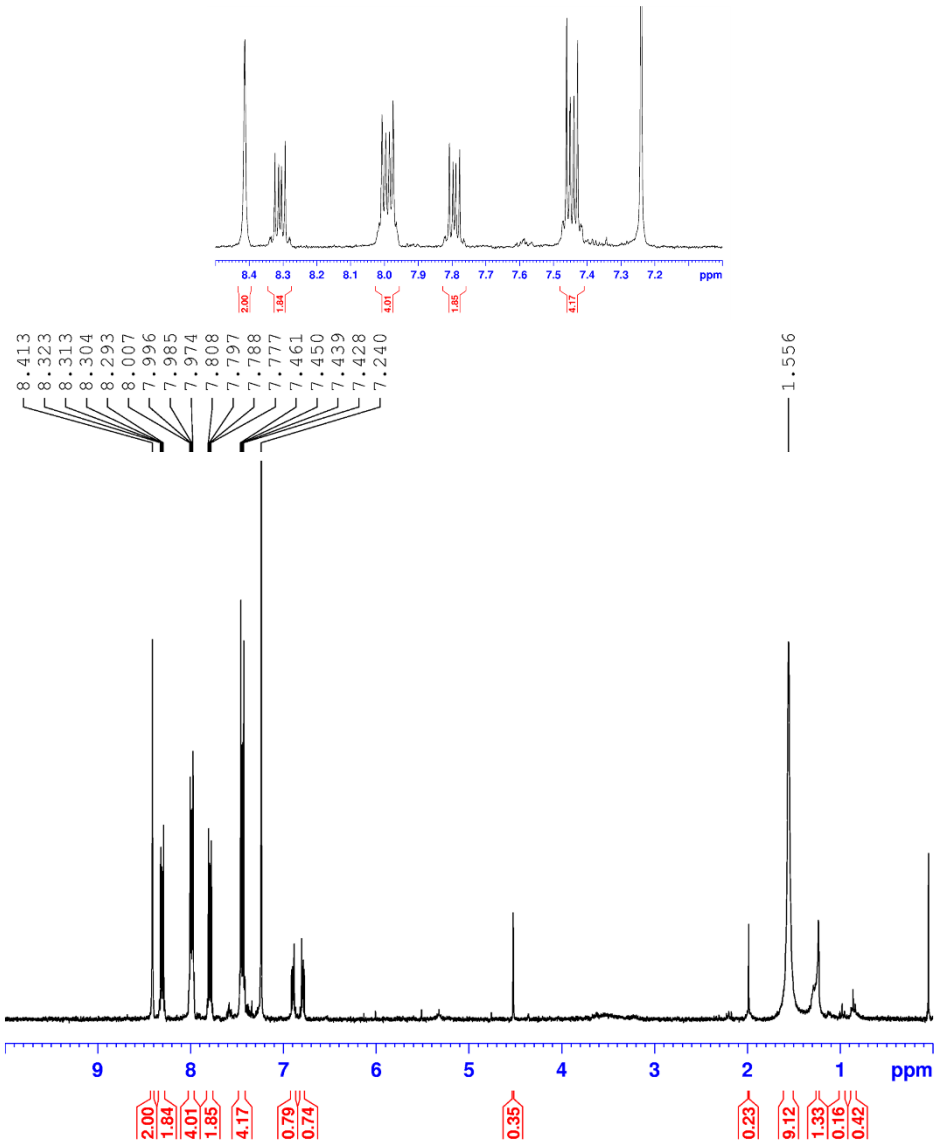

Fig. 2-34 The raw data of ^{1}H-NMR of the product mixture of anthraquinone (AQ, **2a**) after the electroorganic reaction of anthracene (ANTH, **1a**) for days on defective 200 nm n^{+}-Si/SiO_2.

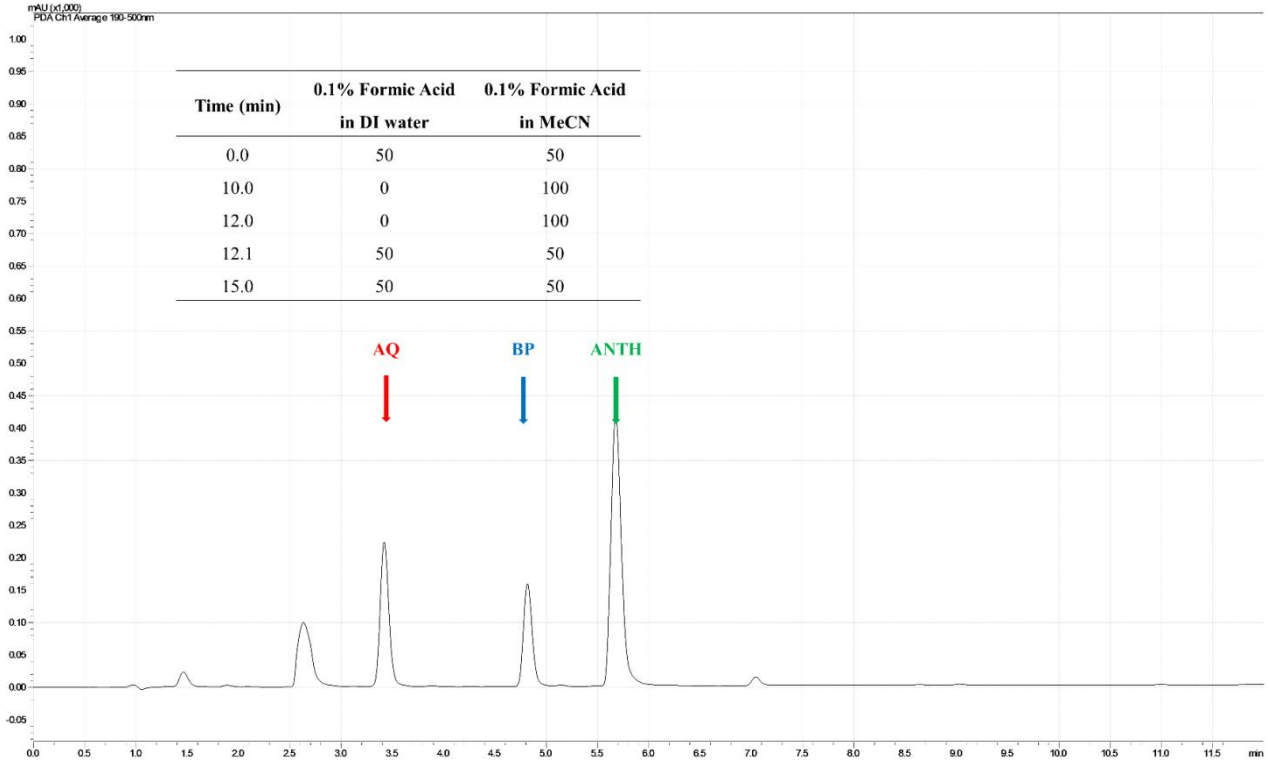

Time (min)	0.1% Formic Acid in DI water	0.1% Formic Acid in MeCN
0.0	50	50
10.0	0	100
12.0	0	100
12.1	50	50
15.0	50	50

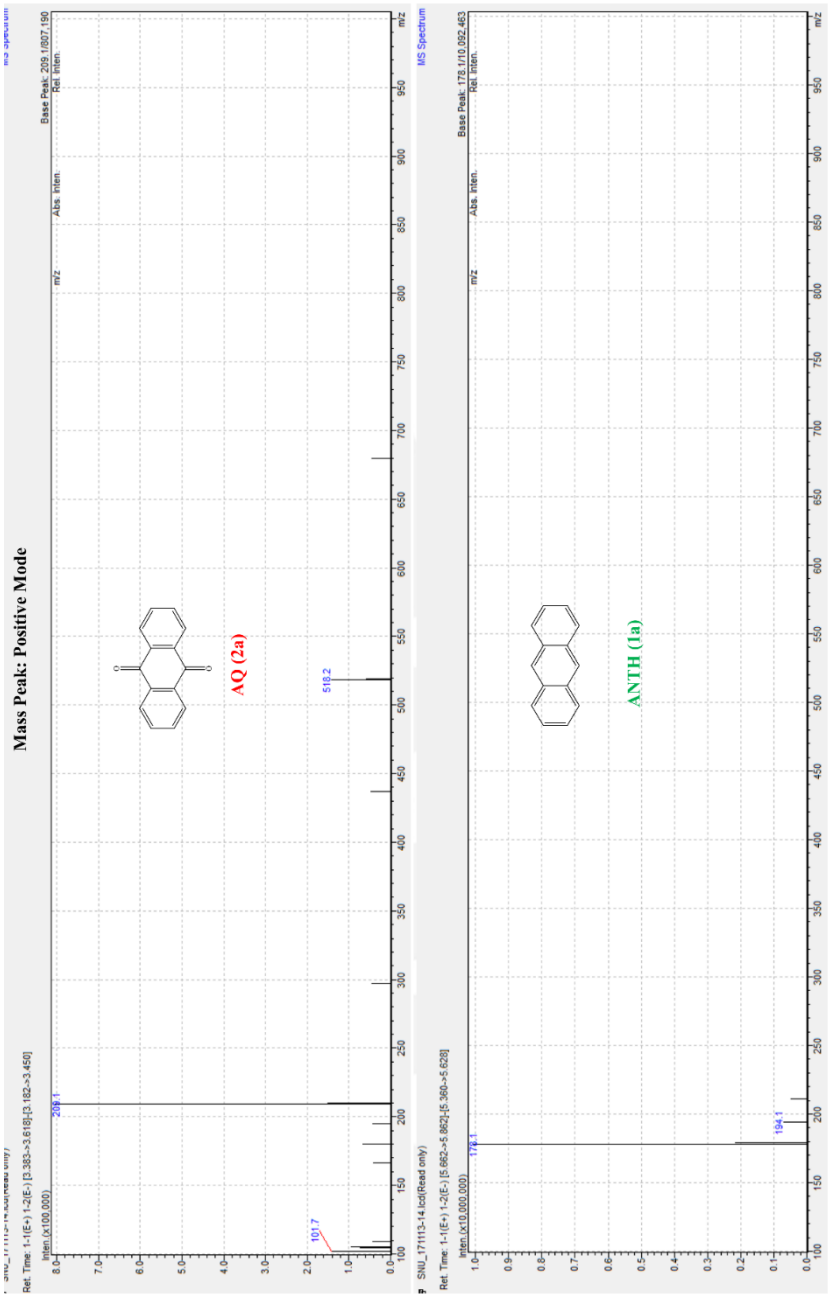

Fig. 2-35 The raw data of LC-MS of the product mixture of anthraquinone (AQ, **2a**) after the electroorganic reaction of anthracene (ANTH, **1a**) for days on defective 200 nm n^+-Si/SiO_2. Biphenyl was included as the internal standard.

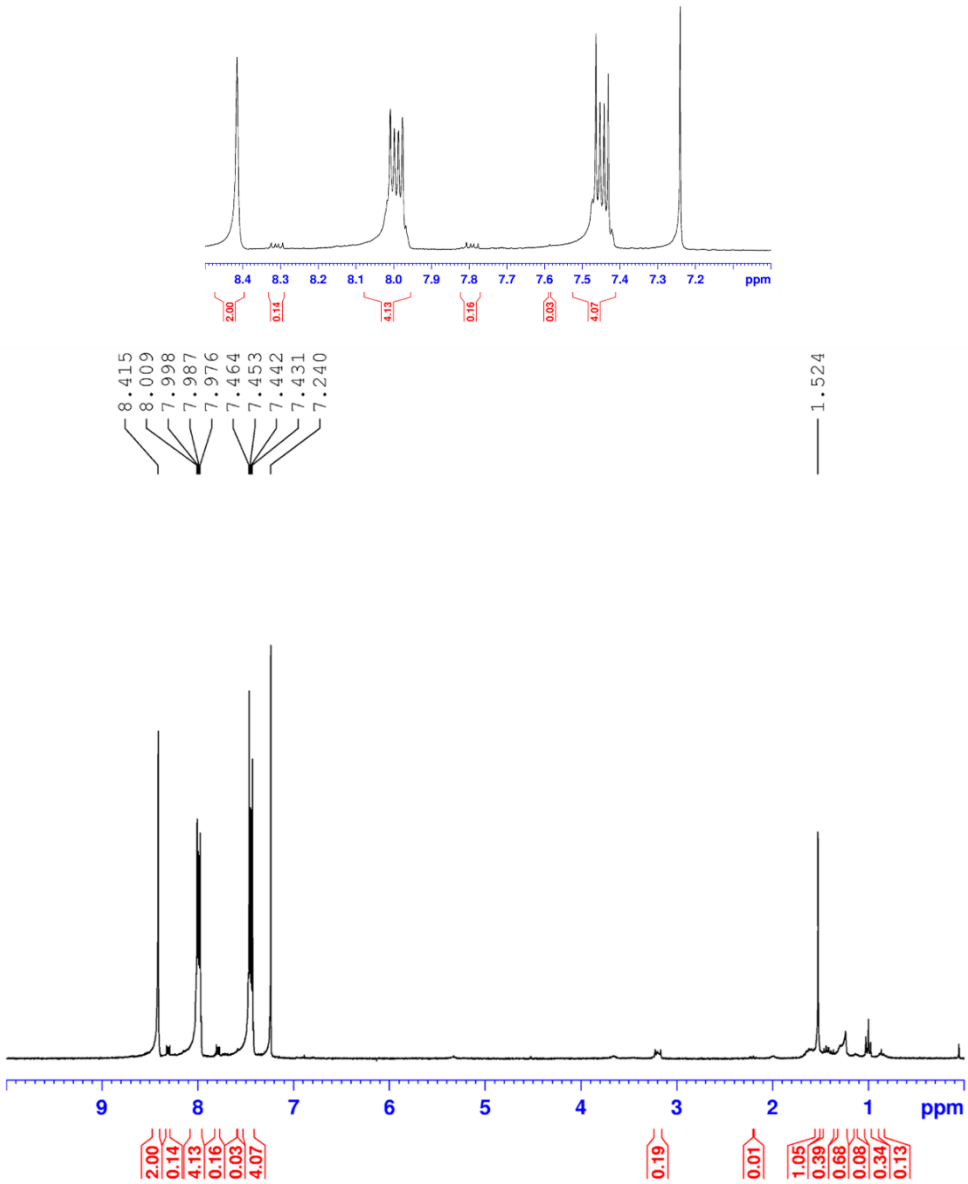

Fig. 2-36 The raw data of ^{1}H-NMR of the product mixture of anthraquinone (AQ, **2a**) after the electroorganic reaction of anthracene (ANTH, **1a**) for 12 h on defective 200 nm n^{+}-Si/SiO_2.

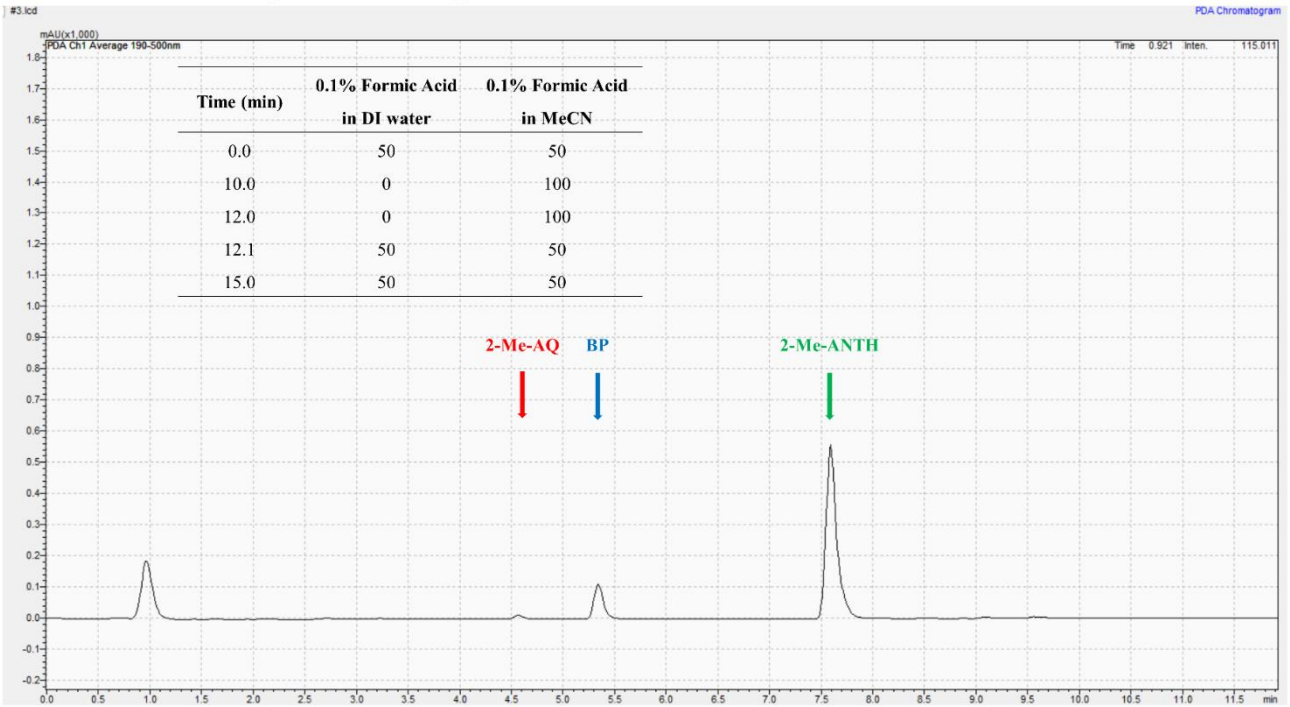

Time (min)	0.1% Formic Acid in DI water	0.1% Formic Acid in MeCN
0.0	50	50
10.0	0	100
12.0	0	100
12.1	50	50
15.0	50	50

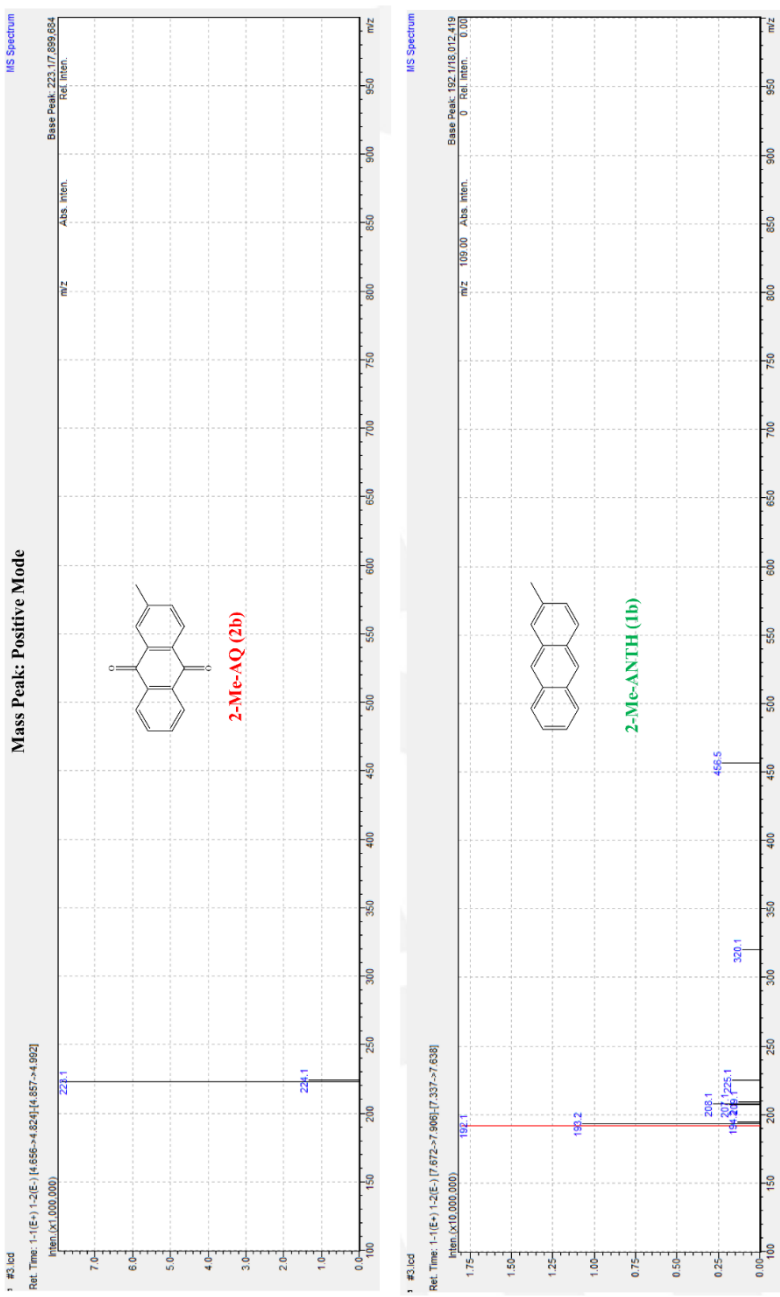

Fig. 2-37 The raw data of LC-MS of the product mixture of anthraquinone (AQ, **2a**) after the electroorganic reaction of anthracene (ANTH, **1a**) for days on defective 200 nm n^+-Si/SiO_2. Biphenyl was included as the internal standard.

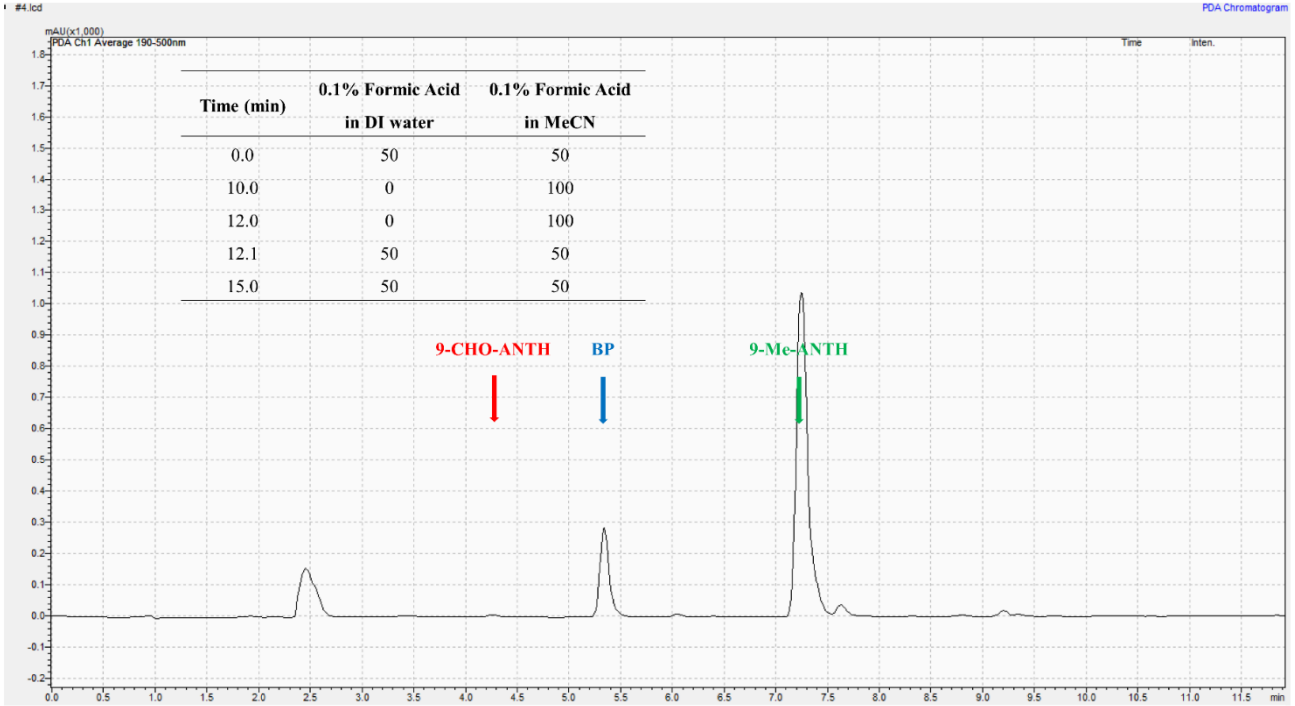
#4.lcd
PDA Chromatogram
mAU(x1,000)
PDA Ch1 Average 190-500nm
Time
Inten.
Time (min) | 0.1% Formic Acid in DI water | 0.1% Formic Acid in MeCN
0.0 | 50 | 50
10.0 | 0 | 100
12.0 | 0 | 100
12.1 | 50 | 50
15.0 | 50 | 50
9-CHO-ANTH
BP
9-Me-ANTH
min

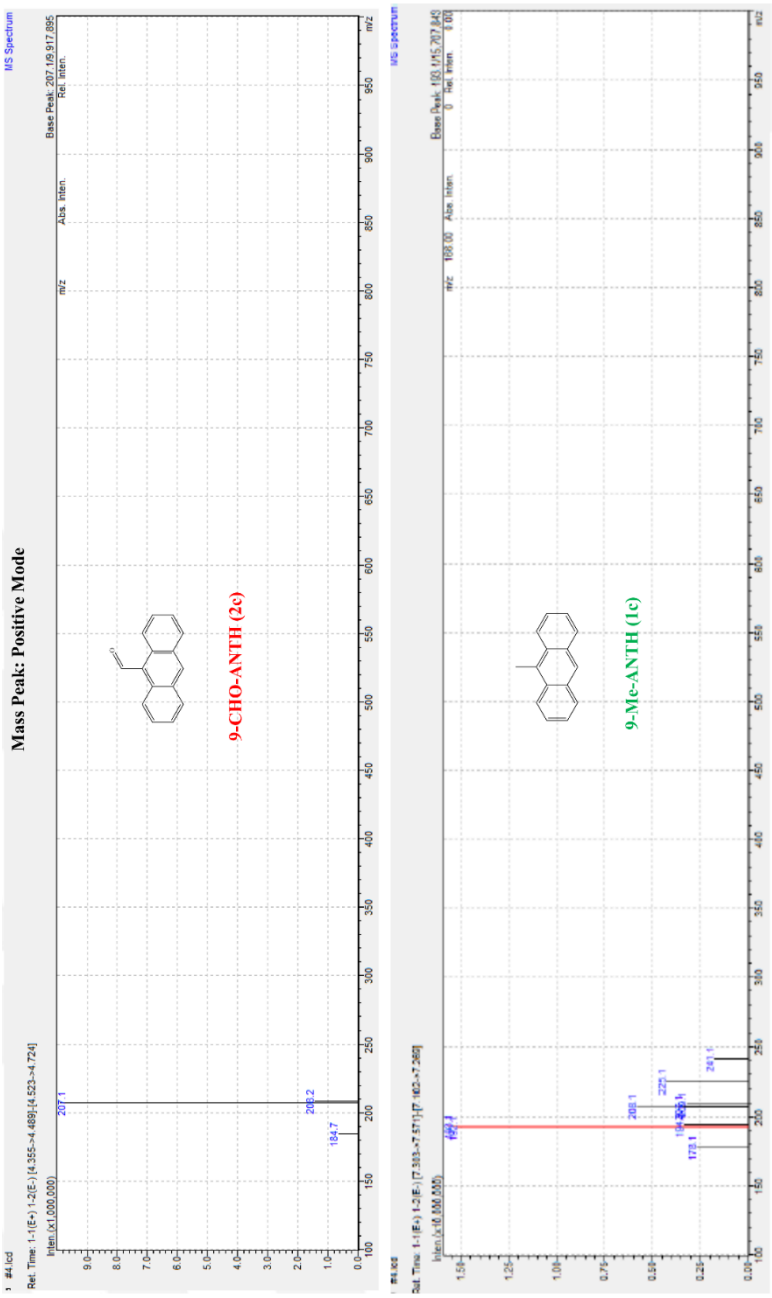

Fig. 2-38 The raw data of LC-MS of the product mixture of 2-methylanthraquinone (2-Me-AQ, **2b**) after the reaction of 2-methylanthracene (2-Me-ANTH, **1b**) for days on defective 200 nm n^+-Si/SiO_2. Biphenyl was included as the internal standard.

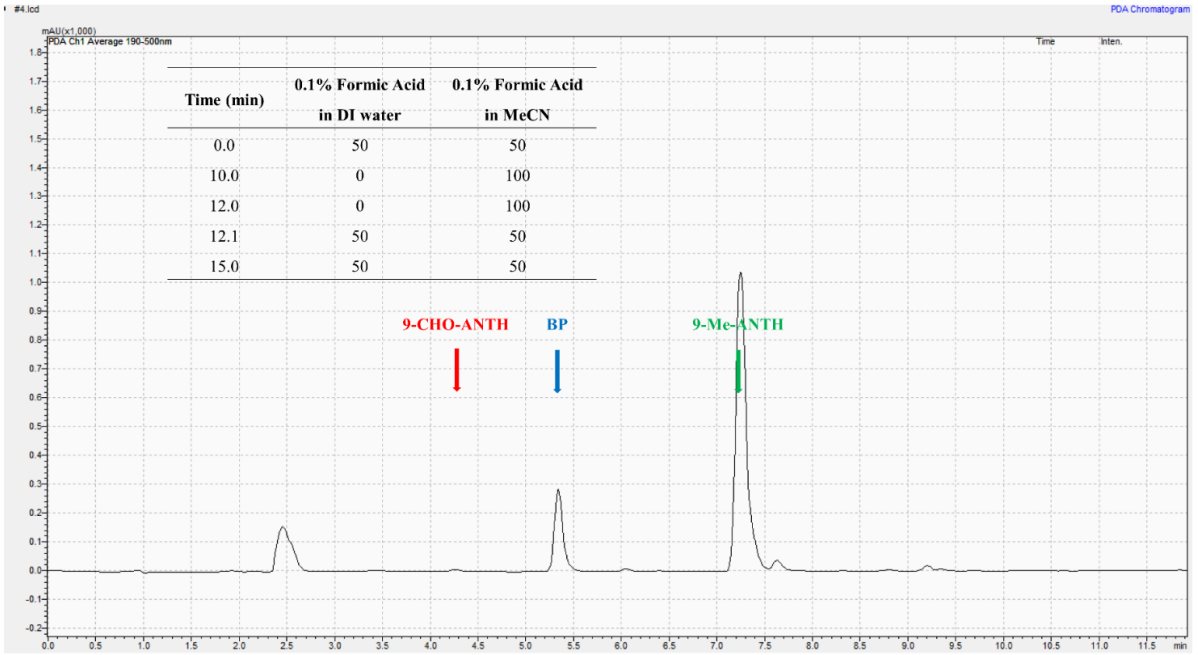
#4.lcd
PDA Chromatogram
mAU(x1,000)
PDA Ch1 Average 190-500nm
Time
Inten.
Time (min) | 0.1% Formic Acid in DI water | 0.1% Formic Acid in MeCN
0.0 | 50 | 50
10.0 | 0 | 100
12.0 | 0 | 100
12.1 | 50 | 50
15.0 | 50 | 50
9-CHO-ANTH
BP
9-Me-ANTH
min

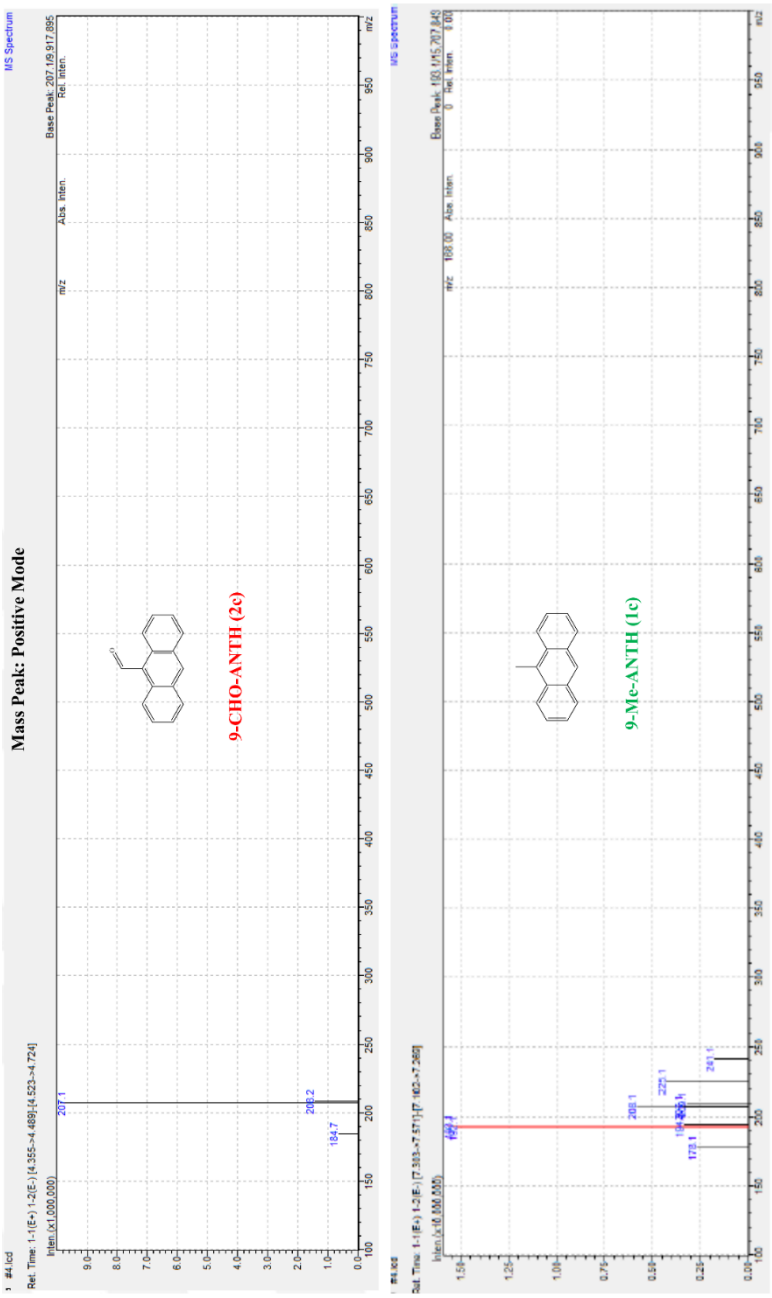

Fig. 2-39 The raw data of LC-MS of the product mixture of 9-anthracenecarboxaldehyde (9-CHO-ANTH, **2c**) after the reaction of 9-methylanthracene (9-Me-ANTH, **1c**) for days on defective 200 nm n^+-Si/SiO_2. Biphenyl was included as the internal standard.

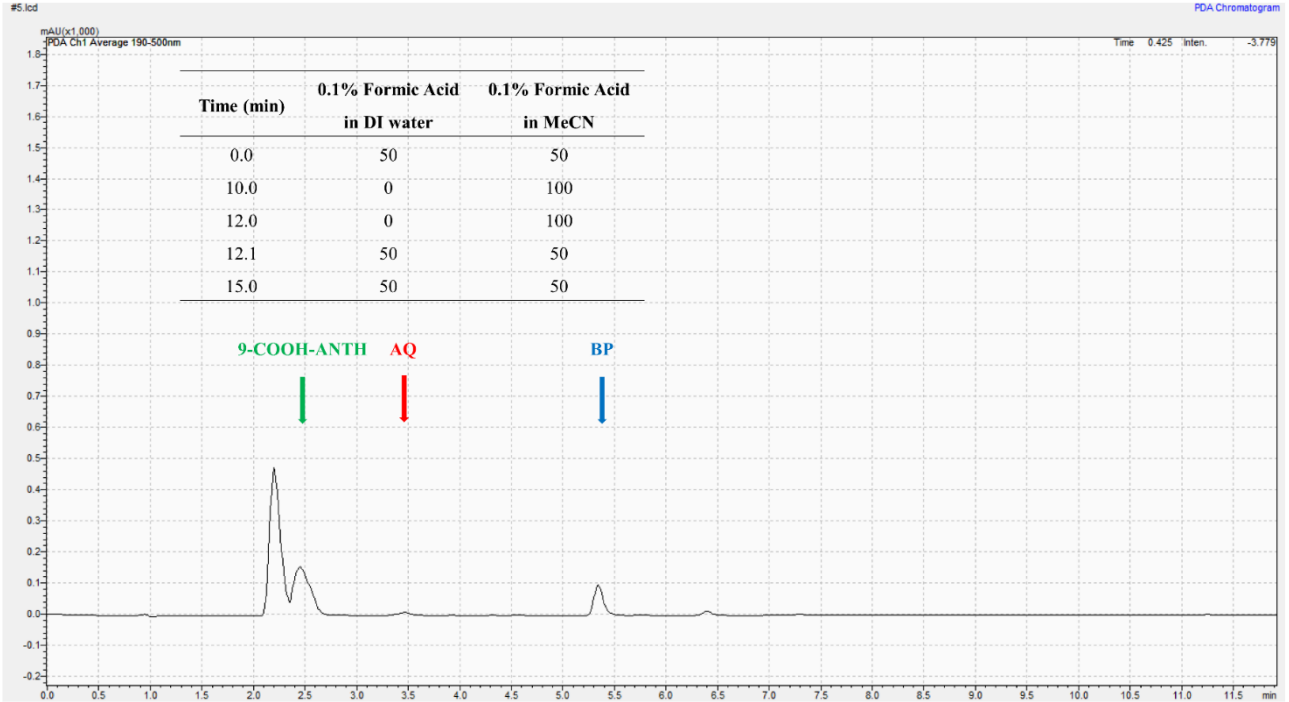

Time (min)	0.1% Formic Acid in DI water	0.1% Formic Acid in MeCN
0.0	50	50
10.0	0	100
12.0	0	100
12.1	50	50
15.0	50	50

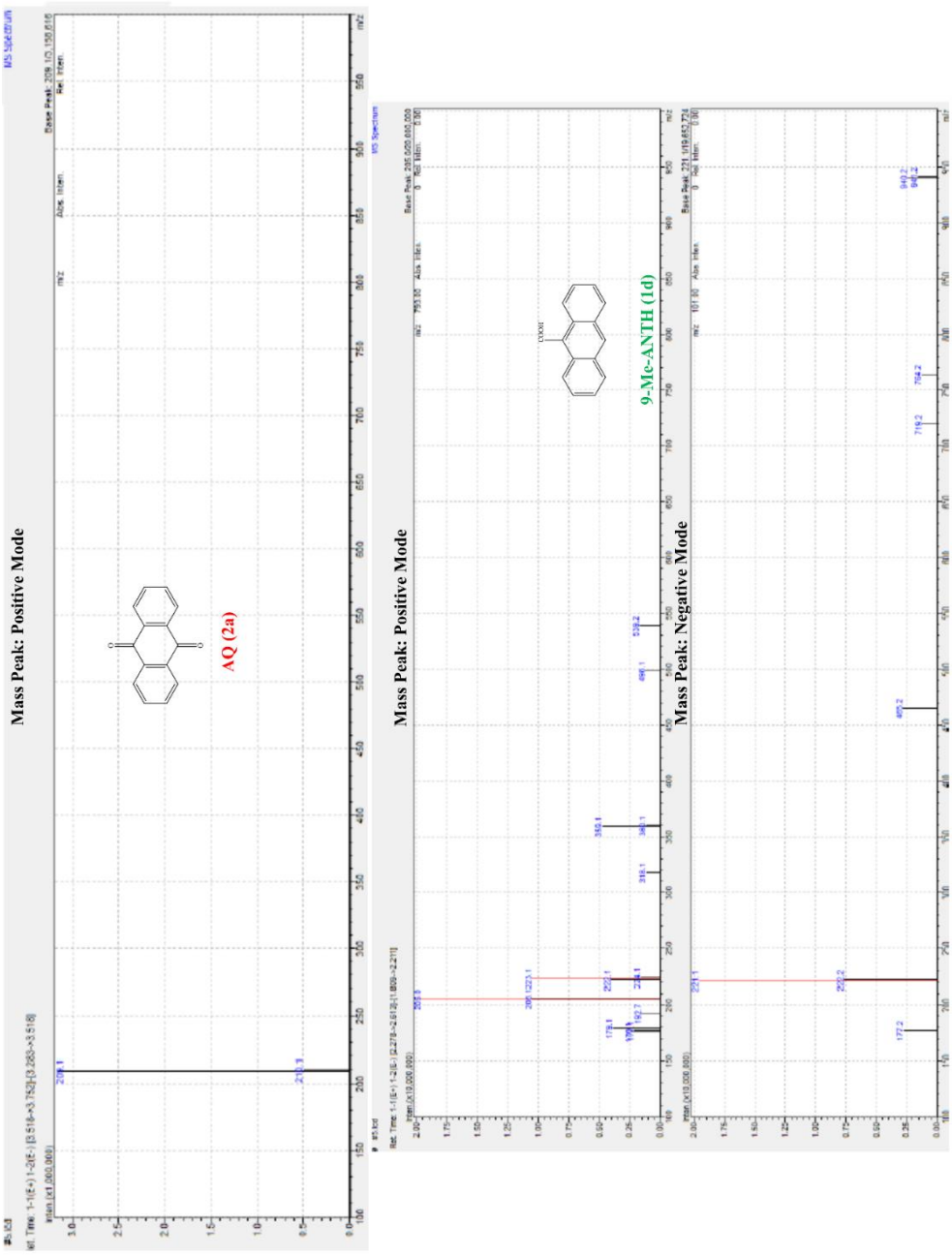

Fig. 2-40 The raw data of LC-MS of the product mixture of anthraquinone (AQ, **2a**) after the reaction of 9-anthracenecarboxylic acid (9-COOH-ANTH, **1d**) for days on defective 200 nm n^+-Si/SiO_2. Biphenyl was included as the internal standard.

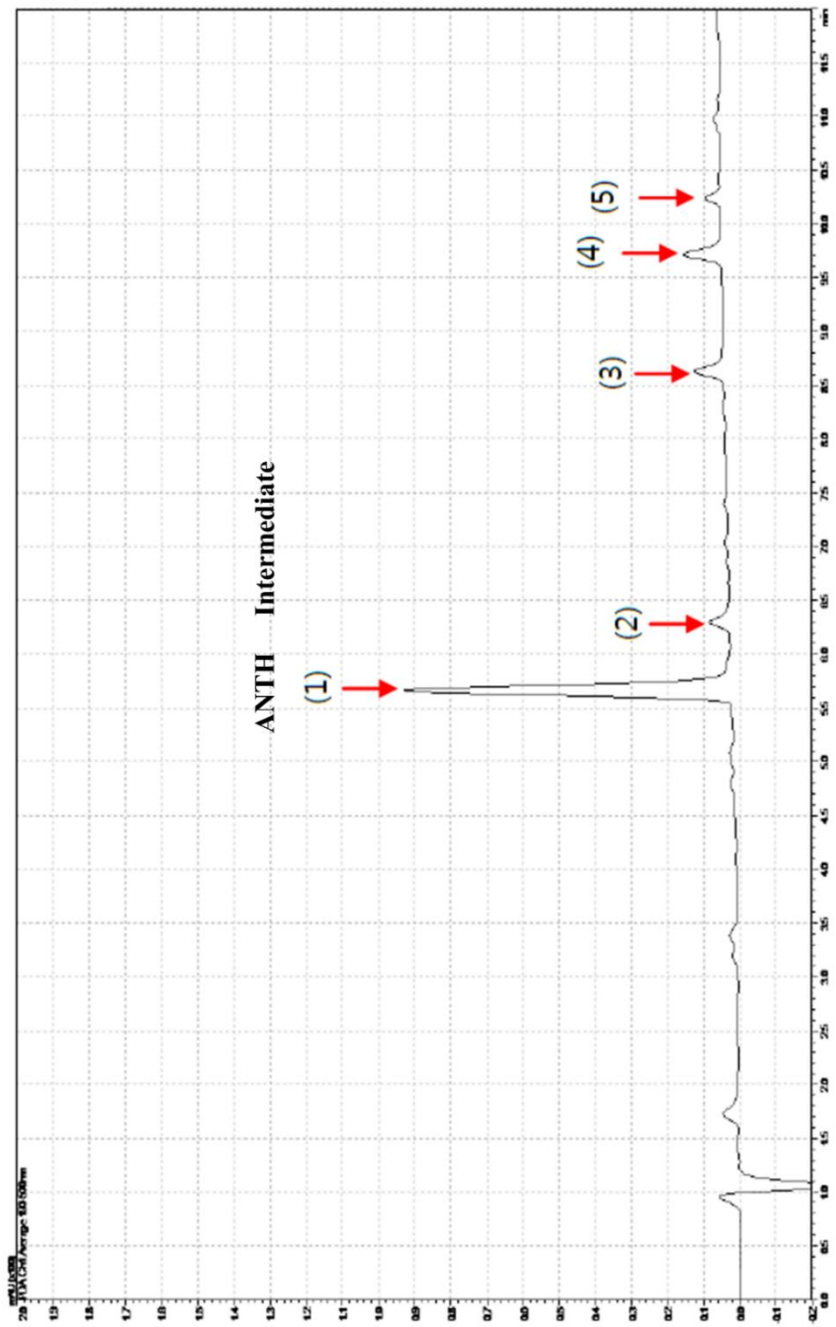
ANTH Intermediate
(1)
(2)
(3)
(4)
(5)

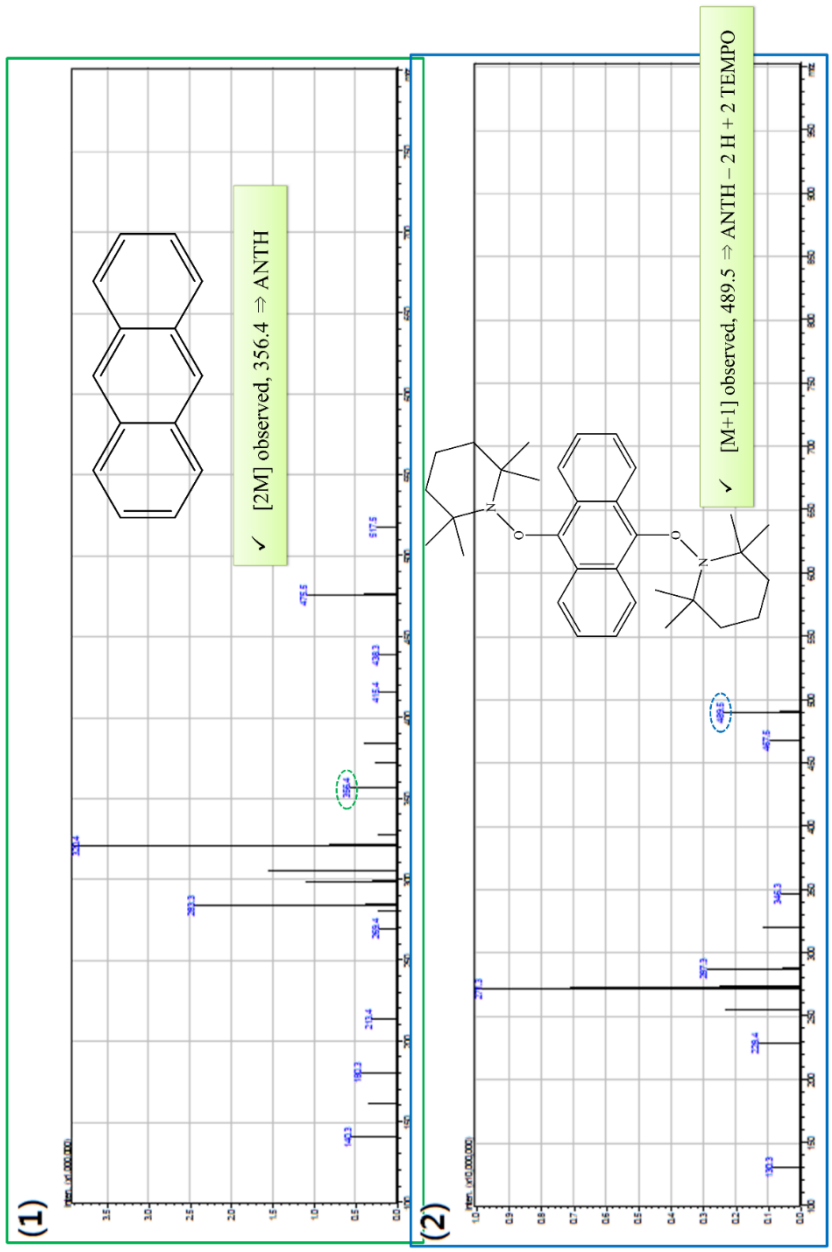

Fig. 2-41 The magnified version of Fig. 2-27, LC-MS attached. Intermediate capture of ANTH (**1a**) reaction on n^+-Si/SiO_2 with TEMPO.

The starting compounds are organized below.

Anthracene (**1a**): Purchased from Sigma Aldrich (≥99.0% GC) and used as received. ^{1}H−NMR (300 MHz, $CDCl_3$): δ 8.42 (s, 2H), 7.98 (dd, J = 6.6, 3.0 Hz, 4H), 7.45 (dd, J = 6.6, 3.0 Hz, 4H). LC−MS (APCI): calcd. for $C_{14}H_{11}$ $[M+H]^+$ 179; found 178.1 as $C_{14}H_{10}$ [M]. Sometimes observed [2M] calcd. as $C_{28}H_{20}$ 356; found 356.4.

The raw data of ^{1}H−NMR (Fig. 2−42) and LC−MS (Fig. 2−43) are attached for **1a**. The cyclic voltammetry of **1a** on glassy carbon electrode is previously attached (Fig. 2−17)

2−Methylanthracene (**1b**): Purchased from Sigma Aldrich (97%) and used as received. ^{1}H−NMR (300 MHz, $CDCl_3$): δ 8.37 (s, 1H), 8.30 (s, 1H), 7.96 (dd, J = 4.8, 4.5 Hz, 2H), 7.90 (d, J = 8.7 Hz, 1H), 7.74 (s, 1H), 7.43 (m, 2H), 7.28 (d, J = 8.4 Hz, 1H), 2.54 (s, 3H). LC−MS (APCI): calcd. for $C_{15}H_{13}$ $[M+H]^+$ 193; found 192.1 as $C_{15}H_{12}$ [M].

The raw data of ^{1}H−NMR (Fig. 2−44) and cyclic voltammetry on glassy carbon electrode (Fig. 2−45) are attached for **1b**.

9−Methylanthracene (**1c**): Purchased from Sigma Aldrich (98%) and used as received. ^{1}H−NMR (300 MHz, $CDCl_3$): δ 8.33 (s, 1H), 8.28 (ddd, J = 8.1, 2.4, 0.9 Hz, 2H), 7.99 (dd, J = 8.1, 0.6 Hz, 2H), 7.47 (m, 4H), 3.09 (d, J = 0.6 Hz, 3H). LC−MS (APCI): calcd. for $C_{15}H_{13}$ $[M+H]^+$ 193; found 192.1 as $C_{15}H_{12}$ [M].

The raw data of ^{1}H−NMR (Fig. 2−46) and cyclic voltammetry on glassy carbon electrode (Fig. 2−47) are attached for **1c**.

9−Anthracenecarboxylic acid (**1d**): Purchased from Sigma Aldrich (99%) and used as received. ^{1}H−NMR (300 MHz, $CDCl_3$): δ 8.59 (s,

1H), 8.32 (d, J = 8.7 Hz, 2H), 8.05 (d, J = 8.4 Hz, 2H), 7.60 (m, 2H), 7.52 (m, 2H). 1H from the carboxylic acid not found. LC-MS (APCI): calcd. for $C_{15}H_{11}O_2$ $[M+H]^+$ 223; found 223.1.

The raw data of ^{1}H-NMR (Fig. 2-48) is attached for **1d**. The cyclic voltammetry of **1d** on the glassy carbon electrode is previously attached (Fig. 2-25).

Phenanthrene (**3a**): Purchased from Sigma Aldrich (≥98.0%) and used as received. ^{1}H-NMR (300 MHz, $CDCl_3$): δ 8.70 (d, J = 9.3 Hz, 2H), 7.91 (d, J = 8.7 Hz, 2H), 7.75 (s, 2H), 7.64 (m, 4H). LC-MS (APCI): calcd. $C_{14}H_{11}$ $[M+H]^+$; not found.

The raw data of ^{1}H-NMR (Fig. 2-49), LC-MS (Fig. 2-50), and cyclic voltammetry on glassy carbon electrode (Fig. 2-51) are attached for **3a**.

Pyrene (**4a**): Purchased from Sigma Aldrich (98%) and used as received. ^{1}H-NMR (300 MHz, $CDCl_3$): δ 8.18 (dd, J = 7.5, 1.5 Hz, 4H), 8.07 (d, J = 1.8 Hz, 4H), 8.01 (td, J = 8.1, 0.9 Hz, 2H). LC-MS (APCI): calcd. for $C_{16}H_{11}$ $[M+H]^+$ 203; found 203.2.

The raw data of ^{1}H-NMR (Fig. 2-52), LC-MS (Fig. 2-53), and cyclic voltammetry on glassy carbon electrode (Fig. 2-54) are attached for **4a**.

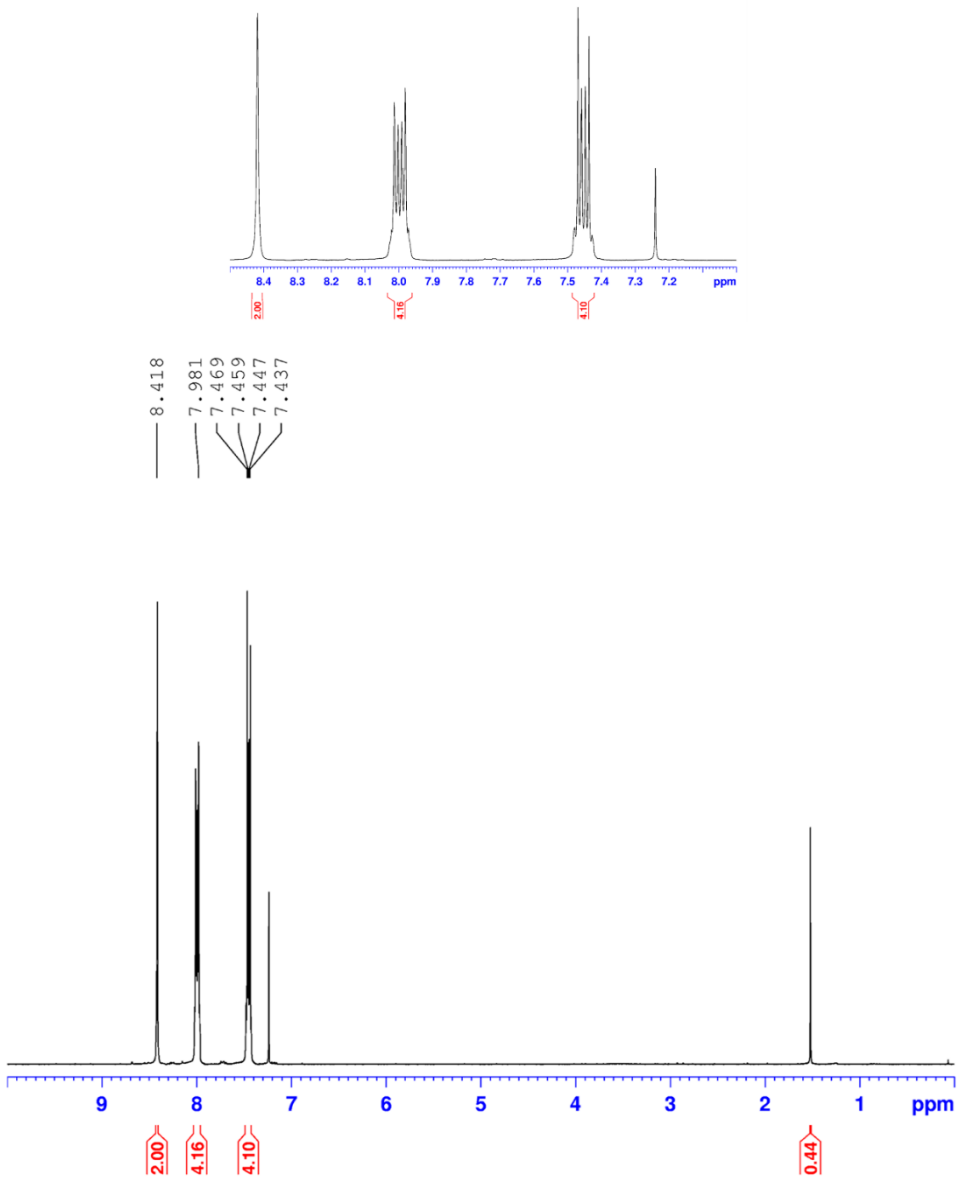

Fig. 2-42 The raw data of ^{1}H-NMR of 1a.

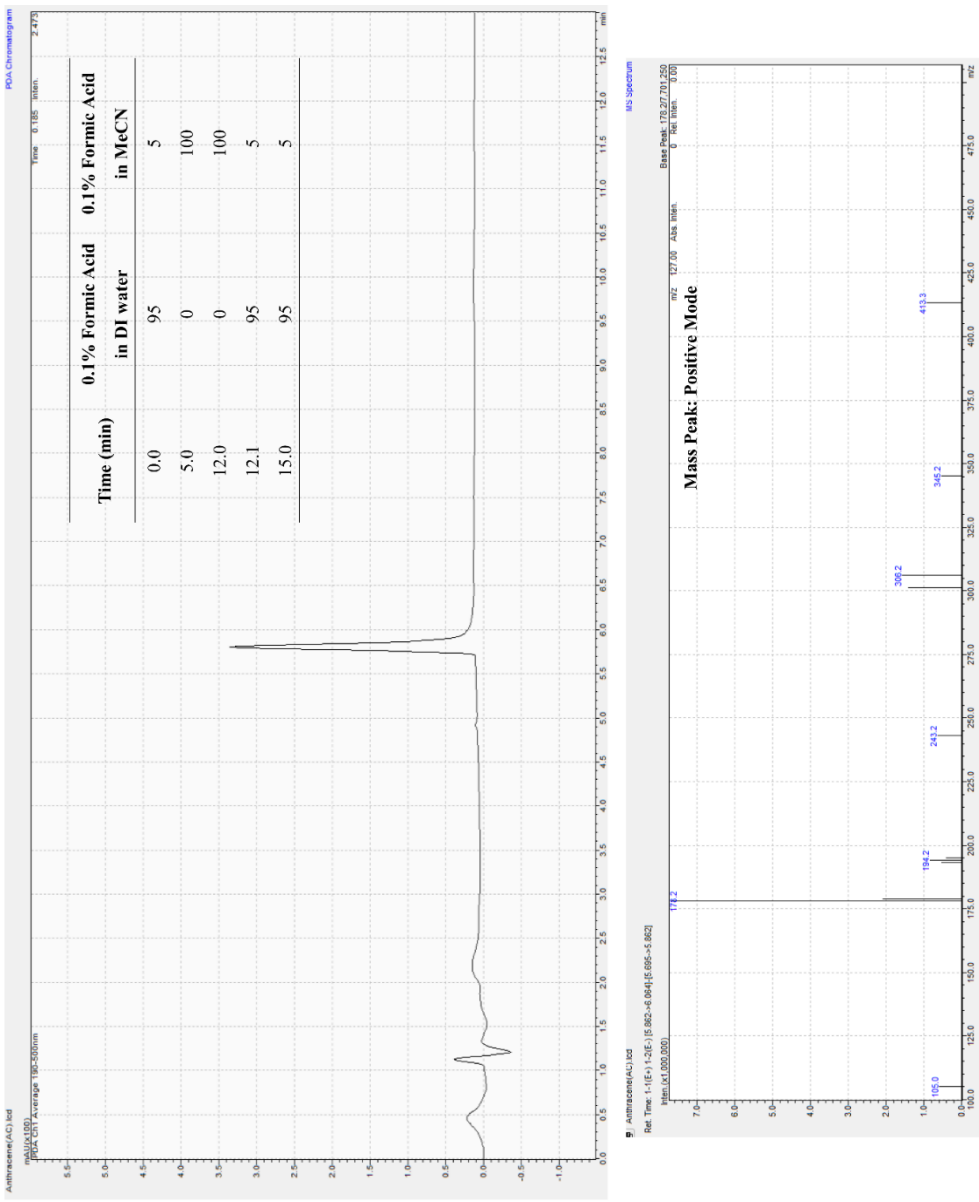

Fig. 2-43 The raw data of LC-MS of 1a.

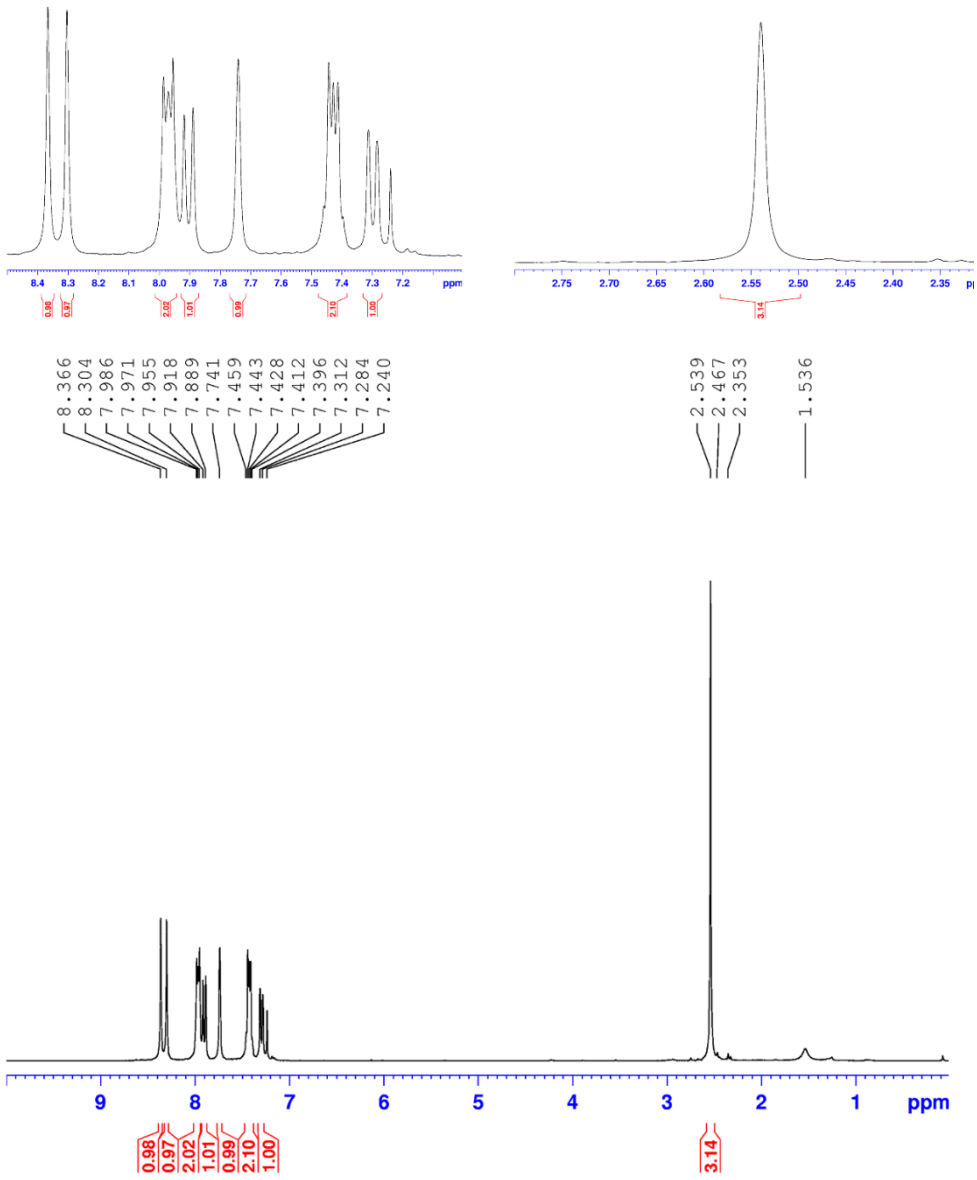

Fig. 2-44 The raw data of ^{1}H-NMR of **1b**.

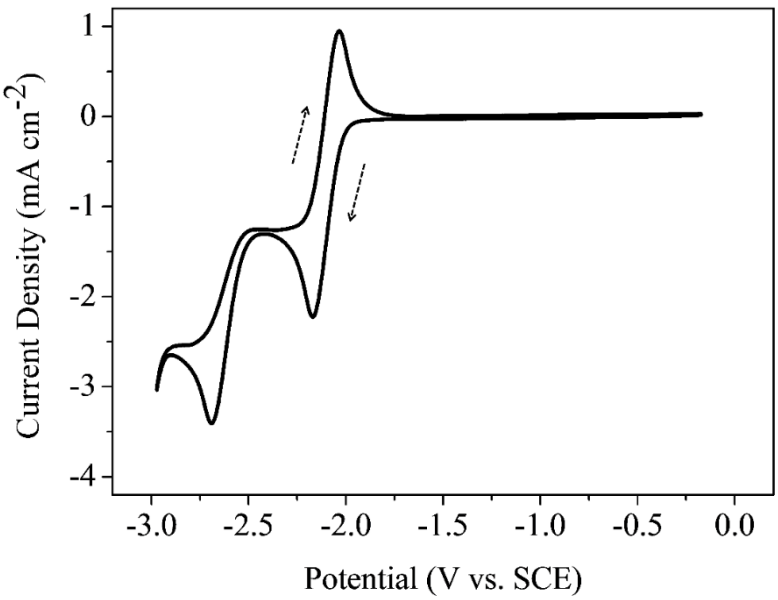

Fig. 2-45 The cyclic voltammetry of 1b on glassy carbon electrode.

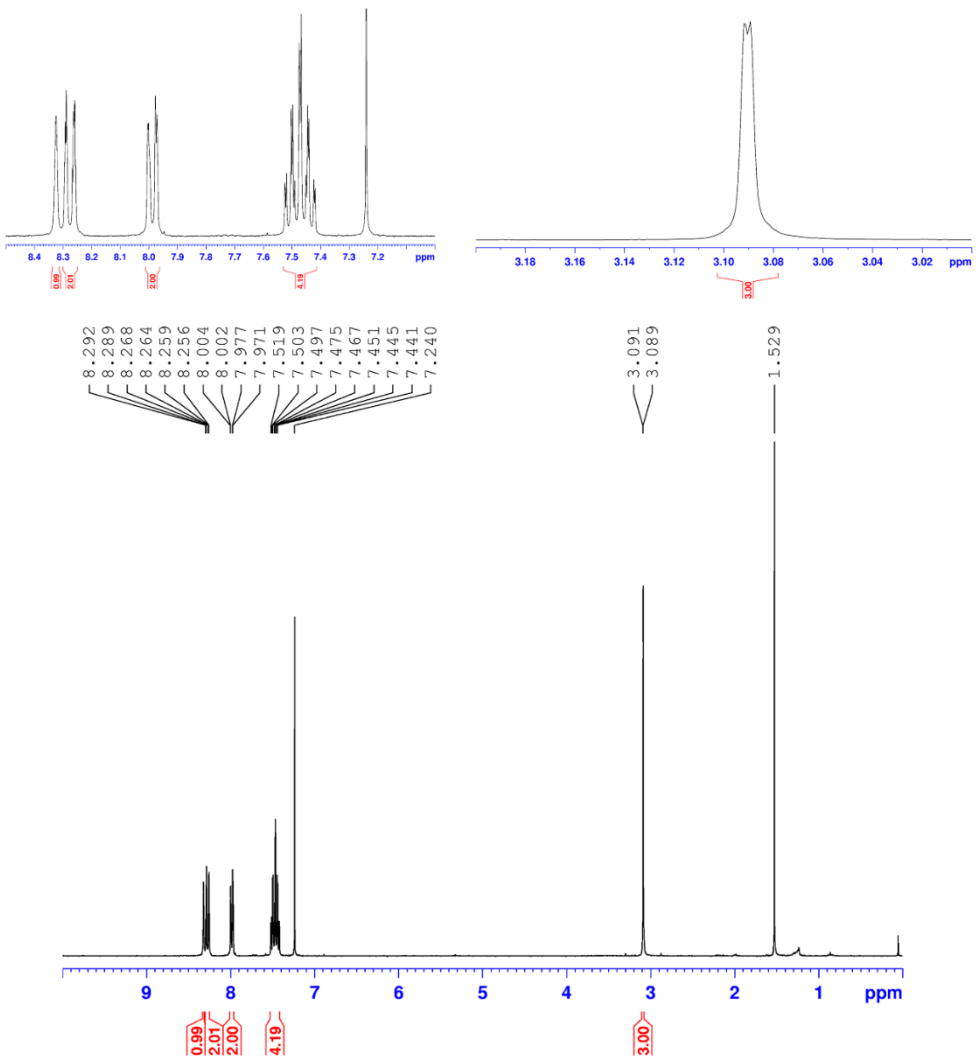

Fig. 2-46 The raw data of ^{1}H-NMR of **1c**.

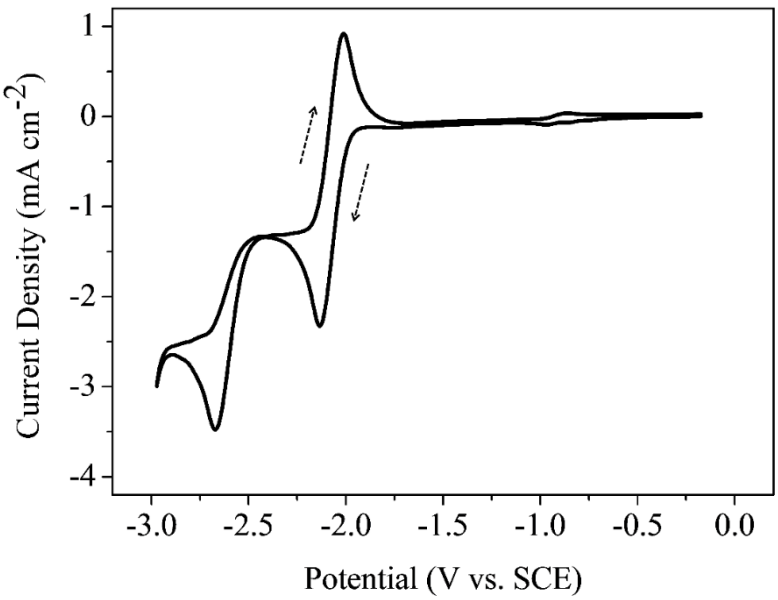

Fig. 2-47 The cyclic voltammetry of 1c on glassy carbon electrode.

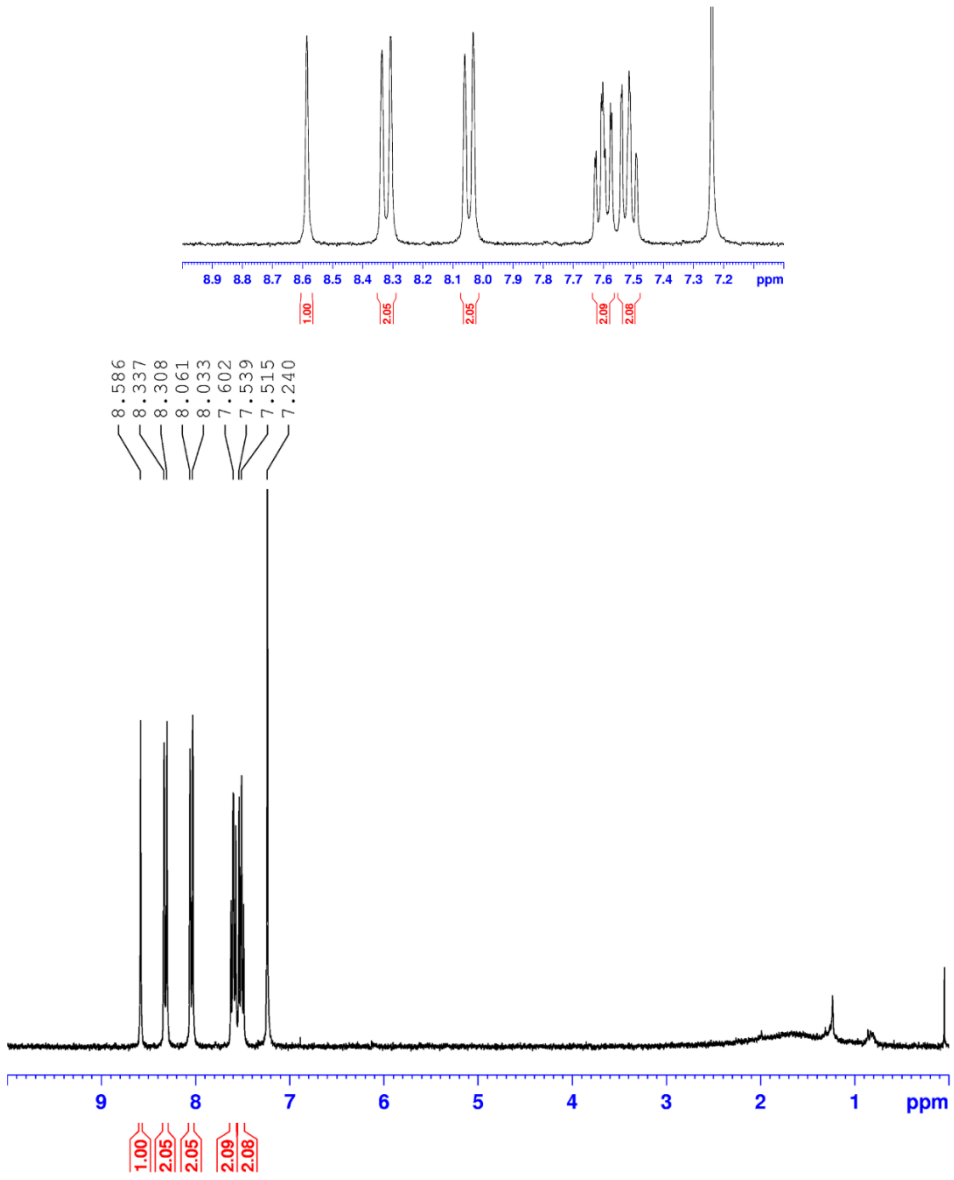

Fig. 2-48 The raw data of ^{1}H-NMR of 1d.

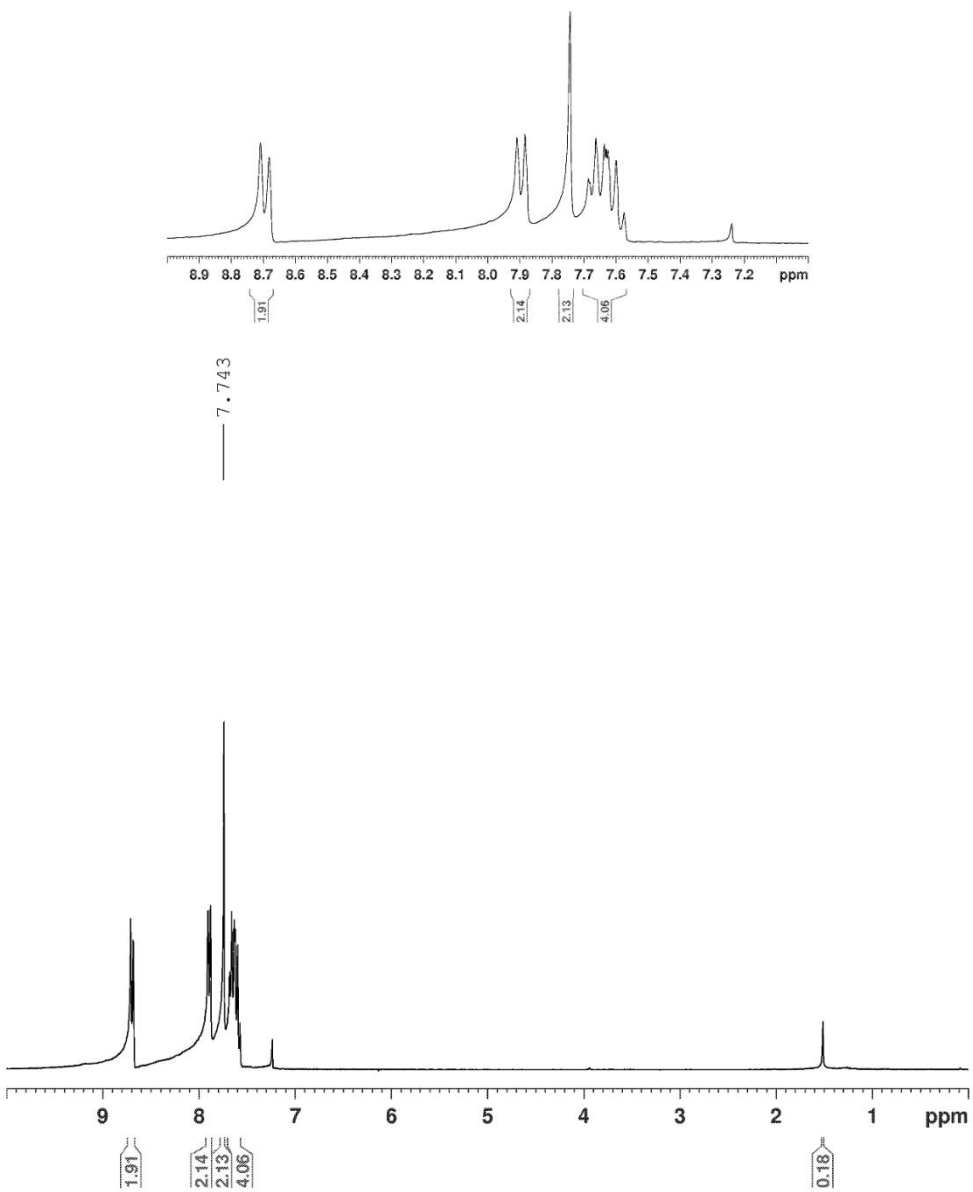

Fig. 2-49 The raw data of ^{1}H-NMR of 3a.

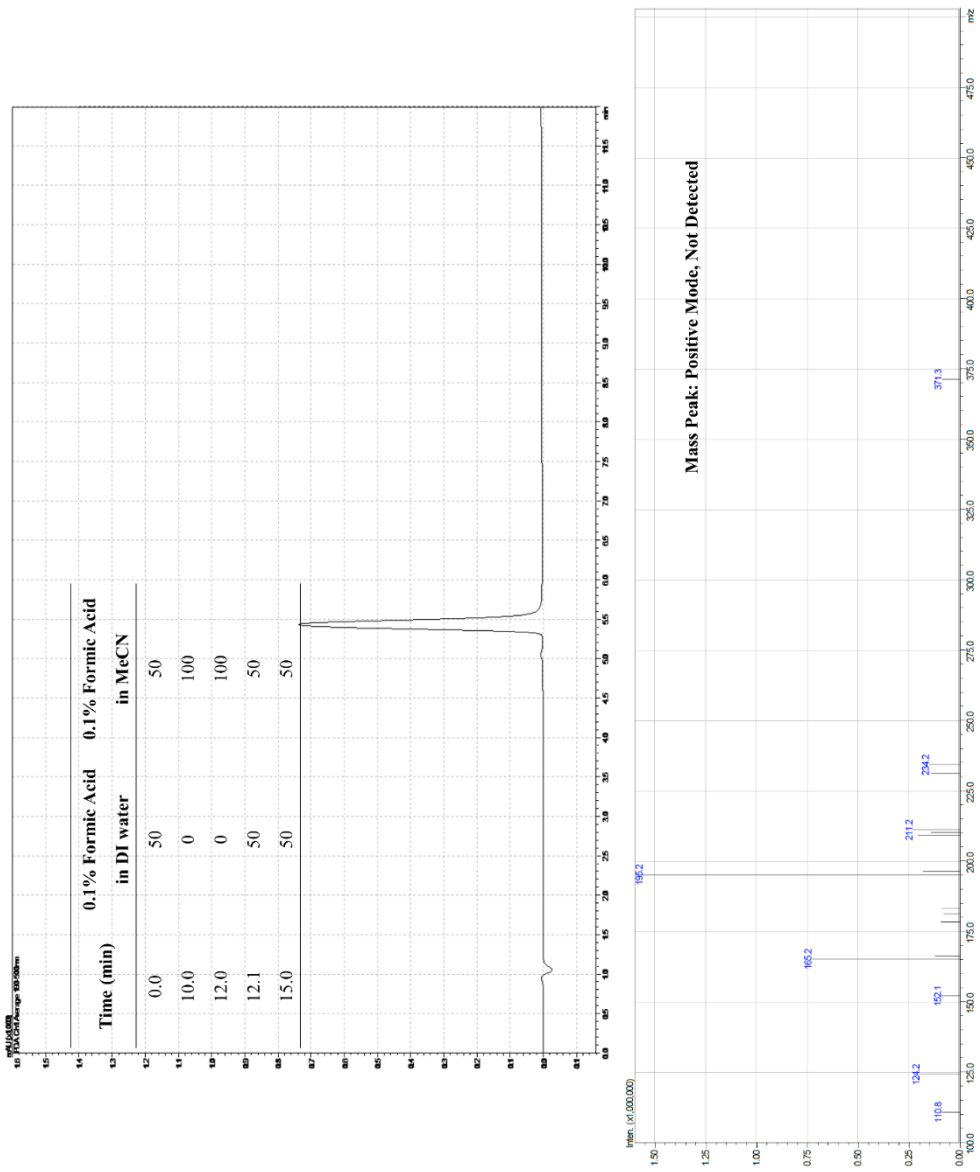

Fig. 2-50 The raw data of LC-MS of 3a.

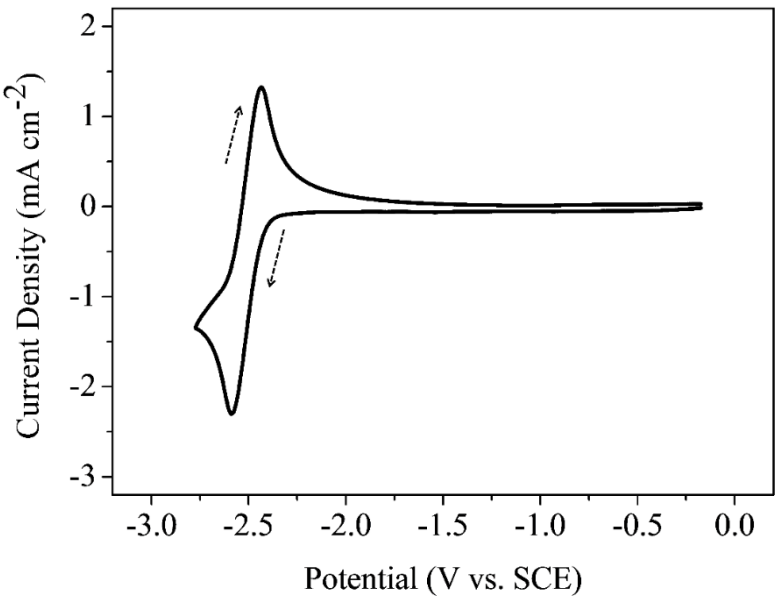

Fig. 2-51 The cyclic voltammetry of 3a on glassy carbon electrode.

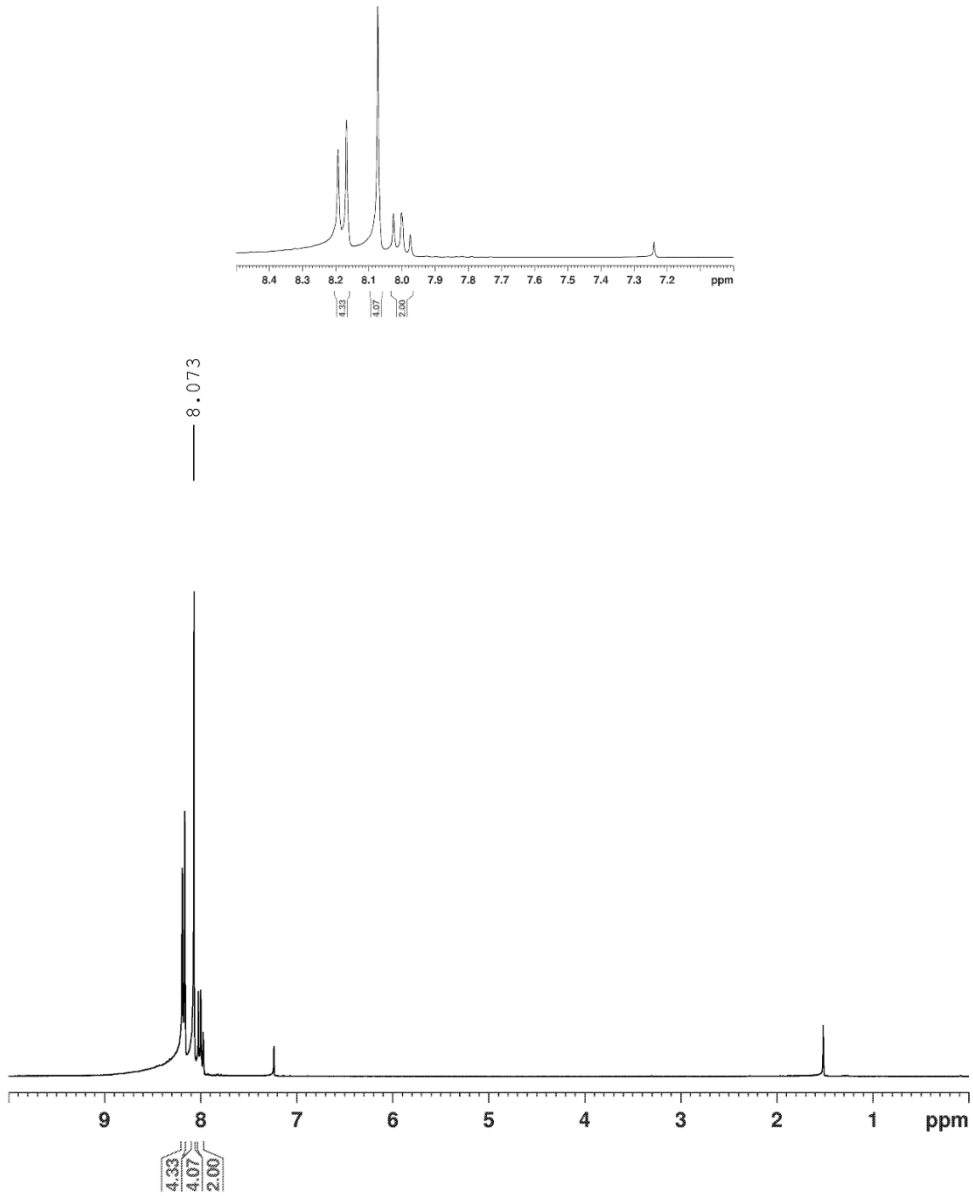

Fig. 2-52 The raw data of ^{1}H-NMR of 4a.

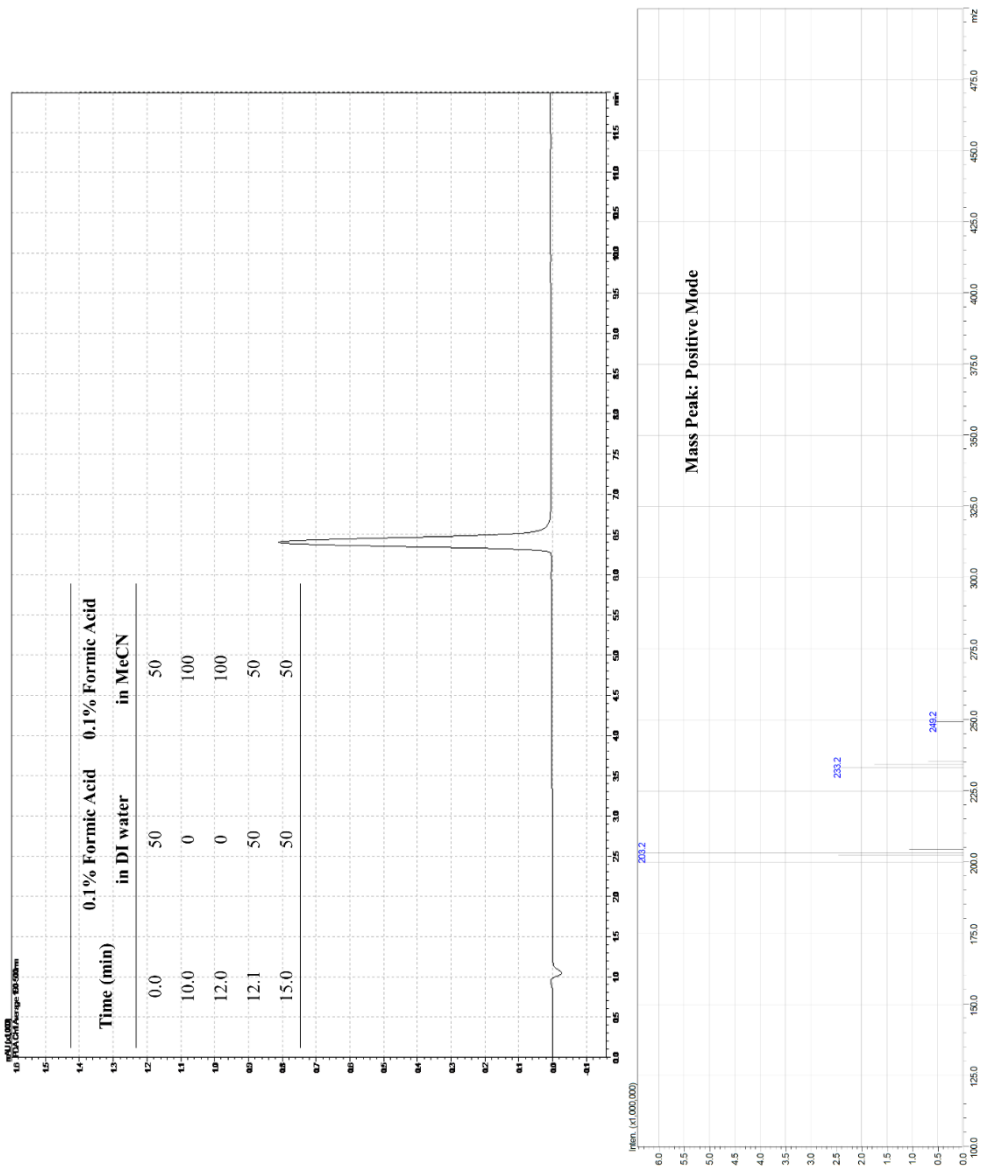

Fig. 2-53 The raw data of LC-MS of **4a**.

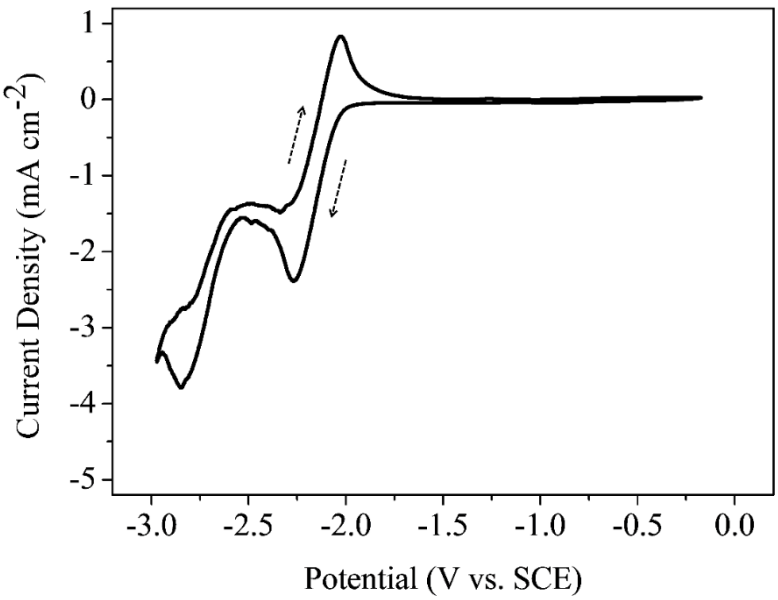

Fig. 2-54 The cyclic voltammetry of 4a on glassy carbon electrode.

The internal standard compound is organized below.

Biphenyl: Purchased from Sigma Aldrich (99.5%) and used as received. ^{1}H−NMR (300 MHz, CDCl3): δ 7.62 (ddd, J = 8.1, 2.4, 1.2 Hz, 4H), 7.46 (ddd, J = 8.1, 7.2, 1.5 Hz, 4H), 7.36 (m, 4H). LC−MS (APCI): not ionized, calcd. $C_{12}H_{11}$ $[M+H]^{+}$ 155.2; not found.

The raw data of ^{1}H−NMR (Fig. 2−55) and LC−MS (Fig. 2−56) are attached for BP.

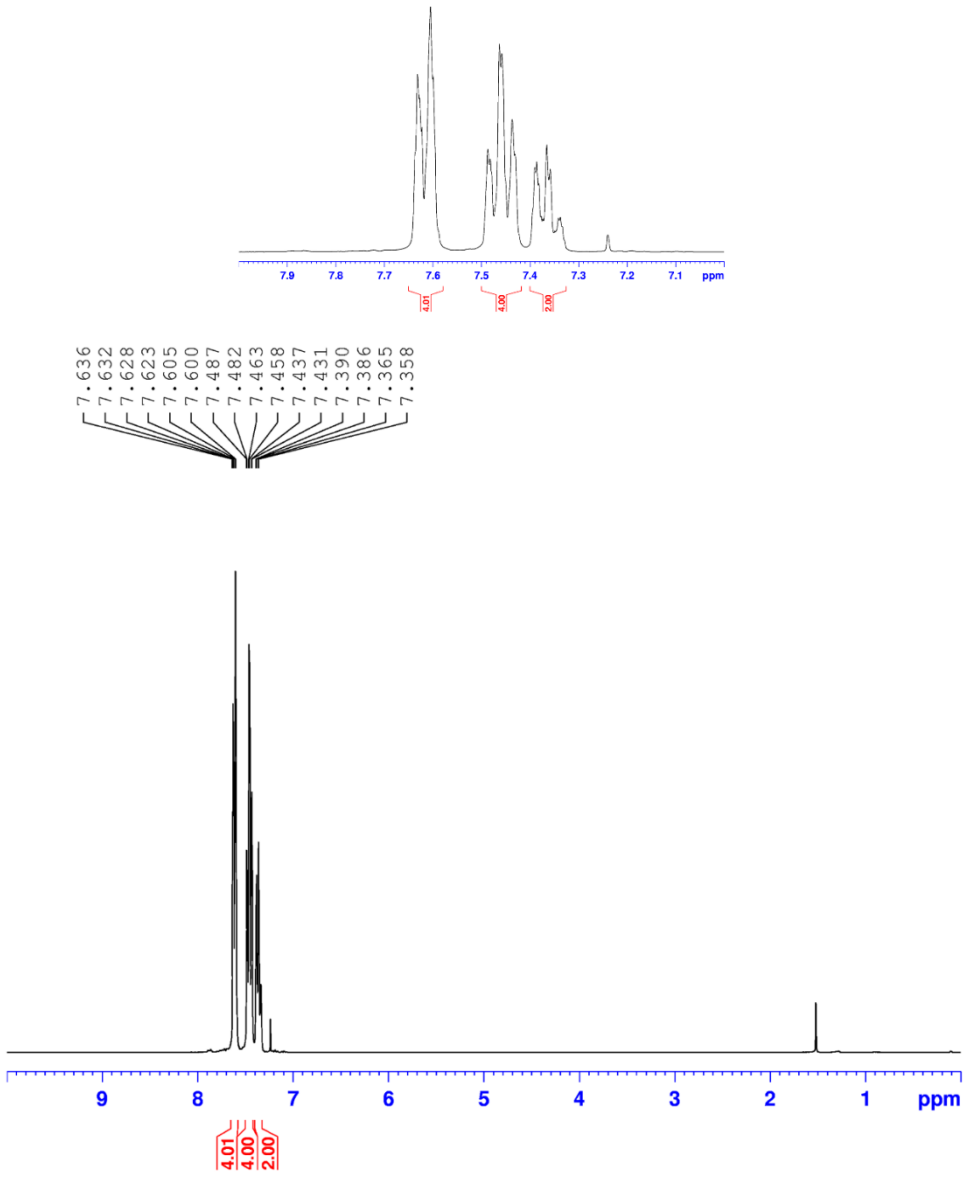

Fig. 2-55 The raw data of ^{1}H-NMR of BP.

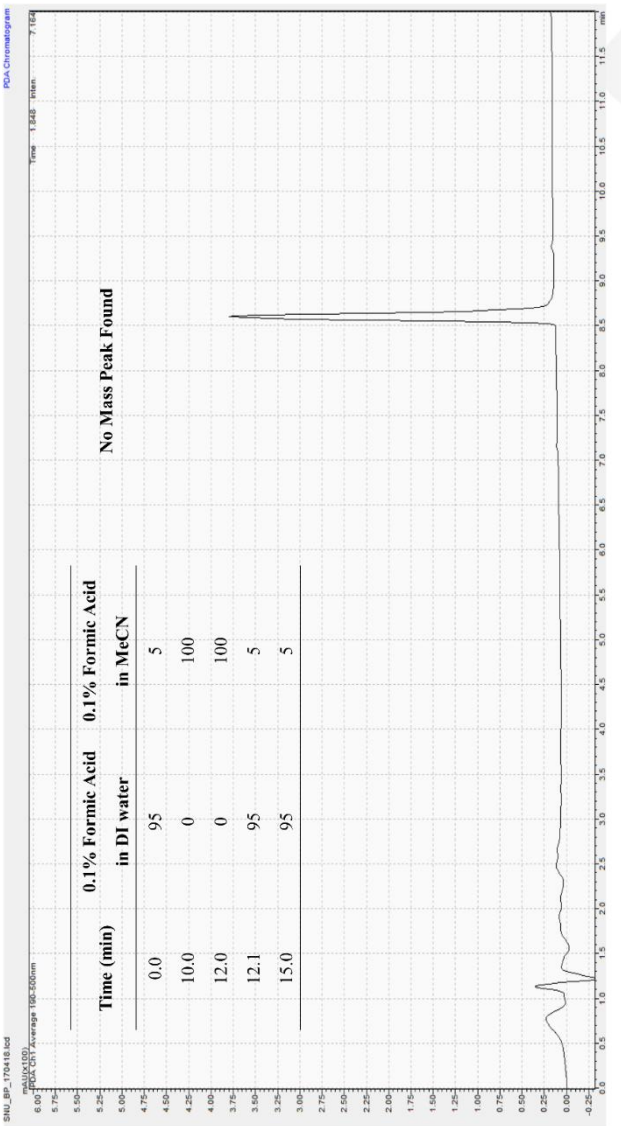

Fig. 2-56 The raw data of LC-MS of BP. No mass peak found due to no ionization by APCI.

The standard compounds of products are organized below.

Anthraquinone (**2a**): Purchased from Sigma Aldirch (97%) and used as received to compare the product mixture as standard. ^{1}H−NMR (300 MHz, $CDCl_3$): δ 8.30 (dd, J = 5.7, 3.3 Hz, 4H), 7.79 (dd, J = 5.7, 3.3 Hz, 4H). LC−MS (APCI): calcd. for $C_{14}H_9O_2$ $[M+H]^+$ 209; found 209.1.

The raw data of ^{1}H−NMR (Fig. 2−57) and LC−MS (Fig. 2−58) are attached for **2a**.

2−Methylanthraquinone (**2b**): Purchased from TCI (99%) and used as received. ^{1}H−NMR (300 MHz, $CDCl_3$): δ 8.28 (m, 2H), 8.18 (d, J = 8.1 Hz, 1H), 7.76 (m, 2H), 7.57 (dd, J = 7.8, 0.9 Hz, 1H). LC−MS (APCI): calcd. for $C_{15}H_{11}O_2$ $[M+H]^+$ 223; found 223.1.

The raw data of ^{1}H−NMR (Fig. 2−59) is attached for **2b**.

9−Anthracenecarboxaldehyde (**2c**): Purchased from Sigma Aldrich (97%) and used as received. ^{1}H−NMR (300 MHz, $CDCl_3$): δ 11.49 (s, 1H), 8.95 (d, J = 9.0 Hz, 2H), 8.64 (s, 1H), 8.02 (d, J = 8.4 Hz, 2H), 7.66 (ddd, J = 8.7, 6.6, 1.2 Hz, 2H), 7.52 (m, 2H). LC−MS (APCI): calcd. for $C_{15}H_{11}O$ $[M+H]^+$ 207; found 207.1.

The raw data of ^{1}H−NMR (Fig. 2−60) and LC−MS (Fig. 2−61) is attached for **2c**.

9,10−Anthracenediol: Purchased from Ark Pharm. Inc. (98%) and used as received to compare the **2a**. ^{1}H−NMR (300 MHz, $CDCl_3$): δ 8.31 (dd, J = 5.7, 3.3 Hz, 4H), 7.79 (dd, J = 5.7, 3.3 Hz, 4H). LC−MS (APCI): calcd. for $C_{14}H_{11}O_2$ $[M+H]^+$ 211; found 209.1, matched to $C_{14}H_9O_2$.

The raw data of ^{1}H−NMR (Fig. 2−24) and LC−MS (Fig. 2−25) are previously attached. In addition, note that 9,10−anthracenediol is found to be identical to anthraquinone (AQ, **2a**) in both ^{1}H−NMR and LC−MS spectra.

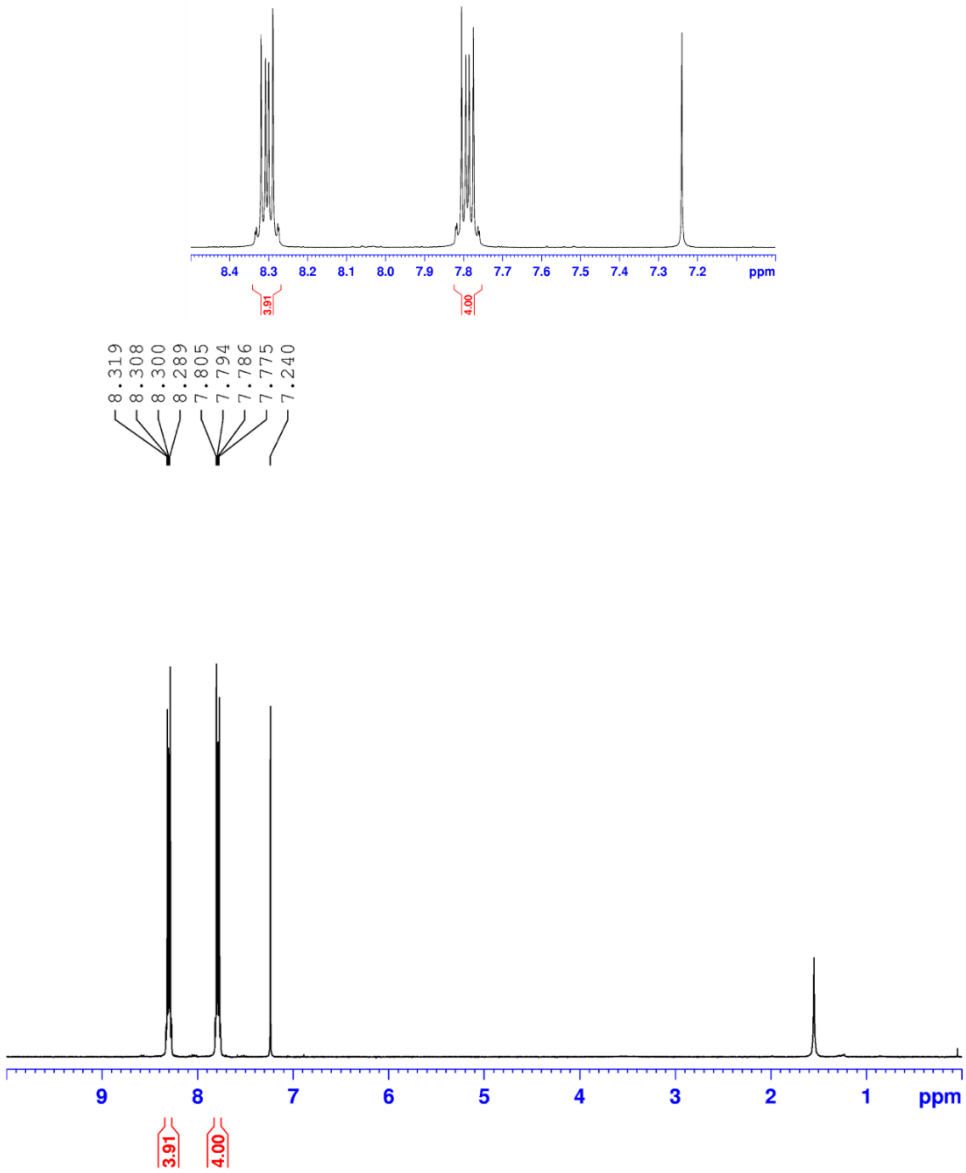

Fig. 2-57 The raw data of ^{1}H-NMR of 4a.

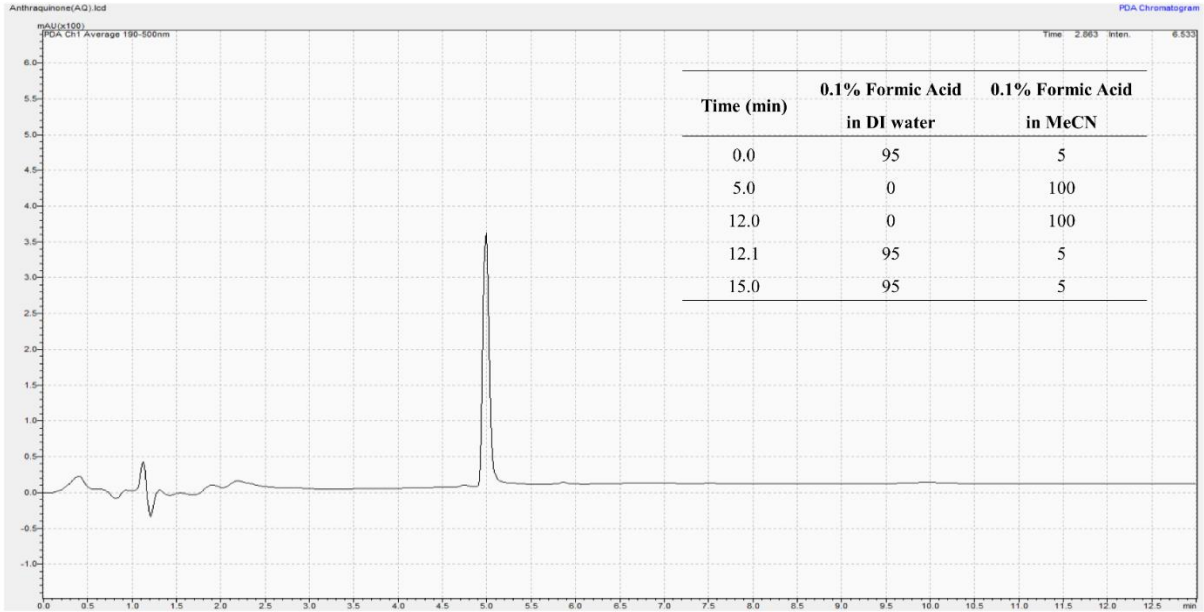

Time (min)	0.1% Formic Acid in DI water	0.1% Formic Acid in MeCN
0.0	95	5
5.0	0	100
12.0	0	100
12.1	95	5
15.0	95	5

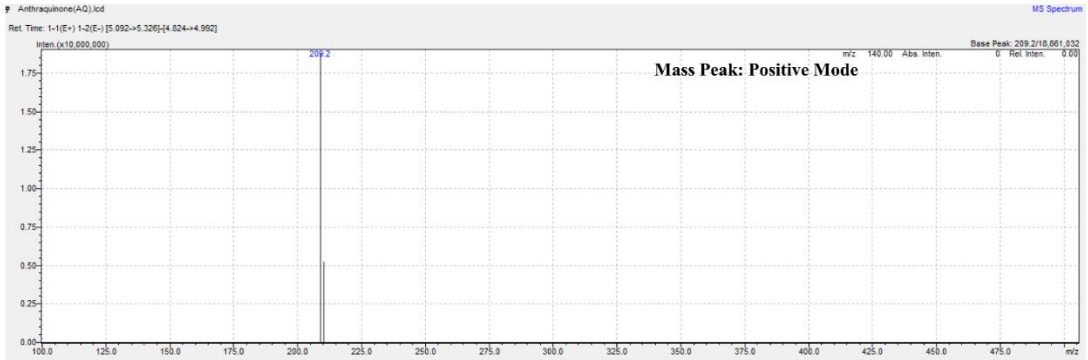

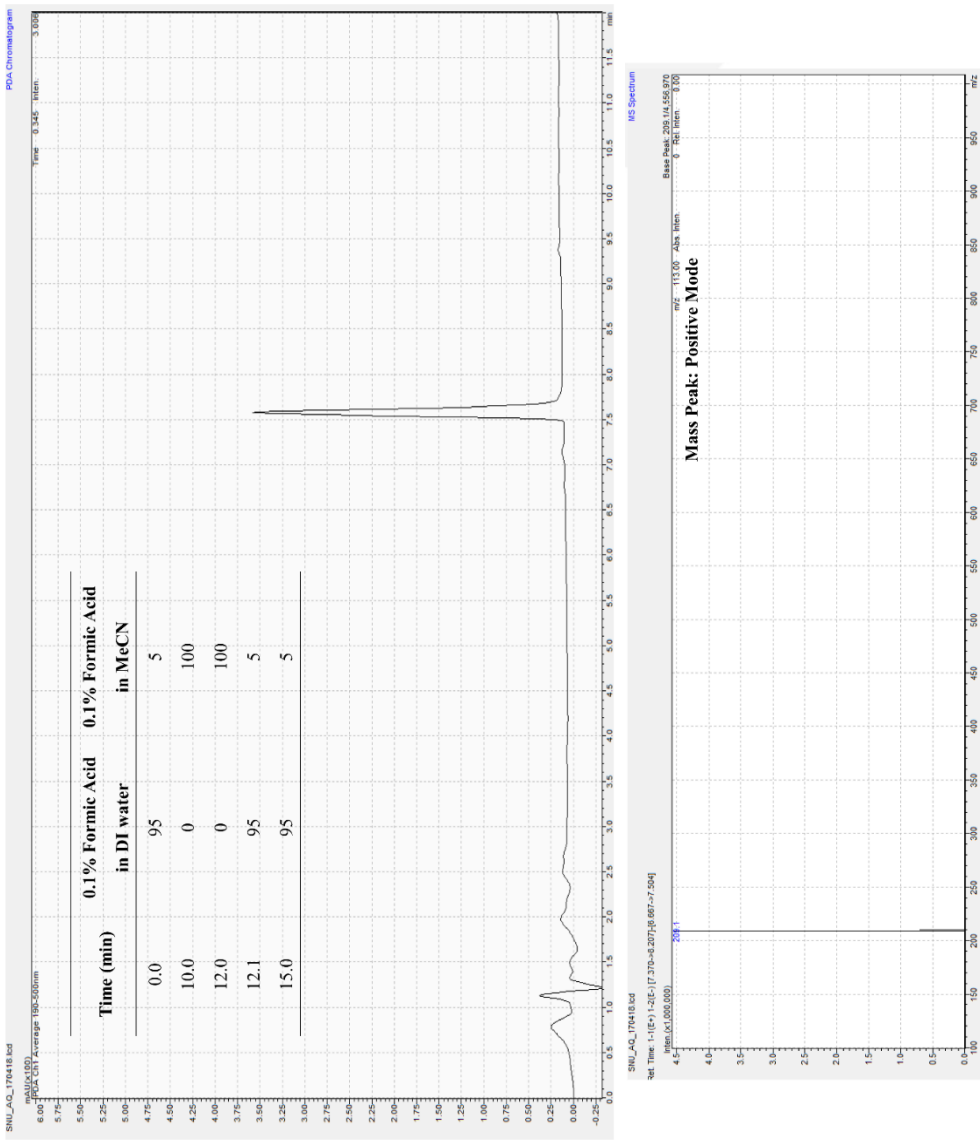

Fig. 2-58 The raw data of LC-MS of **4a**. Two spectra are measured in different eluent condition.

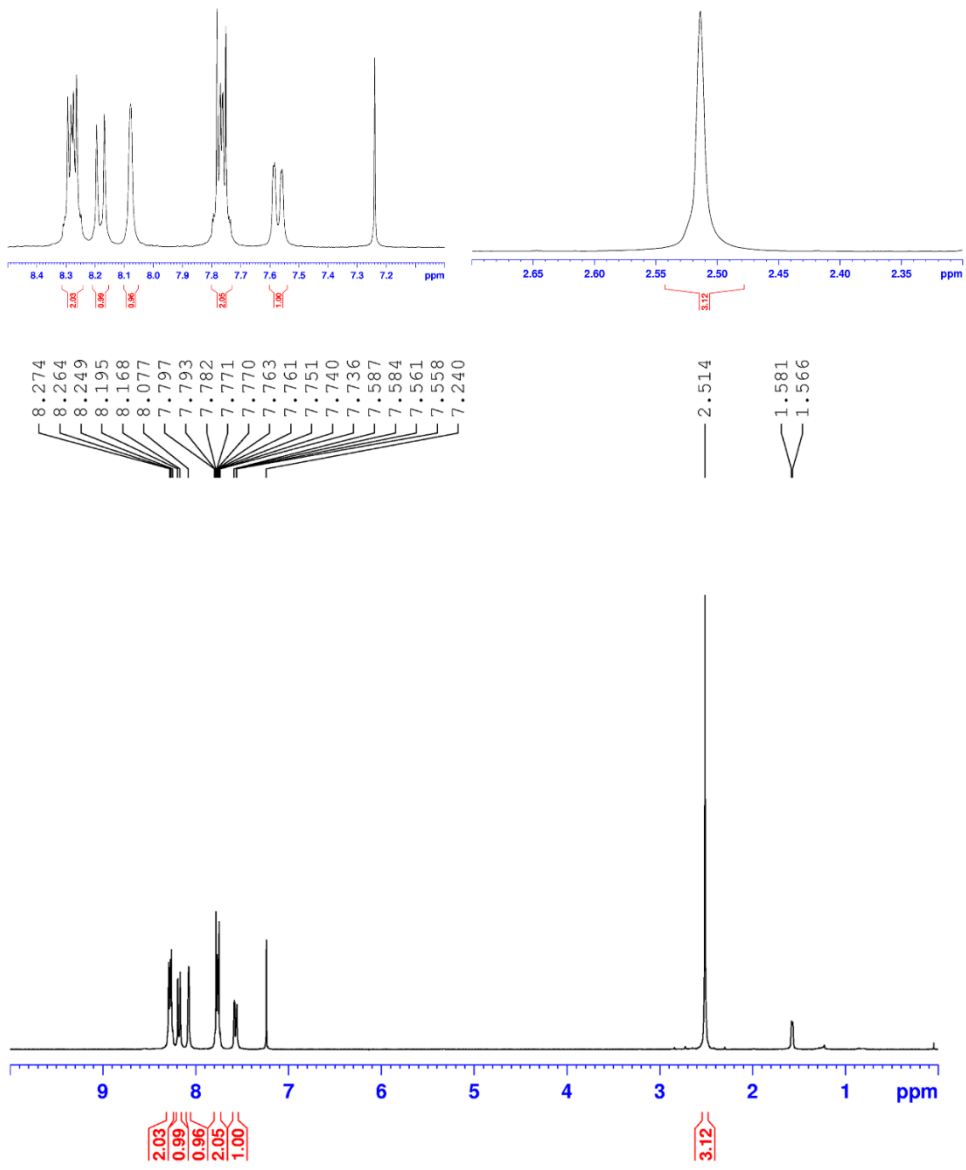

Fig. 2-59 The raw data of ^{1}H-NMR of 2b.

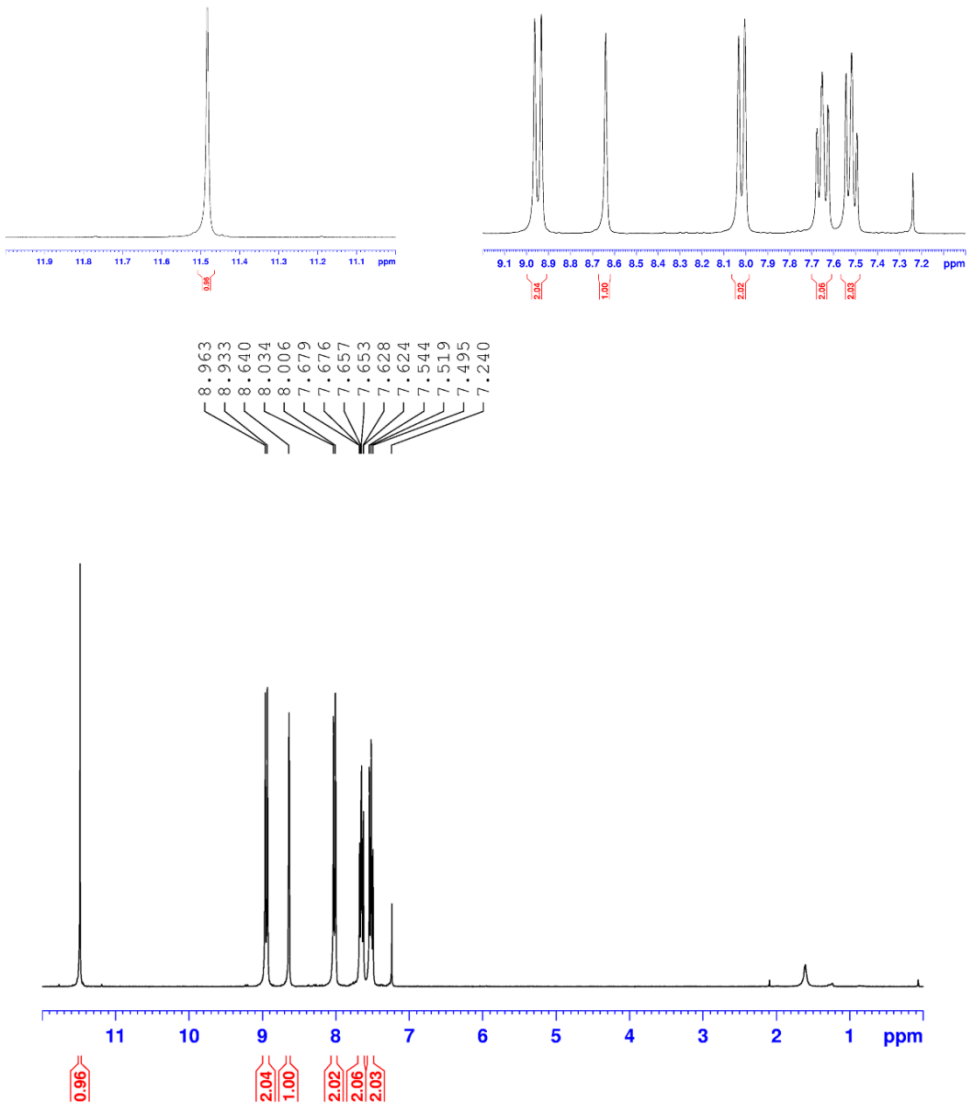

Fig. 2-60 The raw data of ^{1}H-NMR of 2c.

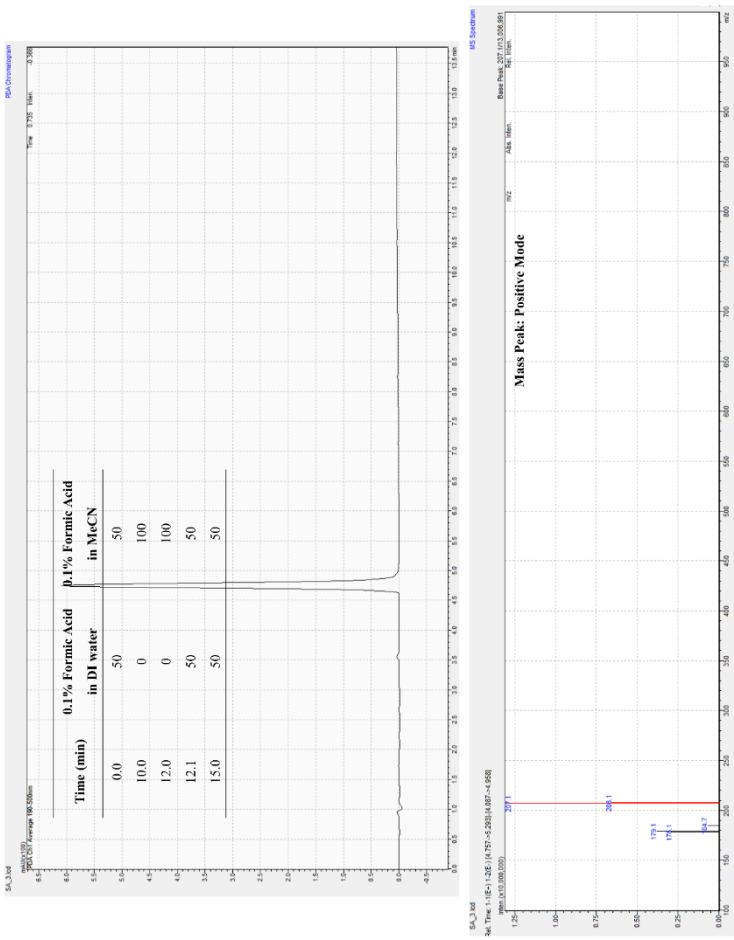

Fig. 2-61 The raw data of LC-MS of 2c.

2.4 Conclusion

In summary, a defective n^+−Si/SiO_2 electrode was fabricated and the cathodic electroorganic reactions on such EOS system were investigated. The dielectric electrode showed similar electrochemical behavior to the 6−nm−thick thermal SiO_2 reported previously. Negative bias in acidic organic media produces low faradaic current which depends only on proton concentration of the solution. The existence of redox couples which follows the outer−sphere electron transfer mechanism barely contributes to current density. The electrolysis at “cathodic” potential showed that cathodic current yields both the “oxidized” and “reduced” product. Particularly, ANTH and its derivatives are electrochemically oxidized as a consequence of cathodic reaction at the defective n^+−Si/SiO_2 electrode. According to the analysis of electrodes and products of electrolysis, the observed event must involve electrochemically generated species. This is suggested to be a hydrogen atom produced by the reduction of protons at the dielectric electrode. Various experiments were performed to provide evidence which supports the proposed reaction mechanism. These results clearly indicate significant discoveries. The mechanism for the cathodic electroorganic reaction was proposed with the experimental evidence in this study although it is yet to require further research. Even so, this system will inspire many ideas in EOS and as well in electrolyte−oxide−metal (EOM)

system. This could be a new synthetic strategy in the field of synthetic organic chemistry

2.5 References

[1] T. Morofuji, A. Shimizu, J. Yoshida, *J. Am. Chem. Soc.*, 2015, *137*, 9816.

[2] S. R. Waldvogel, S. Mohle, *Angew. Chem. Int. Ed.*, 2015, *54*, 6398.

[3] E. J. Horn, B. R. Rosen, Y. Chen, J. Tang, K. Chen, M. D. Eastgate, P. S. Baran, *Nature*, 2016, *533*, 77.

[4] Y. Kawamata, M. Yan, Z. Liu, D. H. Bao, J. Chen, J. T. Starr, P. S; Baran, *J. Am. Chem. Soc.*, 2017, *139*, 7448.

[5] M. Yan, Y. Kawamata, P. S. Baran, *Chem. Rev.*, 2017, *117*, 13230.

[6] K. J. Frankowski, R. Liu, G. L. Milligan, K. D. Moeller, J. Aube, *Angew. Chem. Int. Ed.*, 2015, *54*, 10555.

[7] F. Tang, K. D. Moeller, *J. Am. Chem. Soc.*, 2007, *129*, 12414.

[8] A. Kirste, G. Schnakenburg, F. Stecker, A. Fischer, S. R. Waldvogel, *Angew. Chem. Int. Ed.*, 2010, *49*, 971.

[9] T. Morofuji, A. Shimizu, J. Yoshida, *Angew. Chem. Int. Ed.*, 2012, *51*, 7259.

[10] A. Wiebe, B. Riehl, S. Lips, R. Franke, S. R. Waldvogel, Sci. Adv. 2017, *3*, 10.

[11] J. Chen, W. Q. Yan, C. M. Lam, C. C. Zeng, L. M. Hu, R. D. Little, *Org. Lett.*, 2015, *17*, 986.

[12] C. Y. Liu, A. J. Bard, *Nat. Mater.*, 2008, *7*, 505.

[13] C. Y. Liu, A. J. Bard, *J. Am. Chem. Soc.*, 2009, *131*, 6397.

[14] J. Velmurugan, D. P. Zhan, M. V. Mirkin, *Nat. Chem.*, 2010, *2*,

498.

[15] H. T. Baytekin, A. Z. Patashinski, M. Branicki, B. Baytekin, S. Soh, B. A. Grzybowski, *Science*, 2011, *333*, 308.

[16] J. Y. Lee, J. G. Lee, S. H. Lee, S. M. Seo, L. Piao, J. H. Bae, S. Y. Lim, Y. J. Park, T. D. Chung, *Nat. Commun.*, 2013, *4*, 2766.

[17] H. T. Baytekin, B. Baytekin, S.; Huda, Z. Yavuz, B. A. Grzybowski, *J. Am. Chem. Soc.*, 2015, *137*, 1726.

[18] J. G. Lee, J. −Y. Lee, J. Yun, Y. Lee, S. Lee, S. J. Shin, J. H. Bae, T. D. Chung, *Electrochem. Commun.*, 2017, *76*, 75.

[19] J. Y. Lee, S. J. Shin, J. G. Lee, J. Yun, M. A. Oh, T. D. Chung, *J. Electrochem. Soc.*, 2017, *164*, D1.

[20] C. Yun, S. H. Lee, J. Ryu, K. Park, J. W. Jang, J. Kwak, S. Hwang, *J. Am. Chem. Soc.*, 2018, *140*, 14687.

[21] D. P. Manica, Y. Mitsumori, A. G. Ewing, *Anal. Chem.*, 2003, *75*, 4572.

[22] M. Mossad, L. Zou, *J. Hazard. Mater.*, 2013, *244*, 387.

[23] C. Kohler, L. Bleck, M. Frei, R. Zengerle, S. Kerzenmacher, *Chemelectrochem*, 2015, *2*, 1785.

[24] Y. F. Zhai, O. Baturina, D. Rarnaker, E. Farquhar, J. St−Pierre, K. Swider−Lyons, *J. Phys. Chem. C*, 2015, *119*, 20328.

[25] E. Peltola, S. Sainio, K. B. Holt, T. Palomaki, J. Koskinen, T. Laurila, *Anal. Chem.*, 2018, 90, 1408.

[26] D. D. M. Wayner & V. D. Parker, V. D. *Acc. Chem. Res.,* 1993, *26*, 287.

[27] B. D. McCarthy, D. J. Martin, E. S. Rountree, A. C. Ullman, J. L. Dempsey, *Inorg. Chem.*, 2014, *53*, 8350.

[28] H. I. Abdel-Shafy, H. E. Sayour, M. S. M. Mansour, *Polym. Advan. Technol.*, 2016, *27*, 724.

[29] F. Z. Mesbaiah, F. Mansour, K. Eddouaouda, A. Badis, *Desalin. Water Treat.*, 2016, *57*, 5995.

[30] I. Tongo, L. Ezemonye, K. Akpeh, *Environ. Monit. Assess.*, 2017, *189*, 247.

[31] I. Tongo, O. Ogbeide, L. Ezemonye, *Toxicol. Rep.*, 2017, *4*, 55.

[32] C. Sanchez-Sanchez, J. I. Martinez, N. Ruiz Del Arbol, P. Ruffieux, R. Fasel, M. F. Lopez, P. L. de Andres, J. A. Martin-Gago, *J. Am. Chem. Soc.*, 2019, *141*, 3550.

[33] A. Yokozawa, Y. Miyamoto, *Phys. Rev. B*, 1997, *55*, 13783.

[34] I. A. Shkrob, B. M. Tadjikov, S. D. Chemerisov, A. D. Trifunac, *J. Chem. Phys.*, 1999, *111*, 5124.

[35] C. Barckholtz, T. A. Barckholtz, C. M. Hadad, *J. Am. Chem. Soc.*, 1999, *121*, 491.

[36] E. C. Gentry, R. R. Knowles, *Acc. Chem. Res.*, 2016, *49*, 1546.

[37] S. Ghosh, J. Castillo-Lora, A. V. Soudackov, J. M. Mayer, S. Hammes-Schiffer, *Nano Lett.*, 2017, *17*, 5762.

[38] W. D. Morris, J. M. Mayer, *J. Am. Chem. Soc.*, 2017, *139*, 10312.

[39] J. M. Campos-Martin, G. Blanco-Brieva, F. L. G. Fierro, *Angew. Chem. Int. Ed.*, 2006, *45*, 6962.

[40] D. D. M. Wayner, V. D. Parker, *Acc. Chem. Res.*, 1993, *26*, 287.

[41] H. A. Schwarz, *J. Chem. Educ.*, 1981, *58*, 101.

[42] G. V. Buxton, C. L. Greenstock, W. P. Helman, A. B. Ross, *J. Phys. Chem. Ref. Data*, 1988, *17*, 513.

[43] X. Q. Hu, X. T. Qi, J. R. Chen, Q. Q. Zhao, Q. Wei, Y. Lan, W. J. Xiao, *Nat. Commun.*, 2016, *7*, 11188.

[44] B. Quiclet-Sire, S. Z. Zard, *Proc. Math. Phys. Eng. Sci.*, 2017, *473*, 20160859.

[45] K. Beckmann, H. Uchtenhagen, G. Berggren, M. F. Anderlund, A. Thapper, J. Messinger, S. Styring, P. Kurz, *Energy Environ. Sci.*, 2008, *1*, 668.

[46] P. S. Rao, E. Hayon, *J. Phys. Chem.*, 1975, *79*, 397.

[47] I. M. AlNashef, M. L. Leonard, M. C. Kittle, M. A. Matthews, J. W. Weidner, *Electrochem. Solid. St.*, 2001, *4*, D16-D18.

[48] A. P. S. Bailey, Ozonation in Organic Chemistry V2: Nonolefinic Compounds. 1 ed., Elsvier, 1982.

[49] N. Toshima, T. Sugano, H. Hirai, *Can. J. Chem.,* 1984, *62*, 2053.

3. Direct Electrodeposition of Thin Metal Films on Functionalized Dielectric Layer and Hydrogen Gas Sensor

3.1 Introduction

The deposition of nanostructured metal on dielectric layers is important in an industry such as solid state electronics [1], catalysts supported on substrate for energy conversion devices [2], sensors [3], etc. There are many conventional methods to prepare metal films on dielectric such as atomic layer deposition (ALD) [4], sputtering in vacuum [5], galvanic replacement [6,7], or electroless deposition via reducing agents [8], etc. Electrochemical methods [9,10] provide a simple and fine solution process without using reducing agents via direct electron transfer to the precursors. Important of all, surfactant-free NPs or films can be created on a surface that serves as the potential catalytic active sites for various chemical reactions and sensors [11]. Therefore, the electrochemical method has been widely renowned as an economically-efficient alternative method. In particular, electrosynthesis of nanoparticles on conducting substrates [12,13] has attracted great attention as to control the shape of nanoparticles by the programmed electrochemical methods

on substrate of glassy carbon [14]. Despite its valuable advantages, the produced nanoparticles by programmed electrosynthesis must be transferred to other substrates. The candidate substrates, in general, are mostly insulator materials to pose practical in many application areas.

The recently reported method provides an intuitive idea to overcome these issues in terms of direct electrodeposition on dielectric layers; Pd NPs electrodeposited on n^+−Si/thermal SiO_2 [15]. Direct electroplating on insulating substrates is out of common sense. However, the electrogenerated hydrogen atoms in the thermal SiO_2 layer makes this possible. The hydrogen atom mediated electrochemistry at SiO_2 finely controls the electroreduction not only by the pH in the solution but also by the applied voltage. Thus, it can produce pristine Pd NPs deposited on SiO_2 without any surfactant. Hydrogen atoms, generated by reduction of protons migrated along with SiO_2 layers, are a strong reducing agent as described in the early chapters. Undoubtedly, they are expected to electrochemically reduce the precursors at the interface of thermal SiO_2 and the solution. Indeed, this provides a new innovation to directly electroplating technology of thin metal films on a dielectric layer.

There are some critical matters to overcome in order to utilize such chemistry. An inherently low current density mediated by hydrogen atoms and weak affinity between metal and pristine SiO_2 surface is unlikely to produce a significant amount of metals on the surface. In

addition, there is a disadvantage in the uniformity of shape and size of the particles. Nevertheless, it is unfavorable to apply large overvoltage to increase current density for fine, steady control of the electroplating. However, the electrochemistry through n^+−Si/SiO_2 inherently possesses strong negative onset potential compared to the reduction potentials of many metals. Moreover, high current density is needed to acquire electrodeposited metal film in reasonable time.

In this chapter, direct electrodeposition of 100 nm−thick metal films on dielectric layers is demonstrated. The appropriate SiO_2 surface modification was performed to accomplish both fair affinity of metal on the surface and fine control of current density by hydrogen atoms. Many kinds of metals such as Pd, Pt, Cu, or Ni, can be directly electrodeposited on the SiO_2 surface functionalized with Au NPs (denote as n^+−Si/SiO_2−NH_2−AuNP). Its surface allows uniformly distributed Pd NPs of 100 nm−thick films. As an application, Pd metal thin film on n^+−Si/SiO_2−NH_2−AuNP is demonstrated to work as a hydrogen gas sensor which needs a sufficiently large amount of Pd thin film.

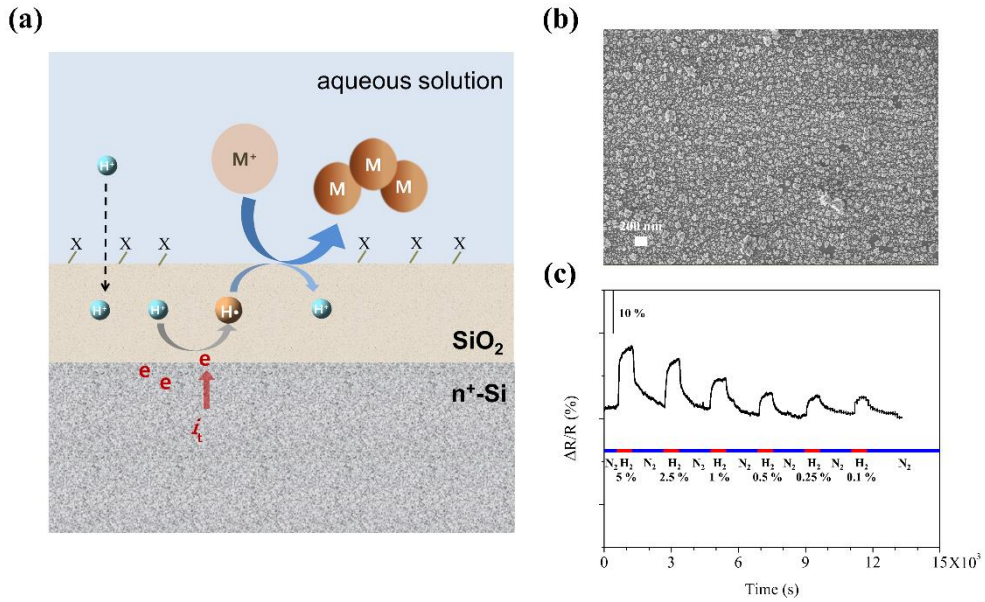

Fig. 3-1 (a) Schematic illustration of the direct electrodeposition on various modified surface of n^+-Si/SiO_2 dielectric electrode. (b) Representative image of directly electrodeposited thin film of metal NPs on n^+-Si/SiO_2 dielectric electrode. (c) Hydrogen gas sensing behavior of the fabricated sensor based on the electrodeposited thin film of Pd NPs on n^+-Si/SiO_2 dielectric electrode.

3.2 Experimental Methods

3.2.1 Materials and reagents

Palladium (II) chloride ($PdCl_2$, ≥ 99.9%), potassium gold (III) chloride ($KAuCl_4$, 98%), chloroplatinic acid hydrate ($H_2PtCl_6 \cdot xH_2O$, ≥ 99.9% trace metal basis), and (3-aminopropyl)triethoxysilane (APTES) were purchased from Sigma Aldrich. Copper sulfate ($CuSO_4$) was a product of Junsei Chemicals Co., Ltd. Nickel sulfate hexahydrate ($NiSO_4 \cdot 6H_2O$, ≥ 98.5%) was purchased from Dae Jung. All chemicals were used without further purification.

3.2.2 Preparation of thermal SiO_2 on n^+-Si wafer

N-type, arsenic-doped, <100> oriented Si wafers (n^+-Si) with resistivity of 0.005 Ω cm were purchased from STC (Japan). n^+-Si with thermal oxide SiO_2 (n^+-Si/SiO_2) was produced by dry oxidation under the dry oxygen environment. Prior to oxidation, conventional RCA cleaning was done. The sacrificial 200-Å-thick thermal oxide was prepared at 850 ° C then stripped again by diluted HF. Cleaning was repeated, and the target 6-nm-thickness was achieved at 850 ° C in a furnace by blowing dry O_2. The insulating property of the prepared 6-nm-thick thermal SiO_2 was checked by the current density-voltage voltammogram in metal-oxide-silicon (MOS)

system. The threshold field of the prepared thermal SiO_2 is 10^7 V/cm, confirming oxide insulators were well-prepared.

3.2.3 Surface modification of the prepared thermal SiO_2 with amine and Au NPs

Previously prepared 6 nm n^+-Si/ SiO_2 was degreased by sonication in acetone and isopropanol and rinsed with methanol. It was immediately immersed in 2 wt% APTES solution in ethanol for 1 h. Then it was washed with ethanol and baked in the oven at 120 ° C for 30 min. The NH_2-terminated surface of SiO_2 was confirmed by XPS.

The sample of NH_2-terminated SiO_2 on n^+-Si was immersed in an aqueous solution that contained colloidal Au NPs for 3 h. Then it was rinsed with D. I. water and dried with N_2 gas.

The Au NPs used for functionalization were prepared as follows. 0.5 mL of 1 M sodium hydroxide and 1 mL of THPC (Tetrakis(hydroxymethyl) phosphonium chloride) solution (prepared by adding 12 μL of 80 % THPC (0.067 mmol) in water to 1 mL water) was diluted by adding 45 mL water. The reaction mixture was stirred for 5 min by a vortex mixer. Then, 2.0 mL (27 mmol) of 1 % $HAuCl_4$ in water was added quickly, stirring for 5 min. A brown solution was obtained and stored in a refrigerator at 4 ° C when not used immediately.

3.2.4 Electrochemical synthesis of NPs on amine-modified SiO_2

The deposition of metal NPs on n^+-Si/SiO_2 (6 nm thick) was performed in a conventional three-electrode cell with an Ag/AgCl electrode (3 M NaCl, BAS Inc.) and Pt wire (diameter of 0.5 mm) as the reference and counter electrodes, respectively. All potentials refer to the Ag/AgCl reference electrode. The bimetallic NPs and NCs were electrochemically synthesized in an N_2 environment immediately after purging the solution with N_2 gas for 10 min at room temperature.

To deposit Pd NPs, an aqueous solution composed of 0.5 mM $PdCl_2$ in 0.1 M potassium phosphate buffer of pH 3 was prepared and a constant potential of −1.2 V or −1.5 V (vs. Ag/AgCl) was applied to the n^+-Si/SiO_2.

3.2.5 Electrochemical synthesis of AuNP-based bimetallic NPs

The substrates of Au-NPs dispersed SiO_2 were exposed to the aqueous electrolyte with metal precursors, i.e. 0.5 mM $PdCl_2$, 1 mM $CuSO_4$, and 1 mM H_2PtCl_6 in 0.1 M potassium phosphate buffer at pH 3, respectively. For Ni, 1 mM $NiSO_4$ in boric acid aqueous solution at pH 3.8 was used. Bimetallic NPs on n^+-Si/SiO_2 (6 nm thick) were

electrodeposited in a conventional three-electrode cell with an Ag/AgCl electrode (3 M NaCl, BAS Inc.) and Pt wire (diameter of 0.5 mm) for reference and counter electrodes.

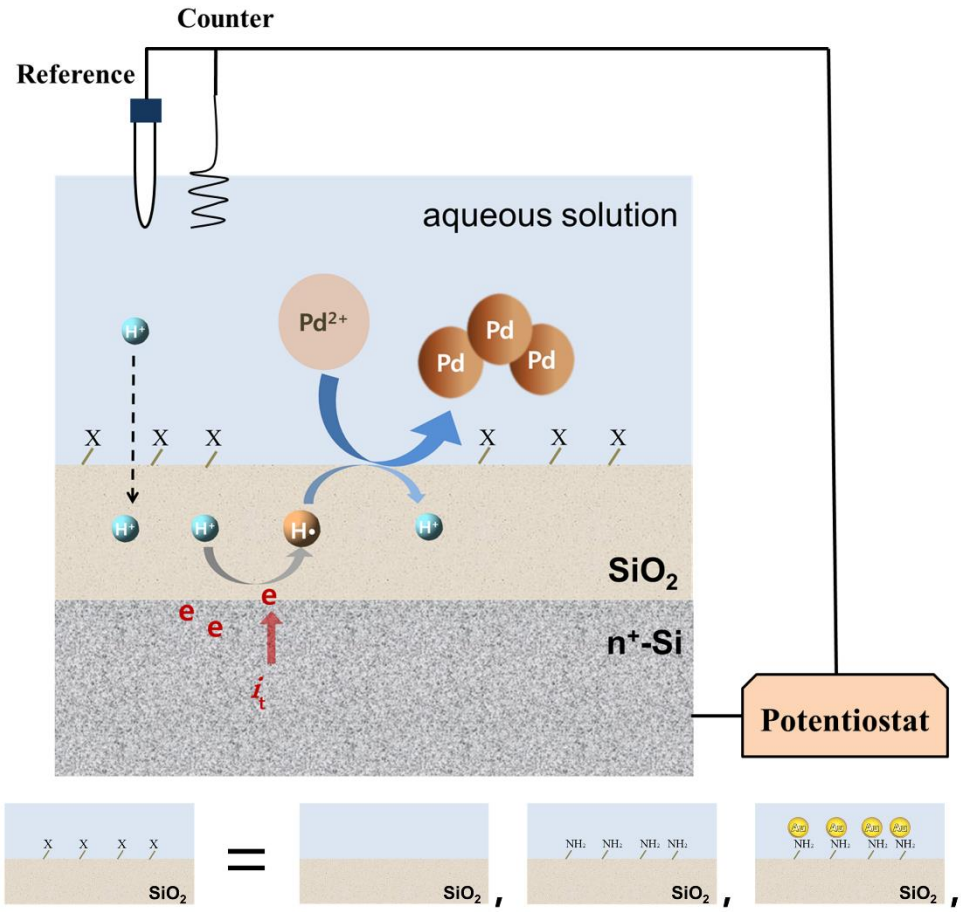

Fig. 3-2 Schematic illustration of the metal electrodeposition directly by hydrogen atom mediated electrochemistry on chemically modified of n^+-Si/SiO_2 surfaces.

3.2.6 Characterization of NPs

The NPs on SiO_2 were characterized by field-emission scanning electron microscopy (FE-SEM, Carl Zeiss, Germany), focused ion beam (FIB, Carl Zeiss, Germany) and energy-dispersive spectroscopy (EDS; Carl Zeiss, Germany) at the National Instrumentation Centre for Environmental Management (NICEM) of Seoul National University. X-ray photoelectron spectroscopy (XPS, AXIS-HIS: KRATOS) was used at the Research Institute of Advanced Materials of Seoul National University. We completely digested the electroplated Pd in aqua regia and diluted with DI water to quantify its amount by ICP-AES (Perkin-Elmer Optima 4300 DV, SNU AMS Facility NCIRF).

3.2.7 Hydrogen gas sensing

Pd NPs for H_2 sensor was fabricated as follows. Pd was directly electroplated on n^+-Si/SiO_2-NH_2-AuNP at -1.5 V (vs. Ag/AgCl) in 0.5 mM $PdCl_2$ of 0.1 M potassium phosphate buffer at pH 3. Putting two Cu tapes between an approximately 1 mm gap, we tested the Pd-deposited n^+-Si/SiO_2-NH_2-AuNP for H_2 sensing. Two adhered Cu tapes were electrically connected with a potentiostat. We let H_2 and N_2 gas alternatively flow into the quartz tube furnace (tube dimension: 5 cm diameter with 75 cm length) linked to a gas flowmeter. The partial pressure of H_2 was controlled by adjusting the ratio of flow

rates of 99.999% H_2 and 99.9% N_2 where the total gas flow rate was fixed to 1000 sccm. The applied bias was typically 2 mV (otherwise mentioned).

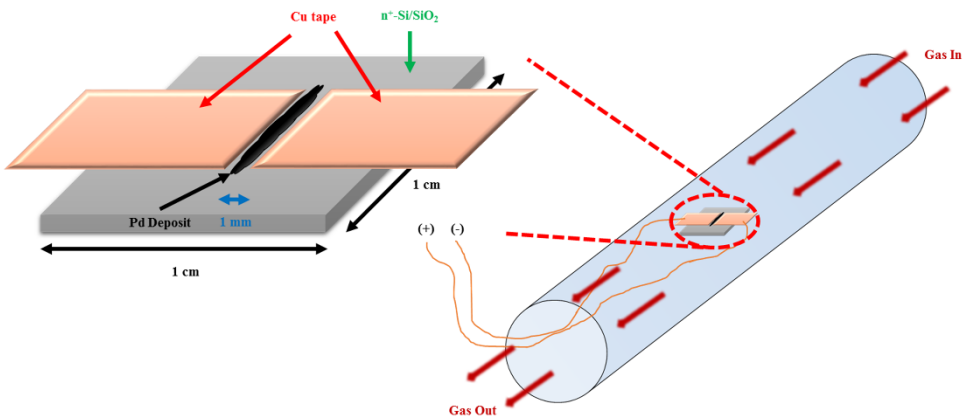

Fig. 3-3 Schematic diagram of the fabrication of hydrogen gas sensor and measurement of its gas sensing property upon applied bias.

3.3 Results and Discussion

3.3.1 The direct electrodeposition of various metal NPs on modified surface of n^+−Si/SiO_2

By hydrogen atom mediated electrochemistry within SiO_2 layer, direct Pd electrodeposition on n^+−Si/SiO_2 was demonstrated which was confirmed to be an electrical insulator [15]. Other metals such as Au, Cu, and Pt, however, barely can be electrodeposited since most of them weakly adhere to SiO_2 unless Pd NPs pre−exist on it [15]. Although Pd NPs pre−exists, the deposition process is slow due to the low current density that only small amounts of metals even performing electroplating for a long time. Moreover, electrodeposited Pd NPs were not finely controlled in terms of size, shape, and dispersity.

In short, it was impossible to obtain the desired thin metal films on the pristine thermal SiO_2 surface by direct electrodeposition. In order to directly electroplate many other metals on SiO_2 in large amounts, adhesive layer is needed. It must sufficiently increase the affinity between pristine SiO_2 and metal electrodeposit. The thin layers of Cr or Ti are common material to increase the adhesion in semiconductor industry. However, they are not suitable in the electrochemical system since it can block the electron transfer mediated by hydrogen atom from the electrode to the solution. An aliphatic primary amine

may be a promising organic compound to anchor metal NPs onto the SiO_2 [16]. In this work, thermally grown 6 nm n^+-Si/SiO_2 functionalized with APTES to form the more adhesive surface of primary amine terminal. However, n^+-Si/SiO_2-NH_2 was not sufficient enough to increase the affinity of the surface in order to immobilize reproducibly. In addition to amine groups, 2-3 nm Au NPs were introduced by immersing n^+-Si/SiO_2-NH_2 in the Au NPs dispersed in the aqueous solution.

Figure 3-4 shows the distribution and morphology of the electrodeposited Pd NPs upon various surface modification on the SiO_2 surface. Pd NPs on $n^+-SiO_2-NH_2$ are spread more uniformly than on the pristine surface of SiO_2. However, the quantitative analysis (Table 3-1) indicates that $n^+-SiO_2-NH_2$ does not sufficiently anchor the metal which were electrochemically reduced. It is believed that amine groups improve affinity while also causes an attendant adverse effect.

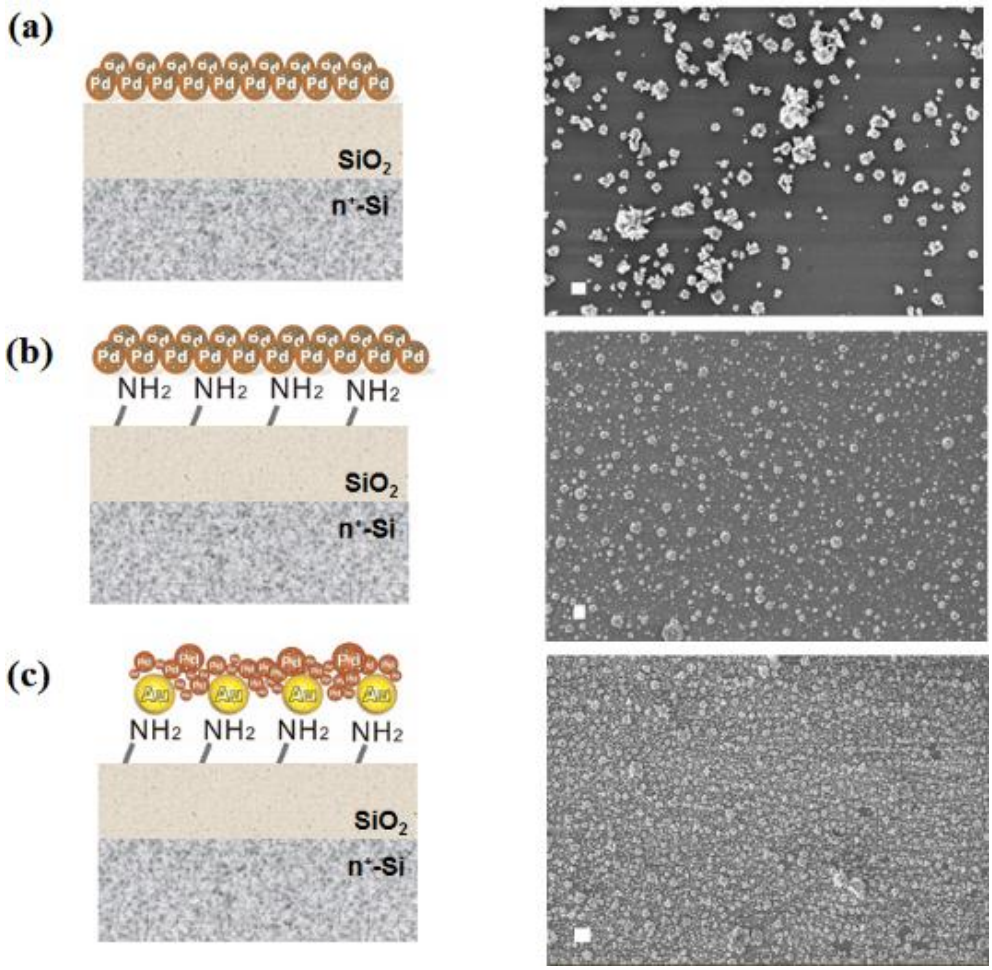

Fig. 3-4 Electrodeposited Pd on various surface of modified n^+-Si/SiO_2 electrode. The experimental condition for electrodeposition was N_2-purged solution of 0.5 mM $PdCl_2$ and 0.1 M potassium phosphate (pH 3) applying -1.5 V for 30 min (a) on pristine SiO_2, (b) n^+-Si/SiO_2-NH_2, and (c) n^+-Si/SiO_2-NH_2-AuNP. Scale bars are 100 nm, 200 nm and 200 nm respectively from (a) to (c).

Substrate	Pd Amount ($\mu g \cdot cm^{-2}$)	Pd/Charge ($\mu g \cdot C^{-1} \cdot cm^{-2}$)	Faraday Efficiency (%)
n^+-Si/SiO_2	9.35	98	8.9
n^+-Si/SiO_2-NH_2	5.64	89	8.1
n^+-Si/SiO_2-NH_2-AuNP	12.24	172	15.7

Table 3-1 Quantitative analysis of Pd electrodeposit on various surfaces of SiO_2. The amount of Pd deposited was determined by ICP-AES measurement and charge from $i-t$ curve, respectively.

The organic film on the n^+-Si/SiO_2-NH_2 resembles an insulator that hinders the electron transfer mediated by hydrogen atoms. Supported by the experimental result (Table 3-1), the faraday efficiencies are similar in n^+-Si/SiO_2 and n^+-Si/SiO_2-NH_2 but the electrodeposited Pd amount is less on amine-modified SiO_2 surface. Thus, the functionalization of aliphatic amine groups on the SiO_2 layer surface is not enough to increase the quantity of Pd electrodeposit.

Outstandingly, Au NPs on the amine-functionalized SiO_2 surface significantly enhance both the homogeneity distribution and thickness of Pd electrodeposit as shown in Fig. 3-5. The uniform, large area of metal film is about 100 nm thick. This is the first thin metal film to report which is directly electrodeposited on a dielectric layer via hydrogen atom mediated electrochemistry [15]. Furthermore, other metals such as platinum, copper, and nickel could be electrodeposited on n^+-Si/SiO_2-NH_2-AuNP as well. The SEM images of these electrodeposited metals are shown in Fig. 3-6. In addition, the elements are confirmed by XPS or EDS for Pt (Fig. 3-7), Cu (Fig. 3-8), and Ni (Fig. 3-9), respectively. In this study, Au NPs of 3-5

nm diameters were uniformly distributed on n^+-Si/SiO_2-NH_2 surface and acted as the seeds for uniform nucleation and growth into a greater amount of metal electrodeposition.

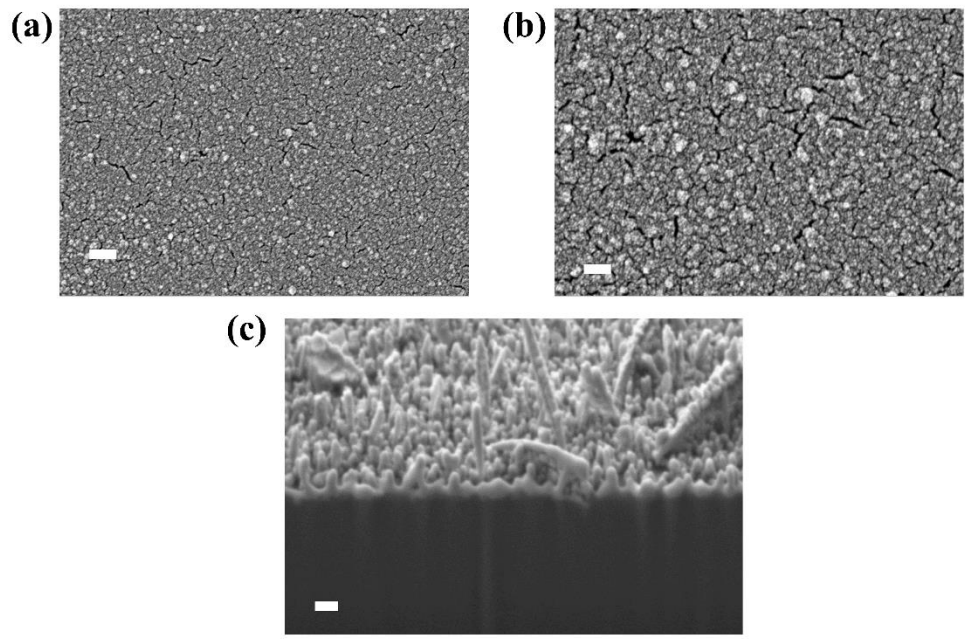

Fig. 3-5 Pd film on n^+-Si/SiO_2-NH_2-AuNP. Pd was electrodeposited by applying −0.9 V (vs. Ag/AgCl) for 30 min on n^+-Si/SiO_2-AuNP. (a) FE-SEM image of the surface. (b) Magnified view of (a). (c) Cross-sectional view after FIB dissection. Scale bars are 200 nm, 100 nm and 100 nm respectively from (a) to (c).

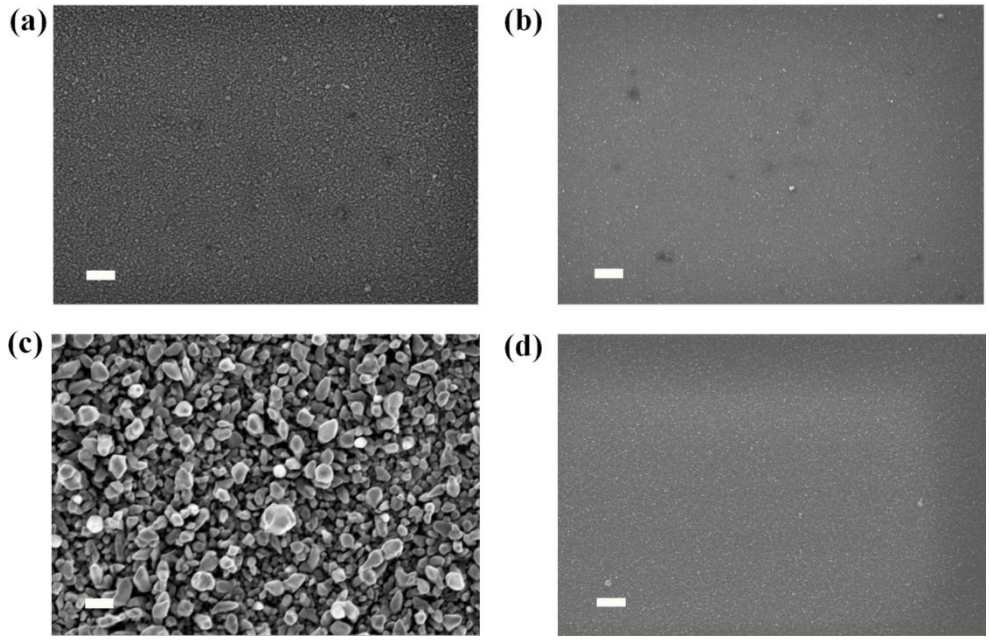

Fig. 3-6 FESEM images after various metal electrodeposition on n^+-Si/SiO_2. (a) FESEM image of electrodeposited Pt on n^+-Si/SiO_2-NH_2-AuNP. Scale bar, 200 nm. Pt was deposited at -1.7 V (vs. Ag/AgCl) for 30 min on n^+-Si/SiO_2-NH_2-AuNP in 1 mM H_2PtCl_6 and 0.1 M K_2SO_4 at pH 3.4 (b) FESEM image of electrodeposited Cu on n^+-Si/SiO_2-NH_2-AuNP. Cu deposits were prepared at -1.3 V for 30 min in the solution of 1 mM $CuSO_4$ in 0.1 M potassium phosphate at pH 3 on the n^+-Si/SiO_2-NH_2-AuNP. (c) FESEM image of electrodeposited Au on n^+-Si/SiO_2-NH_2-AuNP. Au deposits were prepared at -1.5 V for 30 min in the solution of 1 mM $KAuCl_4$ in 0.1 M potassium phosphate at pH 3 on the n^+-Si/SiO_2-NH_2-AuNP. (d) FESEM image of electrodeposited Ni on n^+-Si/SiO_2-NH_2-AuNP. Ni deposits were prepared at -1.5 V for 30 min in the solution of 1 mM $NiSO_4$ in pH 3.8 aqueous boric acid on the n^+-Si/SiO_2-NH_2-AuNP. Scale bar 200 nm.

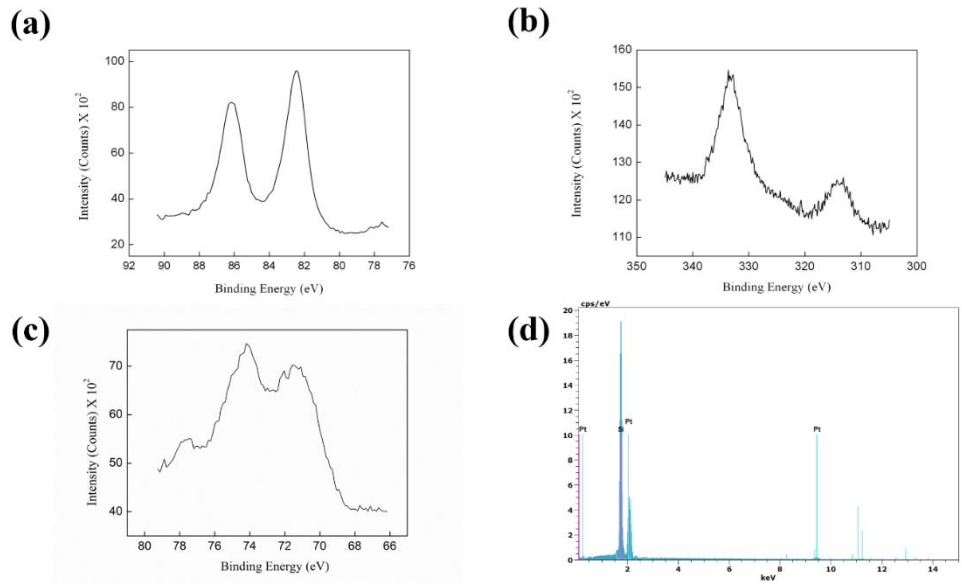

Fig. 3-7 Characterization of Pt electrodeposited on n^+-Si/SiO_2-NH_2-AuNP. (a) Au 4f core level XPS spectrum (Au 4f peak: 84.000, 87.679, 85.231 eV) (b) Pt 4d core level XPS spectrum (Pt 4d peak: 315.392, 332.259 eV) (c) Pt 4f core level XPS spectrum (Pt 4f peak: 75.740, 72.736 eV) of Au-Pt NPs on the n^+-Si/SiO_2 (d) EDS spectrum.

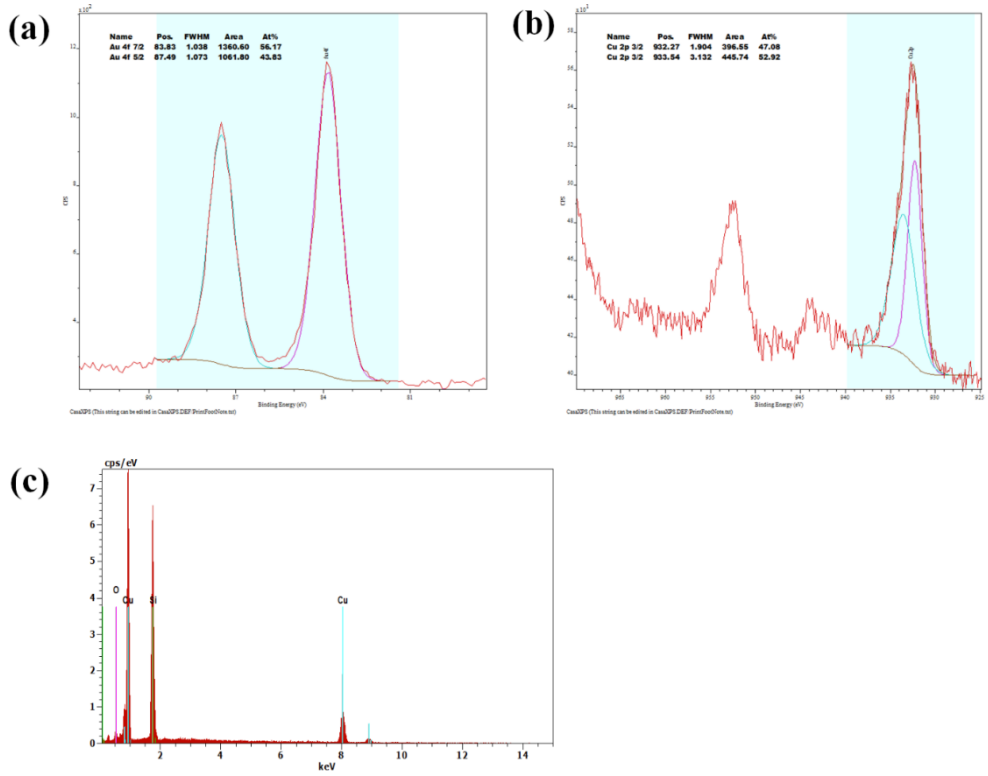

Fig. 3-8 Characterization of electro-deposited Cu on n^+-Si/SiO_2-NH_2-AuNP. (a) Au 4f core level XPS spectrum (Au 4f peak: 83.83, 87.49 eV) (b) Cu 2p core level XPS spectrum (Cu 2p peak: 932.27, 933.54 eV) (c) EDS spectrum.

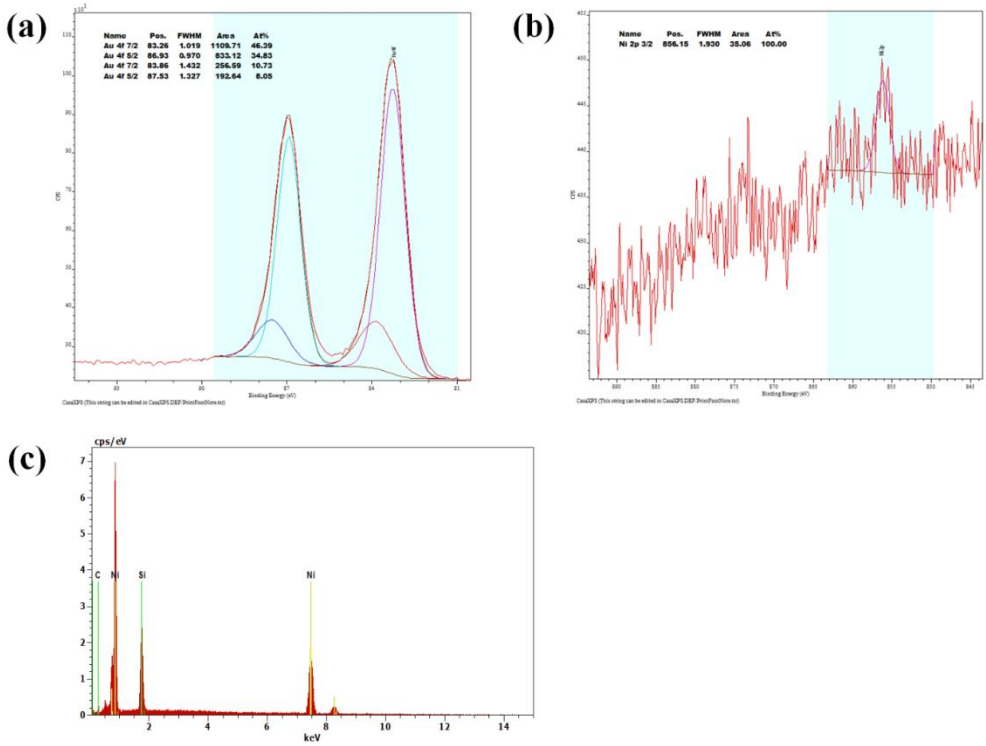

Fig. 3-9 Characterization of electrodeposited Ni on n^+-Si/SiO_2-NH_2-AuNP. (a) Au 4f core level XPS spectrum (Au 4f peak: 83.26, 86.93, 83.86, 87.53 eV) (b) Ni 2p core level XPS spectrum (Ni 2p peak: 856.15 eV) (c) EDS spectrum.

3.3.2 Investigation on the role of the modified surface of n^+-Si/SiO_2 feasible to one step electrodeposition

To investigate the working principle of this Au NPs effect, electrochemical impedance spectroscopy and linear sweep voltammetry for n^+-Si/SiO_2-NH_2 and n^+-Si/SiO_2-NH_2-AuNP were performed as shown in Fig. 3-10. Both analyses show that Au NPs on n^+-Si/SiO_2-NH_2 significantly facilitate electron transfer. Especially, the current density of the electrode with AuNP is considerably increased compared to without AuNP as shown in the $i-V$ curve (Fig. 3-10b). However, the onset potentials for the electrodeposition of Pd seem invariant near at −0.5 V (vs. Ag/AgCl). This result implies two features. First, the electrodeposition mechanism of Pd is identical irrespective of the presence of AuNP. Second, the electrical leakage current or tunneling does not occur along with the physical defects such as crevice or pinhole regardless of the existence of AuNP on the surface. In addition, the measured onset potential of Pd electrodeposition on n^+-Si (+0.4 V vs. Ag/AgCl) was extremely more positive than both n^+-Si/SiO_2-NH_2 and n^+-Si/SiO_2-NH_2-AuNP. Note that the n^+-Si electrode is considered as a conductive Si electrode with native oxides that are formed on the surface as insulating patches. To compare on the conducting electrode, the onset potential on Au wafer measured to be +0.6 V (vs. Ag/AgCl) which was even more positive.

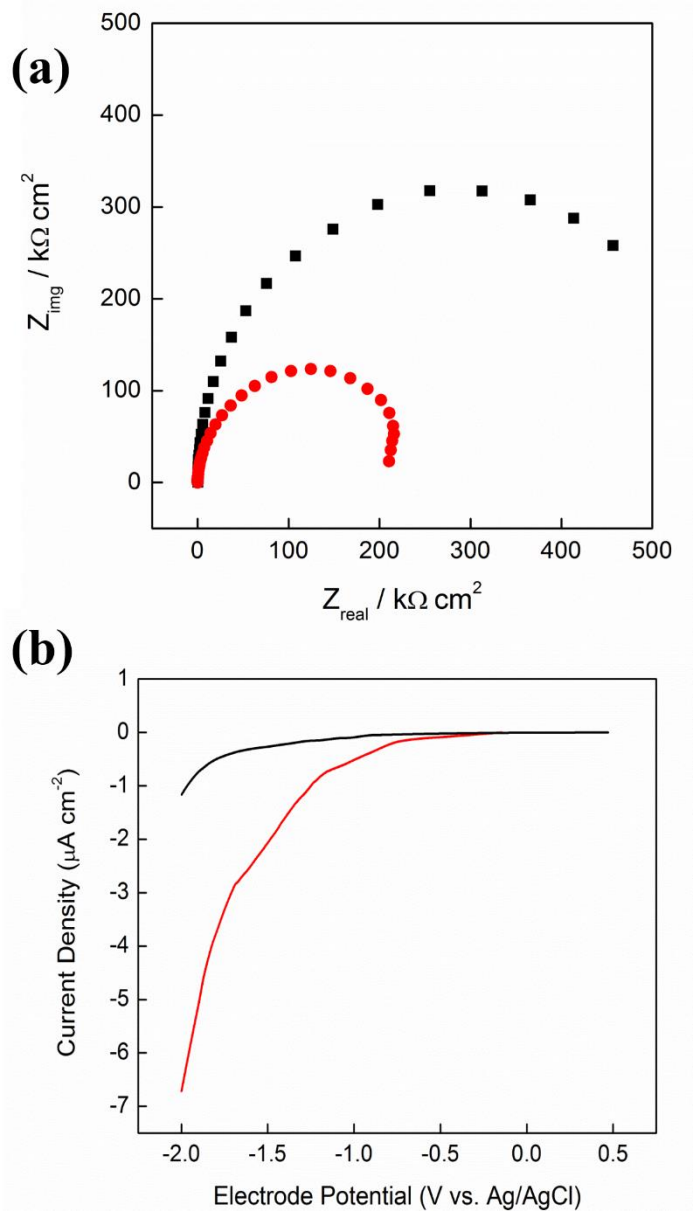

Fig. 3-10 Electrochemical behavior comparison at n^+-Si/SiO_2-NH_2 and n^+-Si/SiO_2-NH_2-AuNP. (a) Nyquist plots by impedance spectroscopy at -1.2 V (vs. Ag/AgCl) on n^+-Si/SiO_2-NH_2 (black squares) and n^+-Si/SiO_2-NH_2-AuNP (red circles) in 0.1 M potassium phosphate buffer at pH 3. (b) The *i*-*V* curves obtained from N_2-purged solution of 0.5 mM $PdCl_2$ and 0.1 M potassium phosphate (pH 3) with scan rate of 10 mV/s.

By functionalization of Au NPs on n^+−Si/SiO_2−NH_2, both the larger amount of metal electrodeposition and the greater charge passed during electroplating was achieved (Table 3−1). In short, the faradaic efficiency dramatically enhanced the pre−existence of Au NPs. The observed phenomenon can be explained by improved adhesion (or, alloying). Au NPs may anchor and even form alloys with electrochemically reduced metals acting as a seed for nucleation and to grow in large size due to the lattice mismatch of only 4% [17]. In respect to electron transfer, Au NPs cannot promote electron tunneling across the SiO_2 layer as discussed earlier [18]. However, both Au NPs and deposited metal can serve as hydrogen atom stabilizers [19], which incorporate hydrogen atoms and beneficially utilize them for a faradaic reaction. As a result, Au NPs improves the electrodeposited amount of Pd in a thin film of Pd−Au alloy on thermal SiO_2 as shown in Fig. 3−5. The detailed characterization is described in Fig. 3−11.

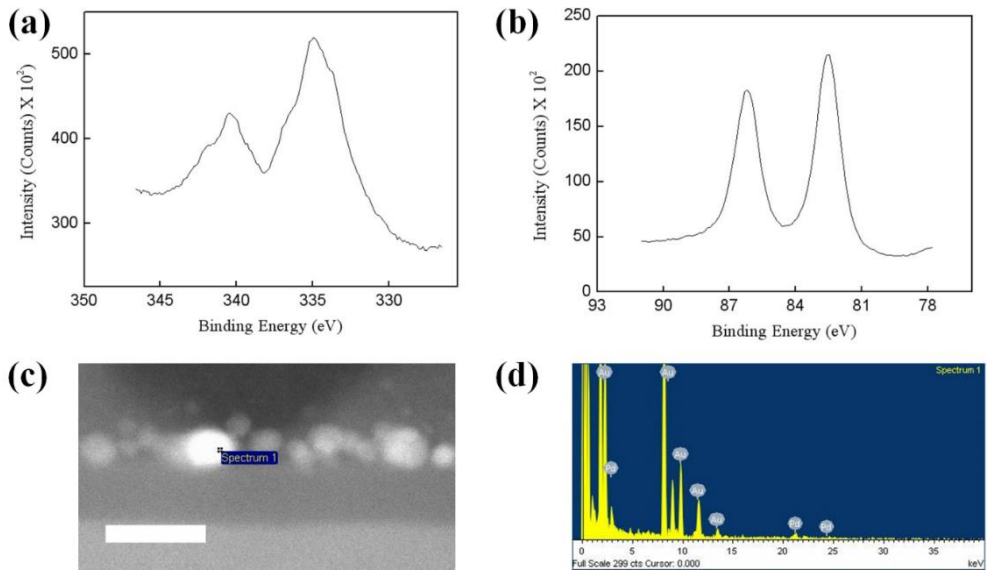

Fig. 3-11 Characterization of electrodeposited Pd on n^+-Si/SiO_2-NH_2-AuNP. (a) Pd 3d core level XPS spectrum (Pd 3d peak: 335.891, 341.966, 337.473 eV) (b) Au 4f core level XPS spectrum (Au 4f peak: 84.000, 87.685, 85.621 eV) (c) HAADF-STEM image. Scale bar 10 nm. (d) EDS spectrum at the point of "spectrum 1" in c.

3.3.3 The application as hydrogen gas sensor of a thin metal film deposited on n^+-Si/SiO_2

The method to electrodeposit metals on SiO_2 insulating layer in a single step can be applied to build resistance-based hydrogen (H_2) gas sensor [19,20] composed of a thin film of Pd NPs. Its performance of sensitive response to H_2/N_2 gas mixture is organized in Fig. 3-12. As shown in Fig. 3-12a, resistance which corresponds to the signal increases upon H_2 exposure [21,22] and it is recovered in nitrogen (N_2) gas. This kind of response and recovery are within a few minutes when tested in a tube furnace with 1000 sccm of total gas flow rate at an applied bias of as low as 2 mV. In addition, the responses were sensitive to the H_2 gas partial pressure as shown in Fig. 3-12c and Fig. 3-13. Note that the operation at 2 mV bias shows better sensitivity than higher applied bias which the reason why the sensitivity is inversely proportional to applied bias is still unclear. In addition, the detection limit was measured to be as low as 100 ppm of H_2 as shown in Figure 3-12b. Moreover, the electroplated thin metal film of Pd NPs is expected to preserve its intrinsic properties upon volume expansion of Pd to Pd:H. The demonstrated H_2 sensor based on a thin film of Pd NPs on n^+-Si/SiO_2-NH_2-AuNP demands low power consumption and less fabrication costs due to simple and reproducible method compared to previously known processes, i.e. transfer of nanostructured Pd to dielectric substrate [22-24], photoresist etching to leave Pd on substrate [24-26], co-

evaporation to deposit Pd and SiO_2 on n-GaN layer [27], etc.

Furthermore, the proposed H_2 gas sensor exhibits performance comparable to the reported high-performance H_2 gas sensors [26]. The detailed comparison to other literature is organized in Table 3-2 [23,25-26,28-29]. As discussed for the example of H_2 gas sensor, the direct electroplating method via hydrogen atom mediated electrochemistry on SiO_2 possesses great potential in a wide range of manufacturing due to its simple and cost-effectiveness.

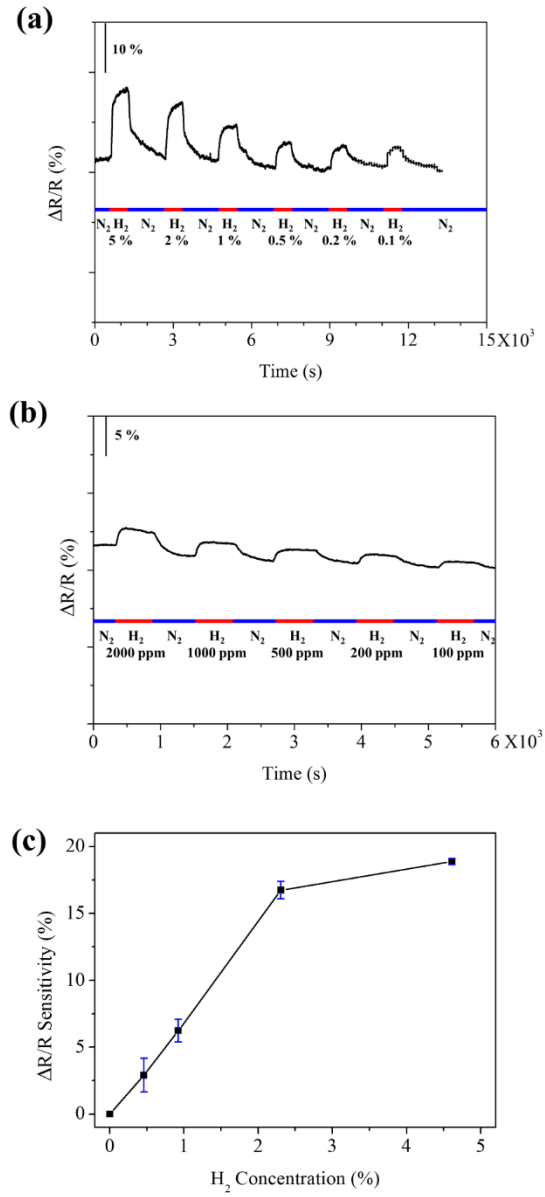

Fig. 3-12 Performance of the resistance-based H_2 gas sensor prepared via direct electrodeposition of Pd thin metal film on n^+-Si/SiO_2-NH_2-AuNP. The real-time resistance responses to various H_2 gas partial pressure which the flow was programmed for 1000 sccm gas flow at room temperature in the range of (a) 0.1 – 5% with 2 mV bias and (b) 100 – 2000 ppm with 10 mV bias. (c) Plot of sensitivity response as a function of H_2 partial pressure with 2 mV bias.

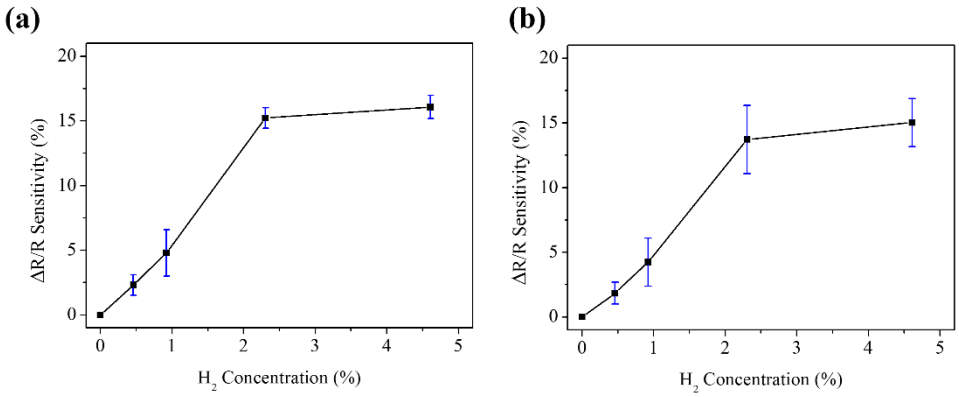

Fig. 3-13 Performance of the hydrogen gas sensor of electrodeposited thin film of Pd NPs on n^+-Si/SiO_2-NH_2-AuNP. Plots of sensitivity as a function of H_2 partial pressure with (a) 5 mV and (b) 10 mV applied bias.

Sensing constituent [a]	Dimensions	Temp (K)	τ_{resp}/τ_{rec} 0.1% H_2 [b]	τ_{resp}/τ_{rec} 4% H_2 [c]	Detection Limit	Ref
Pd thin film	d = 30 – 40 nm t = 100 nm	rt	272s/547s	185s/844s	100 ppm	This work
Pd mesowire array	d = 30 – 40 nm	rt	nr	0.07s/0.07s	1%	[23]
Pd film nanogap	t = 100 nm	rt	nr	10s/200s	0.5%	[28]
Pd nanowire	25 (h) × 130 (w) nm	rt	400s/1000s	100s/200s	100 ppm	[25, 29]
Pd@Pt nanowire	40 (h) × 100 (w) nm	294	450s/480s	80s/380s	500 ppm	[26]

[a] Abbreviations: rt = room temperature, d = diameter, t = thickness, (h) × (w) are the lateral dimensions of a nanowire with a rectangular cross-section, nr = not reported.

[b] $R_{initial}$ to 0.90R_{max} response time.

[c] R_{max} to 0.10R_{max} recovery time.

Table 3-2 Performance comparison for resistance-based hydrogen gas sensors.

3.4 Conclusion

The direct electroplating of thin metal films on thermal SiO_2 was investigated. The surface modification of SiO_2 changed the efficiency of electrodeposition. Especially for the case of n^+-Si/SiO_2-NH_2-AuNP, a uniform and thick films can be directly electroplated on the insulating layer. In addition, electrochemically reduced Pd, Pt, Cu, and Ni strongly adhere to the surface which Au NPs pre-exist on it, thus both the amount of electrodeposition and faradaic efficiency are extremely enhanced. It is suggested that the pre-anchoring of 3-5 nm Au NPs showed a superior effect in both the facilitation of electron transfer and adhesion. These results indicate that the scope of substrates for direct electrodeposition could expand to the non-conducting surface with the help of hydrogen atom mediated electrochemistry. Finally, the hydrogen gas sensor was prepared by a novel method of a thin film of Pd NPs electrodeposited on n^+-Si/SiO_2. Its performance was superior in both response and recovery time in 0.1% H_2 with 100 ppm detection limit compared to the previous reports. Importantly, the feasibility to control the film thickness implies the possibility of directly electrodeposit hundred-nanometer-thick 2-dimensional inorganic nanosheets [30] on insulator substrates.

3.5 References

[1] R. Waser, M. Aono, *Nat. Mater.*, 2007, *6*, 833.

[2] M. M.Lee, J. Teuscher, T. Miyasaka, T. N. Murakami, H. J. Snaith, *Science*, 2012, *338*, 643.

[3] K. A. Willets R. R. Van Duyne, *Annu. Rev. Phys. Chem.*, 2007, *58*, 267.

[4] G. A. Ten Eyck, J. J. Senkevich, F. Tang, D. Liu, S. Pimanpang, T. Karaback, G. C. Wang, T. M. Lu, C. Jezewski, W. A. Lanford, *Chem. Vapor. Depos.*, 2005, *11*, 60.

[5] G. M. Veith, A. R. Lupini, S. Rashkeev, S. J. Pennycook, D. R. Mullins, V. Schwartz, C. A. Bridges, N. J. Dudney, *J. Catal.*, 2009, *262*, 92.

[6] T. Osaka, N. Takano, T. Kurokawa, T. Kaneko, K. Ueno, *J. Electrochem. Soc.*, 2002, *149*, C573.

[7] E. Glickman, N. Inberg, Y. Fishelson, Y. Shaham-Diampnd, *Micro. Microelectron. Eng.*, 2007, *84*, 2466.

[8] C. H. Ting, M. Paunovic, *J. Electrochem. Soc.*, 1989, *136*, 456.

[9] R. K. Joshi, M. Yoshimura, C. -C. Chiu, F. -K. Tung, K. Ueda, K. Tanaka, *J. Phys. Chem. C*, 2008, *112*, 1857.

[10] Y. Zhang, Y. Yang, P. Xiao, X. Zhang, L. Lu, L. Li, *Mater. Lett.*, 2009, *63*, 2429.

[11] B. K. Kim, D. Seo, J. Y. Lee, H. Song, *J. Electrochem. Commun.*, 2010, *12*, 1442.

[12] J. Hu, W. Li, J. Chen, X. Zhang, X. Zhao, *Surf. Coat. Tech.*, 2008, *202*, 2922.

[13] C. M. Chang, M. T. Hsieh, W. C. Kang, T. J. Whang, *J. Electrochem. Soc.*, 2014, *161*, D552.

[14] N. Tian, Z. -Y. Zhou, N. -F. Yu, L. -Y. Wang, S. -G. Sun, *J. Am. Chem. Soc.*, 2010, 132, 7580.

[15] J. -Y. Lee, J. G. Lee, S. -H. Lee, M. Seo, L. Piao, J. H. Bae, S. Y. Lim, Y. J. Park, T. D. Chung, *Nat. Commun.*, 2013, *4*, 2766.

[16] J. A. Howarter, J. P. Youngblood, *Langmuir*, 2006, *22*, 11142.

[17] Mingshu Chen, Dheeraj Kumar, Cheol-Woo Yi, D. Wayne Goodman, *Science*, 2005, *310*, 291.

[18] J. B. Shen, L. M. H. Lai, P. K. Eggers, M. N. Paddon-Row, J. J. Gooding, *Langmuir*, 2009, *25*, 11121.

[19] D. A. Panayotov, J. T. Yates, *J. Phys. Chem. C*, 2007, *111*, 2959.

[20] J. Lee, W. Shim, E. Lee, J. S. Noh, W. Lee, *Angew. Chem. Int. Ed.*, 2011, *123*, 5413.

[21] R. K. Joshi, S. Krishnan, M. Yoshimura, A. Kumar, *Nanoscale Res. Lett.*, 2009, *4*, 1191.

[22] J. Hong, S. Lee, J. Seo, S. Pyo, J. Kim, T. Lee, *ACS Appl. Mater. Interfaces*, 2015, *7*, 3554.

[23] F. Favier, C. Walter, M. P. Zach, T. Benter, R. M. Penner, *Science*, 2001, *293*, 2227.

[24] J. Lee, W. Shim, J. S. Noh, W. Lee, *ChemPhysChem*, 2012, *13*, 1395.

[25] F. Yang, S. C. Kung, M. Cheng, J. C. Hemminger, R. M. Penner, *ACS Nano*, 2010, *4*, 5233.

[26] X. W. Li, Y. Liu, J. C. Hemminger, R. M.; Penner, *ACS Nano*, 2015, *9*, 3215.

[27] S. W. Tan, J. H. Tsai, S. W. Lai, C. Lo, W. S. Lour, *Int. J. Hydrogen Energ.*, 2011, *36*, 15446.

[28] T. Kiefer, L. G. Villanueva, F. Fargier, F. Favier, J. Brugger, *Nanotechnology*, 2010, *21*, 505501.

[29] F. Yang, D. K. Taggart, R. M. Penner, *Nano Lett.*, 2009, *9*, 2177.

[30] M. Osada, T. Sasaki, *Adv. Mater.*, 2012, *24*, 210.

4. Summary and Perspectives

This dissertation presents a study of the demonstration of the electrochemical reaction on the dielectric electrode. As mentioned in Chapter 1, electrochemistry on the insulator is counterintuitive although it may provide new insights on scientific findings and pioneering applications in many fields. Among the reports on faradaic reaction on insulators, the electrochemistry in electrolyte–oxide–semiconductor (EOS) system is worth to be noted that highly n–doped Si/thermal SiO_2 (n^+–Si/SiO_2) was brought into the solution as the electrode. it was reported that hydrogen atoms can be produced at n^+–Si/SiO_2. They are proposed to be responsible for faradaic current in voltammetry acting as “chemical electrode”, described such system as hydrogen atom mediated electrochemistry. The researches for the research on what kind of chemistry is possible on insulators and what kind of application is possible, however, was overlooked. Especially, there must be an empty space of chemistry brought into hydrogen atom from this system. Seek for the possible chemistry and application is the main work described in this dissertation.

200 nm thick defective n^+–Si/SiO_2 was fabricated and investigated the cathodic electroorganic reaction of the organic reactants as described in Chapter 2. It gives low faradaic current upon negative bias with no current upon positive bias in both acidic aqueous solution

and acidic organic media irrespective of the presence of redox couple. The electrolysis of organic reactants was found to yield either *reduced* or *oxidized* products upon *cathodic* bias. Especially, anthracene and its derivatives are confirmed to be electrochemically *oxidized* as a consequence of *cathodic* electroorganic reaction on defective n^+−Si/SiO_2. Especially, ANTH and its derivatives are electrochemically oxidized as a consequence of cathodic electroorganic reaction. It also showed a correlation between the consumed amount and acidity. Based on the analysis of the electrode itself and products of electrolysis, we propose that the observed phenomenon involves electrochemically generated species, probably hydrogen atom produced by proton reduction in the SiO_2 film. As described in Chapter 1, hydrogen atom possesses diverse reactivity towards reactants which correlates to the observation. Various sets of experiments using TEMPO, water, $H_2{}^{18}O$, and so on provided evidence that support the proposed reaction mechanism.

The direct electrodeposition of metal thin films on thermal SiO_2 was investigated and its application as a hydrogen gas sensor was demonstrated in Chapter 3. Experimental results revealed that uniform and thick films can be directly electroplated on n^+−Si/SiO_2−NH_2−AuNP despite the presence of an insulating layer, SiO_2. Electrochemically reduced Pd, Pt, Cu, Ni, or Au firmly adhere to the oxide surface via pre−anchored Au NPs so that not only the amount of metal electrodeposited but also faradaic efficiency remarkably

increase. These results indicate that substrates for direct electrodeposition are not limited to the conducting materials, but can include a non-conducting surface. Finally, H_2 gas sensor was demonstrated by a thin metal film of Pd electrodeposited on n^+-Si/SiO_2. Its performance was superior in both response and recovery time with a low detection limit.

In line with the aforementioned researches, further studies are required in the following areas: the direct characterization of hydrogen atom produced in this system, seeking for more evidence on the electrical conduction mechanism, seeking for more evidence to support the cathodic electroorganic reaction mechanism, expansion of the kinds of organic reactants and types of organic reaction, expansion to the gas-phase reaction related to energy solving issues, etc. Although many evidences of hydrogen atom is provided, there has been no direct observation. It is challenging, but the proof of such existence is obviously novel and high impact in the science community. This is actually connected to the explanation of the electrical conduction mechanism in the EOS system. More calculation data and plausible evidence are needed to generalize the conduction mechanism. The reaction mechanism of cathodic electroorganic reaction provides intuitive ideas of organic electrochemistry, but the mechanism is still not fully explained. Providing the results to fill the empty space will make such suggestion more firm. Thinking on the basis of such mechanism, more

kinds of organic reactants may be possible and need to seek for them. Consequently, more types of reactions can be found. For example, the enantioselective reaction is thought to be possible in such system. By feasible surface modification of the SiO_2, chiral information can be provided to the reaction mixture, where chiral selectivity can arise. Or, the electroorganic reaction can be brought into surface reaction by appropriate surface modification of SiO_2. Finally, the electrolyte–oxide–semiconductor was demonstrated but a demonstration of the gas phase was not done. Probably with the aid of a thin layer of acid hydration on oxides such as thin electrolyte layer or hydrogels, it is worth to check if gas molecules can undergo chemical conversion. It may be possible since this system serves as “chemical electrode”, distinct to the normal electrochemical condition.

국문초록

부도체를 이용한 전기화학은 상식적이지 않음에도 불구하고, 새로운 과학적 사실을 찾고 많은 응용 분야에서 선구적인 역할을 수행할 수 있다. 절연체에서의 패러데이 반응에 관한 보고들 중에서, 고도로 도핑된 N 형 반도체/열산화막 (n^+-Si/SiO_2) 전극을 용액에 적용하여 전해질-산화막-반도체 (EOS) 시스템에서의 전기화학을 보인 사례는 주목할 가치가 있다.

실리콘의 산화로 만들어지는 열산화막 층은 최소한의 결함으로 높은 유전체 구조를 갖기에 게이트 옥사이드로써 반도체 산업에서 일반적으로 쓰인다. EOS 시스템을 구성하기 위하여 열산화막 아래에 전도성 기판으로 고도로 도핑된 N 형 반도체가 있는 구조를 활용하면, 수소원자가 n^+-Si/SiO_2 에서 만들어질 수 있다고 보고되었다. 이를 수소 원자를 매개로 하는 전기화학이라 칭하였고, “화학 전극”으로 작용할 수 있도록 패러데이 전류에 수소원자가 기여하는 역할이 있다고 제안했다.

그러나 부도체를 이용한 전기화학은 대체로 어떤 종류의 화학반응이 가능한지 또는 어떤 종류의 응용이 가능한가에 대해 연구는 간과되었다. 특히, 이 시스템을 활용하여 수소원자를 화학 분야로 사용할 수 있다면, 연구 영역이 거의 무한할 것이다. 그래서 이 학위논문에서 다루는 주요 주제는 이것을 통해 가능한 화학 및 응용 영역을 살펴보는 것이다.

1 장에서는 부도체에서의 전기화학에 대한 배경지식을 제공하고, 특히 수소 원자를 매개로 한 전기화학이 제안된 n^+-Si/SiO_2 전극을 활용한 EOS 시스템에 주목한다. 또한, 부도체 전극을 활용한 전기화학과 화학분야에서의 수소 원자에 대한 전망을 살펴본다.

2 장에서는 결함이 있는 200 nm 두께의 n^+−Si/SiO_2 전극을 제작하고 유기 반응물에 대한 음극 전기유기반응을 살펴보았다. 여기서 결함이 명시하는 바는 핀홀이나 균열은 매우 적지만 불표화결합이나 공공과 같은 화학적 결함이 많음을 의미한다. 이 전극은 산성 수용액과 유기용매 모두에 대해 환원전위에서 작은 패러데이 전류가 나타나지만 산화전위에서 전류가 나타나지 않는다. 이 패러데이 전류는 양성자 농도에만 의존하고 산화환원종의 존재는 경미한 기여를 보이는 특징을 갖는다. 이것은 이전에 보고된 전기화학적 거동과 유사하다.

유기 반응물을 이 전극으로 전기분해를 해보면, 환원전위를 인가했는데도 불구하고 산화 또는 환원되는 생성물을 얻을 수 있음을 확인했다. 특히, 안트라센과 그 유도체들이 결함이 있는 n^+−Si/SiO_2 전극의 환원전위에 의해 산화되는 음극 전기유기반응이 나타났다. 이를 살펴본 결과, 수소 원자로 추정되는 전기화학적으로 생성된 화학종이 이 현상에 기여하는 것으로 추정되었다. 1 장에서 언급되었듯이, 수소 원자는 반응물에 대해 다양한 반응성을 가질 수 있어, 관찰된 현상과 관계가 있는 것 같다. 제시하는 반응 메커니즘의 근거가 될 수 있는 여러 실험 결과를 이 논문에서 제공한다.

3 장에서는 열산화막 전극에 직접적인 전기도금으로 얇은 금속 박막이 만들어짐을 보이고 이 구조가 수소 기체 센서로 응용이 가능함을 밝힌다. 산화막 표면을 아민기나 3-5 nm Au NP 로 개질하여 전기도금의 효율을 높이고 도금 가능한 금속의 종류를 효과적으로 늘릴 수 있었다.

절연층의 산화막이 있음에도 불구하고 균일하고 두꺼운 두께의 금속 박막이 전기도금에 의해 n^+−Si/SiO_2−NH_2−AuNP 에서 만들어지는 것을 확인할 수 있다. 미리 고정된 Au NP 에 의해 Pd, Pt, Cu, Ni, Au 와

같은 금속들이 산화막 표면에 견고히 붙어있을 뿐만 아니라 전기도금되는 양 및 패러데이 효율이 증가하는 것을 확인할 수 있었다. 이 결과는 직접적인 전기 도금은 도체에 국한되지 않고, 수소원자를 매개로 한 전기화학의 도움으로 부도체에서도 가능할 수 있다는 것을 보인다. 산화막에 직접 전기도금된 Pd 를 이용하여 수소 기체 센서를 제작하는 고유하고 새로운 방법을 시연했다. 그 성능은 기존 보고들과 비교했을 때 검출 한계가 100 ppm 정도로 낮고, 0.1% 수소 기체에 대하여 우수한 응답/회복 시간을 가졌다.

핵심단어: 부도체 전극, n^+−Si/SiO_2, 전해질−산화막−반도체 (EOS) 시스템, 수소 원자, 전기유기 반응, 전기도금.

학번: 2011−23227